

YUN DANIEL PARK

PH.D. DISSERTATION

CHAPTER 1 INTRODUCTION

1. Overview

1.1 Motivation

With the rapid development of the 'Information Age,' the need for reliable and inexpensive data storage mechanisms has grown. The world has witnessed an exponential growth of storage densities, especially in the magnetic recording industry where hard disk drive (HDD) capacity has recently grown at 60 % a year (see Fig.1.1) [Kry96, Bru96]. The current technology HDD has a capacity density around 600-700 Mbits/in², compared to 40 Mbit/in² not so long ago [Hey96]. The sharp increase in the growth can be traced to development of Anisotropic Magneto-Resistance (AMR) read-heads, whose applicability is reaching its fundamental limits. The continued growth projections are founded on a technological breakthrough in 1988 by Baibich et al who have first reported Giant Magneto-Resistance (GMR) in MBE grown Fe/Cr multilayers [Bai88]. The AMR phenomenon is characteristic of certain ferromagnetic materials. The GMR phenomenon is characteristic of layered systems of magnetic and non-magnetic materials and is also observed in granular systems.

AMR and GMR materials have been developed and proposed for various other applications. One application where magnetic systems are advantageous is random access

memories (RAM) [Dau92]. Currently, in semiconductor based integrated circuits (IC), RAM retains data by electrical charges on capacitor elements [Whi95]. Such storage is volatile since the charge must be constantly ‘refreshed.’ Magnetic systems would allow the more attractive non-volatile memory elements. Other IC applications include programmable logic devices (PLD) utilizing GMR material [Has97, She97]. Both AMR and GMR responses show states of high resistance and low resistance, i.e., a binary response, applicable to logic functions. Other applications of GMR elements either currently researched or already on the market include land mine sensors, power isolators, sensors in automotive applications such as ABS and air bag, and industrial sensor applications such as a ‘gear teeth’ sensor or object detection [Dau93, Dau96].

The above mentioned applications require patterning and processing magnetic structures ever smaller. Such reductions in dimensions promise improvements in device performance and economic feasibility. In the HDD industry, the goal of 10 Gigabits per square inch has been proposed to be reached by the year 2000. Such areal densities require feature sizes in the nanometer range [Bel98]. To obtain such reduction in dimension, researchers must incorporate available fabrication techniques (developed for semiconductor IC industry) or apply novel processes to pattern these metallic structures. Along with optimizing fabrication processes, they must understand how the reduction in dimensionality affects these structures.

1.2 Overview of Text

This dissertation will report and interpret research into magnetic systems at reduced dimensions, including novel fabrication processes applied to metallic magnetic structures and characterization methods (mainly magnetization measurements and

transport properties). Fundamentally, this research seeks to observe and isolate any new effects. Size effects will be isolated by minimizing any effects due to patterning.

Patterned structures will be compared to systems (unpatterned thin films) that have been studied in this work or elsewhere. The remainder of this Chapter will dwell on background concepts in magnetism and review of works elsewhere with similar goals. In addition, the main body of this dissertation is as follows.

In the results sections, the magnetic properties of thin films and patterned magnetic structures will be presented and discussed. Characterization will be in terms of static magnetic properties, discussed in a later section, as well as transport properties. Chapter 2 will discuss various experimental procedures for this work. These procedures can be categorized as either fabrication or characterization methods. Fabrication methods include various deposition and patterning methods. Characterization methods include physical, magnetic, and transport measurements. Chapter 3 will discuss magnetic thin film structures before patterning processes. Thin film structures include single layers of various magnetic transition metals and their alloys fabricated to study effects of elevated temperature exposure associated with various fabrication steps. GMR multilayer thin film structures will also be studied to see effects of varying spacer thicknesses to the magnetoresistance (MR).

Understanding the effect of various parameters on magnetic thin films will facilitate discussion of patterned structures to follow. Chapter 4 will discuss spin-valve magnetic structures patterned with dimensions as small as $0.5 \mu\text{m}$. Chapter 4 will report magnetization measurements using the SQUID magnetometer and transport measurements and discuss their results, highlighting geometrical effects. Chapter 5 will discuss

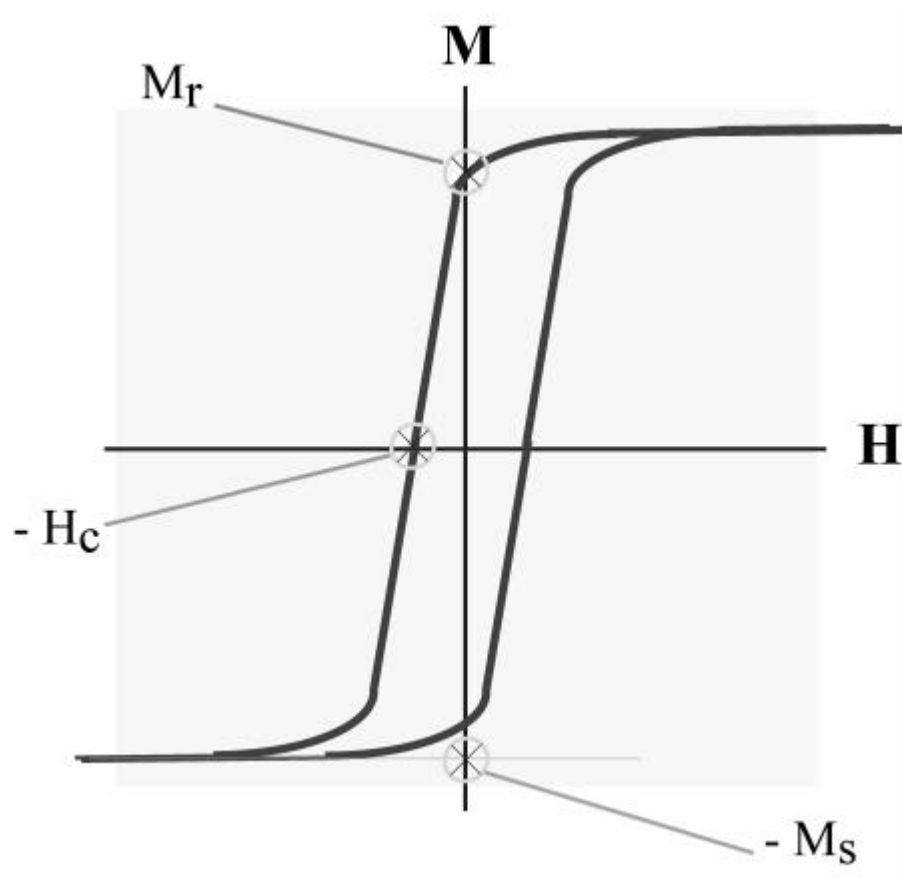


Figure 1.2 - Typical hysteresis loop (M vs. H) of a ferromagnet. Some of the pertinent characteristics are defined in the figure.

fabrication issues and results of magnetic structures with dimension in the tens of nanometers range. This Chapter will detail the electron-beam lithography techniques and their use to fabricate samples. Various techniques to fabricate nanowires will be reported and AMR properties of Ni nanowire will be detailed.

2. Background

2.1 Magnetization

The Magnetization characteristic of a material is best viewed in a plot of magnetization (\mathbf{M}) vs. applied field (\mathbf{H}). Such materials as diamagnets and paramagnets show a weak linear response (negative slope for diamagnetism) [Hum93]. For the ferromagnets, ‘hysteresis loop’ is the most evident distinction. The magnetization of a ferromagnet is dependent on its history. In this dissertation, values for remnant magnetization (M_r), saturation magnetization (M_s), and coercive field (H_C) are reported (Fig.1.2). M_r is simply the magnetization of the sample at zero applied field, and it is an important design parameter. For memory applications, one strives for high M_r . Remnant magnetization is usually reported as a ratio or a fraction of magnetization when the ferromagnet is saturated, M_s . H_C is the applied field that is required to bring the overall magnetization to be zero [Yos96]. For IC applications, one would like this value to be small so that a lower current can switch the magnetization of an element. Another magnetic response to consider is from materials that are anti-ferromagnetic, which are usually compound materials and oxides [Cu172]. These materials, with their high coercive values and exchange fields, have been used to magnetically bias the sensing magnet to certain fields and act as domain stabilizers [Par93, Tsa82].

There are many different means to measure magnetic response, either directly or indirectly. The measurement theories and techniques utilized in this work are detailed in Chapter 2.2. Magnetic response to an applied field is dependent on various parameters and phenomena. Such properties as saturation magnetization are material dependent. Other factors, even sample preparation technique, also play a role. Grain boundaries can serve as pinning sites for domain walls. Geometry of the sample affects magnetic anisotropy. Thus, magnetization measurements show response reflecting many different parameters. In this work, the roles of domains and anisotropy are more carefully considered.

2.1.1 Domain walls and motion

One of the goals of patterning ever-smaller magnetic structures is to achieve single domain elements. When an applied field aligns a magnetic element, the reverse magnetization can occur by two processes. One process is the nucleation and growth of a domain aligned with the reversed field. The other process is the rotation of magnetization to the applied field direction. For application purposes, nucleation and non-uniform motion of domain walls create noises (Barkhausen noise) which are due to discrete jumps in the magnetization [Smi88, Rus95]. Such ‘jumps’ are evident in magnetization measurements when the field is swept and are very important in transport measurements.

The formation of domain walls lowers the overall energy of the system. In a single domain magnetic element (Fig.1.3(b)), a dipolar field (whose direction is opposite to the magnetization direction) is present. As a result of the magnetic ‘poles,’ a single domain has a high value of magnetic energy, $(1/8\pi)\int \mathbf{B}^2 dV$, for single crystal sample, which is on the order of 10^6 erg/cm³. This energy density will be reduced by approximately half if the

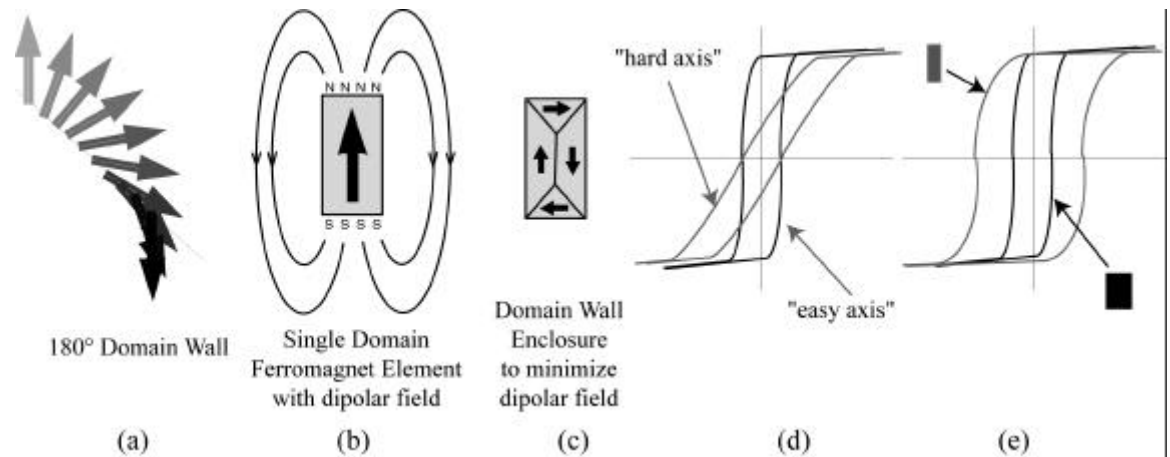


Figure 1.3 - Schematic of certain ideas in domain wall and anisotropy. (a) 180° domain wall where the direction of magnetization rotates from one domain direction to neighboring domain direction. (b) Single domain element where the dipolar fields are present. (c) Domain enclosure or circuit that minimizes the dipolar field. (d) Hysteresis loop of same structure measured in the 'easy axis' and 'hard axis.' Note that a 'hard axis' take longer to technically saturate (e) Hysteresis loops of a differing structure with differing widths. Note that the thinner material has a higher associated coercive field.

two anti-parallel magnetization domains exist. For N domain in anti-parallel arrangement, the energy will be reduced by approximately $1/N$. Dipolar field energy is zero when only domain closures are made (Fig.1.3 (c)).

Dipolar fields are the root of shape anisotropy. To lower overall energy, domains are created. At zero applied field, a domain circuit or closure is created to approach the lowest energy state. Neighboring domains of different directions share a common domain wall where the magnetization direction rotates from neighbor A to neighbor B. The way this rotation occurs determines whether the domain wall is a Néel or a Bloch type (Fig.1.3(a)) [Hub98]. Typical thicknesses of these domain walls are as small as tens of nanometers to micrometers in transitional metals and alloys [Kri63]. This twisting of the direction of magnetization raises the energy, although the overall domain closure minimizes the dipolar field energy. For element sizes approaching the thickness of domain walls, it is very energetically favorable to retain single domains since the energy cost of forming a domain wall is greater than the dipolar field energy reduction [Cul72].

2.1.2 Anisotropy

Another characteristic evident from the hysteresis loop is magnetic anisotropy (Fig.1.3(d)) [Zij82]. Anisotropy is the tendency of a ferromagnet to have a preferential direction of magnetization, i.e., an 'easy direction' or 'easy axis.' This direction can correspond to the crystalline direction or be induced by the shape of the material (i.e., a needle or wire shape prefers the magnetic axis to be along its large dimensions). An effect of crystalline anisotropy is that single crystal Fe has an easy axis along the (100) direction and a hard axis along the (111) direction. Such preferential direction of magnetization along the crystallographic axes is the magneto-crystalline anisotropy.

Most of the work in this study with anisotropy deals with that resulting from the shape of the structure, either thin films or wire shaped structures. The magnetic films deposited in this research are poly-crystalline. Although deposition of various magnetic films onto Si <100> substrates gives a particular texture, the role of the magneto-crystalline anisotropy is weak compared to shape anisotropy for poly-crystalline samples [Don91]. For thin film geometries, an uniaxial description (Eq. 1.1) is sufficient without other terms, which are usually very small [deJ94].

$$E = - K \cos^2\theta \quad (1.1)$$

where E is the orientation dependent energy of the magnetization, θ the angle between the magnetization and the film normal, and K is the anisotropy constant which gives the magnitude or the strength of the anisotropy. The sign of K signifies the preferential direction, i.e., positive K signifies the preferred magnetization perpendicular to the layer plane. Anisotropy energy K (defined per unit volume) incorporates various sources and can be described as an effective K in terms of volume contribution (K_v) and surface (K_s) contribution as

$$K = K^{\text{eff}} = K_v + 2 K_s/t \quad (1.2)$$

where the factor of two comes from two interfaces (surfaces) and t is the thickness.

Magnetic thin films generally have the magnetization in the plane of the film.

Shape anisotropy. As mentioned earlier, shape anisotropy is the main anisotropy considered in this research. It is due to dipolar fields associated with magnetic domain or magnetostatics analogous to electrostatics where ‘North’ and ‘South’ poles are analogous to positive and negative charges. Magnetostatic energy is expressed as

$$E_d = -\mu_0/2V \int \mathbf{M} \cdot \mathbf{H}_d \, dv \quad (1.3)$$

$$\mathbf{H}_d = -N \cdot \mathbf{M} \quad (1.4)$$

where \mathbf{H}_d is the anisotropic demagnetization field and N is the shape-dependent demagnetization tensor, which is simply -1 for thin films for the direction perpendicular to the layer (zero for all other direction) [deJ94]. For the purposes of this discussion, a ‘wire’ structure is defined to be a thin film with a length much greater than its width in the plane of the film. For wire, \mathbf{H}_d can be approximated as $(t/w)\mathbf{M}_s$ where t is thickness and w is the width [Baj74]. From such an analogy and a rectangular geometry, the separation of charge would be favorable along the long axis as opposed to along the short axis of a wire. A long thin wire structure would possess higher dipolar fields, requiring greater applied fields to reverse the magnetization direction, resulting in a higher coercive field, H_C (Fig.1.3(e)). Thus, the shape of the element along with the direction of the applied field determines the effect of the anisotropy.

2.2 Magneto-Transport/Magneto-Resistance

All charged carriers are affected by magnetic fields. Applied magnetic fields have many wide ranging effects from the Hall Effect to lowering the mean free path as electrons precess along the applied field under Lorenz forces ($\mathbf{E} \times \mathbf{B}$). The resistivity dependent on the square of the magnetic field is sometimes referred to as ordinary magneto-resistance. This dissertation will generally concentrate on transport properties in ferromagnets, more specifically transition metals (Fe, Co, Ni, and their alloys). Ever since Mott [Mot64], the general assumption of transport or conduction in ferromagnets is that it is carried by two independent channels that are parallel, one for spin up or majority spin and the other for

spin down or minority spin. Generally, spin-flip scattering mechanisms do not dominate until temperatures are much higher than ferromagnetic ordering temperatures (Curie temperatures for Fe, Co, Ni are 1043, 1388, 627 K, respectively [Woh80].). Other scattering processes such as defects, impurities, surfaces, and interfaces complicate this simple view of independent and parallel channels.

Another influential scattering mechanism is scattering between s- and d- bands, which are generally attributed to conduction in the above ferromagnetic transition metals. The d-band plays a particularly important role since it is the final state of this scattering process. A schematic of the band energies is depicted in Figure 1.4. The asymmetry in population and energies explains ratios of resistivity of minority spin to majority spin as high as ten for certain alloys. How the d-band distorts in applied magnetic fields gives the subtle foundations of anisotropic magneto-resistance, AMR [McG75].

3. Anisotropic Magneto-Resistance

The term anisotropic magneto-resistance describes the fact that magneto-resistance differs depending on the geometry of the orientation of the transport current and the applied magnetic field. It results from an anisotropic scattering mechanism such as that provided by spin-orbit coupling, which is a relativistic effect [Par94]. In the case when the current is parallel to the applied field, the magneto-resistance (MR) is positive, i.e., the resistance increases as the applied field is increased. This response is also referred to as longitudinal AMR. When the current is perpendicular to the applied field, the MR is negative; i.e., the resistance decreases as the applied field is increased. Like longitudinal AMR, this geometry labels this response as transverse AMR. The value quoted for AMR

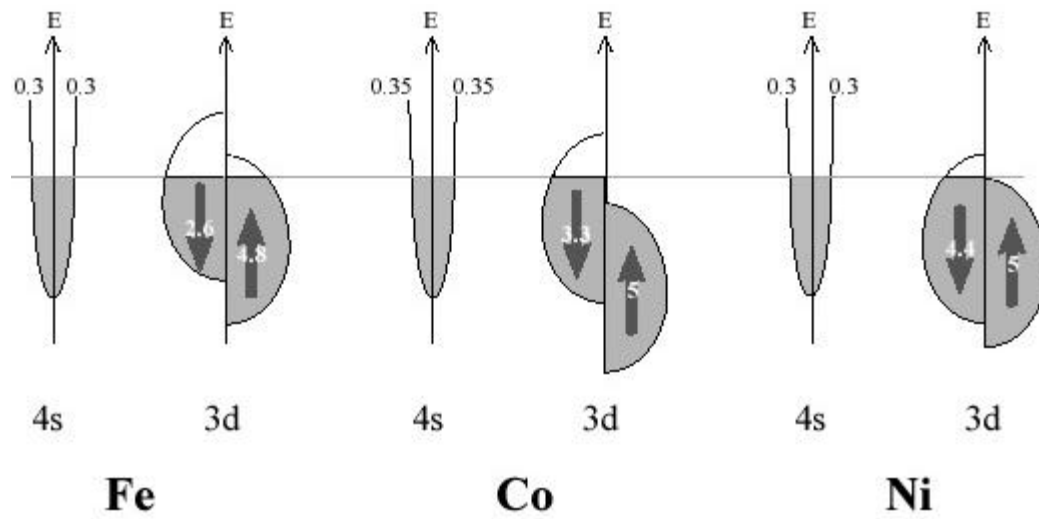


Figure 1.4 - Schematic of s- and d- bands attributed to conduction with relative population and energy respective to fermi energy [Mat91].

is the percent change of resistance from the parallel to the perpendicular case. Typical AMR values are 3-5% at room temperature [Cam82].

AMR has been successfully developed in such applications as read-head for hard disk drive applications, as mentioned earlier in this Chapter, and they have replaced inductive heads [Enz82]. Due to the relatively small but well-behaved percent change, AMR structures are limited to devices with minimum sizes of a couple of micrometers. For structures at smaller dimensions, the device resistance increases and the MR signals are no larger than background noises. To overcome these limitations, there has been considerable interest and development of Giant Magneto-Resistance (GMR), discussed below.

4. Giant Magneto-Resistance

4.1 Origins of GMR

An interesting and well-studied phenomenon in magnetic multilayers is oscillatory ferromagnetic coupling between magnetic layers separated by a non-ferromagnetic spacer layers [All98]. Such a coupling mechanism has been observed in many ferromagnetic layers and many spacer layers (which include non-ferromagnetic transition metals [Par91a] and noble metals [Ben90]). The coupling energy oscillates depending on the spacer thickness, changing from ferromagnetic coupling (magnetization is parallel) to anti-ferromagnetic coupling (magnetization is anti-parallel), between two or more ferromagnetic layers.

Such a phenomenon has been predicted in theory for metallic multilayer systems but not demonstrated until the late 1980s [Fer94]. In metallic systems, the conduction electrons are delocalized and are able to ‘carry’ magnetic exchange through non-ferromagnetic metallic spacer layers. In general terms, the conduction electrons mediate

the coupling, which is described by the RKKY (Ruderman-Kittel-Kasuya-Yosida) interaction [Rud54]. Reviews of the oscillatory coupling behavior in magnetic multilayer structures are found in the literature [Hei93, Fer95]. Studies of this phenomenon inadvertently led to the discovery of Giant Magneto-Resistance (GMR). Researchers in France conducting transport experiments on Fe/Cr anti-ferromagnetically coupled multilayers found negative magneto-resistance (i.e., resistance decreases as the applied field is increased) with the change in resistance being orders of magnitude higher than AMR [Bai88].

4.2 Theory

GMR can be explained in terms of bulk or interface scattering as the mean free paths of minority spin and majority spin carriers are altered. There are many theories proposed for GMR, both semi-classical and quantum mechanical models as examples [Cam89, Lev90]. Semi-classical models introduced parameters such as relaxation times and transmission coefficients to account for various scattering mechanisms. The Boltzmann equation is then used to describe how the perturbation of the electron distribution is affected by neighboring magnetic layers [Bar90]. A limit to the semi-classical approach occurs as the magnetic thickness approaches zero. The resistivity is given by $\rho = t/\ln(\lambda/t)$ where t is magnetic layer thickness and λ is mean free path as $t \rightarrow 0$, $\rho \rightarrow 0$. Quantum mechanical models fit the experimental data better for thin films since they predict that resistivity varies as $1/t^2$ [Fis89]. The key to successful quantum mechanical modeling is to accurately describe the spin scattering of free electrons. The

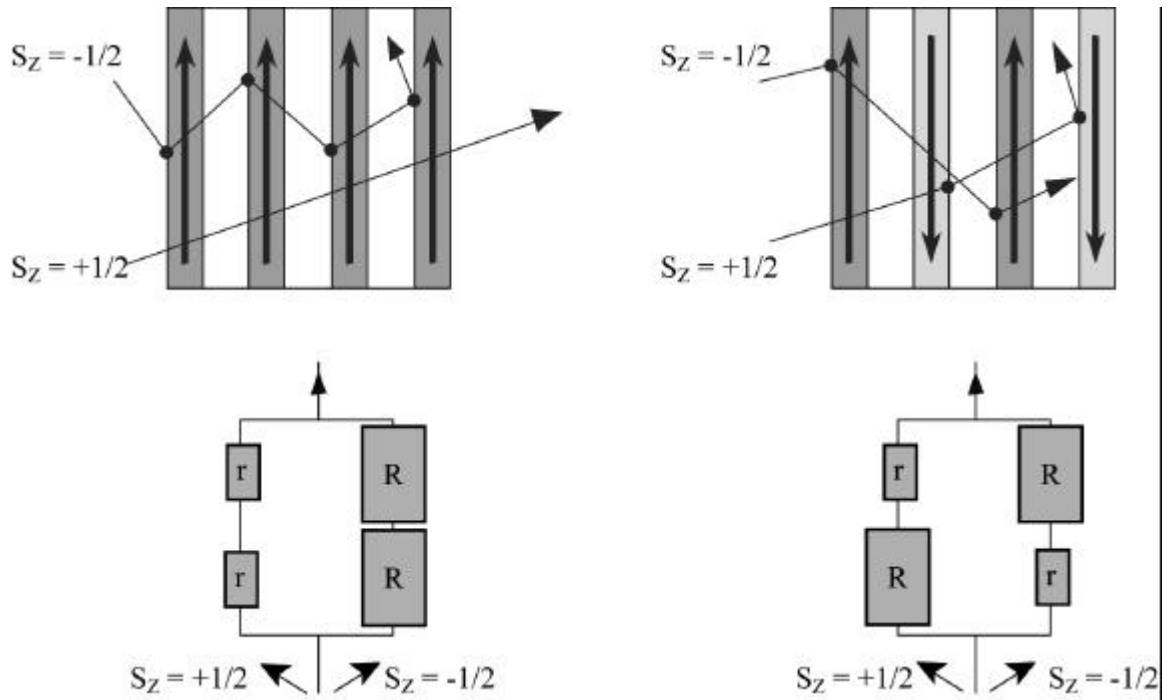


Figure 1.5 - Simple model of GMR for $MFP \gg t$, thickness of magnetic layer, in terms of a parallel resistor network. The scheme on the left represents the state of all magnetizations being parallel and resistivity as described in Eq. 1.5. The right scheme represents anti-parallel magnetization described in Eq. 1.6.

quantum mechanical model reduces to a simple model of GMR for a special case as described below [Zha92].

GMR is attributed to the scattering of conducting electrons by successive magnetic layers. Simply, consider the case where the mean free path (MFP) of the electron is much greater than the thickness of the magnetic layer ($MFP \gg t$). Also, consider that a spacer layer (noble metal or any non-ferrous metal) separates the magnetic layers and that the magnetic layers' magnetizations are either parallel to each other or anti-parallel (see Fig.1.5). If the accepted conduction is modeled by two independent channels, spin up or spin down, then cases can be imagined where one channel is less scattered or where both channels are equally scattered. The former occurs when all magnetizations are parallel, and the later when there is an anti-parallel arrangement. When all magnetizations are parallel, one carrier will provide a 'short,' again if $MFP \gg t$ is assumed. In the other case, both carriers are scattered. In terms of the illustrated parallel resistor network, the following applies:

$$\rho_F = \rho_{\uparrow} \rho_{\downarrow} / (\rho_{\uparrow} + \rho_{\downarrow}) \quad (1.5)$$

$$\rho_{AF} = (\rho_{\uparrow} + \rho_{\downarrow}) / 4 \quad (1.6)$$

$$GMR = (\rho_{AF} - \rho_F) / \rho_{AF} = (\alpha - 1 / \alpha + 1)^2 \text{ where } \alpha = \rho_{\downarrow} / \rho_{\uparrow} \quad (1.7)$$

where ρ_F and ρ_{AF} are parallel (Fig.1.5 left) and anti-parallel (Fig.1.5 right) resistivities and ρ_{\uparrow} and ρ_{\downarrow} are majority and minority spin resistivities as depicted by r and R in Figure 1.5. Equations 1.5 and 1.6 are the simple resistance of a parallel network. The ratio of the two cases gives the MR value which, using algebra, can be expressed in terms of ratio of majority and minority spin channels' resistivities. For less ideal cases, a term is needed to

describe the spin-mixing processes, which lower GMR. Achieving anti-parallel alignment of magnetization plays a large part in achieving large MR values.

Since researchers understand that anti-parallel magnetization between successive magnetic layers is important to GMR, many clever ways to achieve such an alignment have been developed. An excellent review of various GMR structures is in Dieny et al [Die94].

4.3 Geometrical Considerations

Although GMR is isotropic, there are two standard transport measurement geometries. Most common is the Current-In-Parallel (CIP) configuration where the injected current direction lies parallel to the layers. The other geometry is the Current-Perpendicular-to-Plane (CPP) configuration where the direction of current is perpendicular to the layers. In this work, CIP geometry would be considered although CPP nanostructures have been reported (see Chapter 1.5.1). In addition to the difference in geometries, there are other important differences, such as the relevant scaling parameter. In the CIP geometry, the mean free path is an important parameter while, as in the CPP geometry, the scan diffusion length is much more important (this length is usually larger than mean free path) [Fer93, Val93]. For 3-d transition metals, this length can be as much as ten times or more longer than the momentum mean free path [Joh91]. In the CPP geometry, the conducting electron traverses through many layers, and its GMR values are larger than CIP GMR values [Pra91, Lee92]. In this work, CIP geometry will be mainly considered although there have been several studies into CPP structures at nanometer dimensions by electrodeposition through nanoporous membranes [Pir94, Voe95, Dub97]. CPP structures are much more difficult to prepare and characterize since, due to the

geometry (the length is on the order of 10^3 \AA), electrical potential drop thus the resistance is very small, and the contact resistances become significant. Super-conducting contacts such as Nb to lower contact resistances have been used and limit characterizations to cryogenic temperatures [Cab98].

4.4 Thin Film Structures Displaying GMR

4.4.1 Multilayers

As previously mentioned, the first GMR structures were anti-ferromagnetically coupled multilayer structures. One of the largest GMR values is found in Co/Cu multilayer structures with spacer periodicity of about 9 \AA [Mos91]. Values of 100% are not uncommon for Co/Cu structures at the first anti-ferromagnetic maximum (first spacer thickness where the magnetic layers' magnetizations are anti-parallel). Typically, Co/Cu multilayers are hindered by rather high coercive fields [Hol96], and it is extremely difficult to control such tight spacer tolerances in industrial productions. More specifically, Co/Cu multilayers also suffer from low sensitivities, which are defined by change in resistance over change in applied field, $\Delta MR / \Delta H$. For example, the Co/Cu multilayer at its second anti-ferromagnetic coupling in this research displayed approximately 25% MR over 500 Oe while $\text{Ni}_{0.8}\text{Fe}_{0.2}$ (Permalloy)/ Cu/Co spin-valves (discussed later) showed sensitivity of 1% MR over 1 Oe.

Dipolar coupling has also been studied in Permalloy/Ag annealed or patterned multilayers [Hy193]. In these samples, annealing causes Ag to diffuse into grain boundaries of $\text{Ni}_{0.8}\text{Fe}_{0.2}$ layers, which magnetically align as anti-parallel to reduce dipolar interactions. Such multilayers show low coercive fields and it remains unclear whether such systems can be developed for applications, although they show low coercivity and

high sensitivity. Both of these systems will be studied and reported in this dissertation (Chapter 4).

4.4.2 Spin-valve

Spin-valve generally describes a tri-layer arrangement where the spacer layer is between ferromagnetic layers [Die91a]. An author of the term cites three reasons for distinguishing it from GMR multilayer: 1) amplitude of the effect is smaller than 1% in many multilayers; 2) there are sometimes other contributions to the observed giant MR; 3) the term ‘magnetic valve’ has been introduced earlier for tunneling devices utilizing two ferromagnetic layers between a thin insulator. Unlike the above described magnetic multilayers that achieve anti-parallel state by coupling through the spacer layer, these structures achieve an anti-parallel arrangement by different coercivities for the magnetic layers: one layer can be termed the ‘hard’ layer and the other the ‘soft’ layer. The anti-parallel state occurs when the magnetic layers, which have weak or no coupling, change the direction of magnetization at different applied fields. At some field between the coercive fields of the ‘soft’ and ‘hard’ layers, magnetization of the ‘soft’ and ‘hard’ layers would be expected to be anti-parallel.

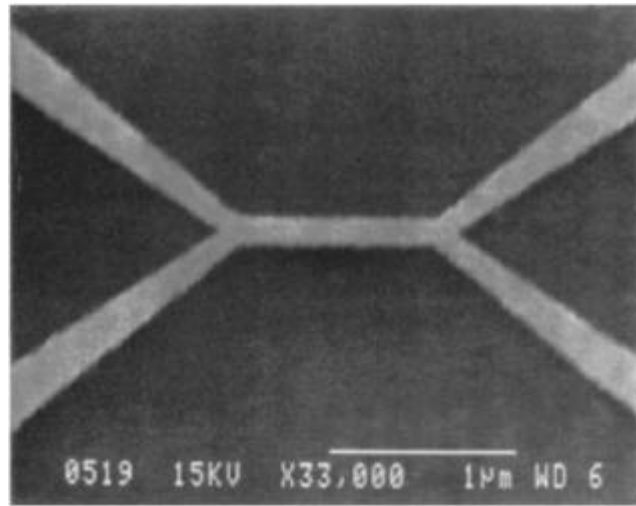
There are many methods to achieve this distinction between the layers. For example, the hard magnetic layer can be achieved by exchange coupling to an anti-ferromagnet, such as FeMn, to form exchange bias sandwich structures [Die91b, Rij97]. Another method is to use differing thicknesses of the magnetic layers, since then one layer would have higher coercivity than the other [Eve98]. Such structures are sometimes referred to as a pseudo spin-valve. Using different magnetic layers such as Permalloy (low coercivity) and Co (higher coercivity) would constitute a spin-valve structure [Shi90]. In

general, spin-valve-like structures have much lower MR values than multilayer structures, ranging on the order of tenth of a percent, but they possess low coercivities and high sensitivities due to incorporation of soft magnetic layers such as Permalloy and Super-Permalloy. Like the multilayer GMR structures, various spin-valves will be studied and reported in Chapter 4.

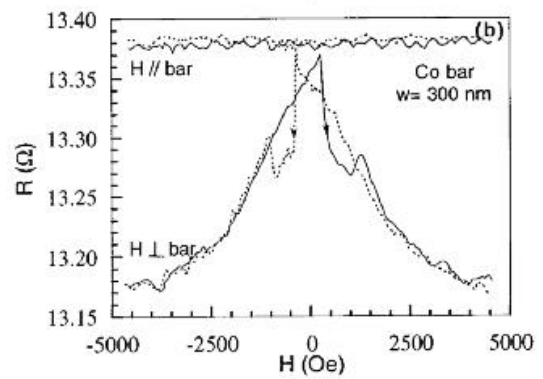
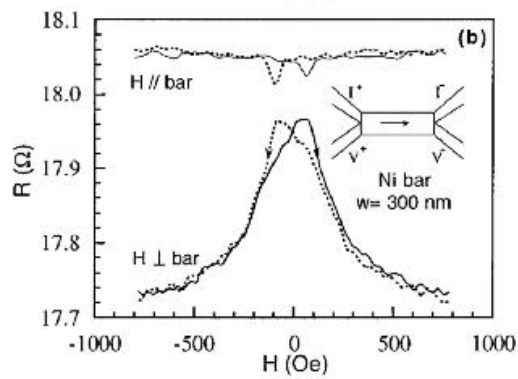
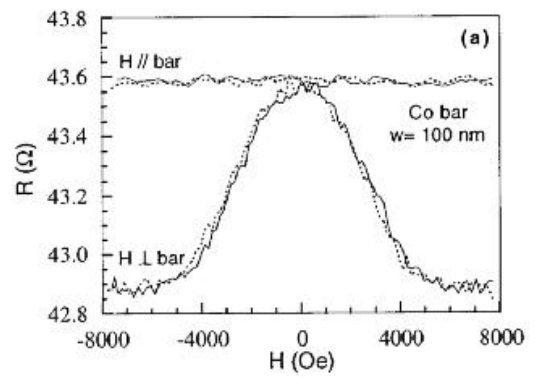
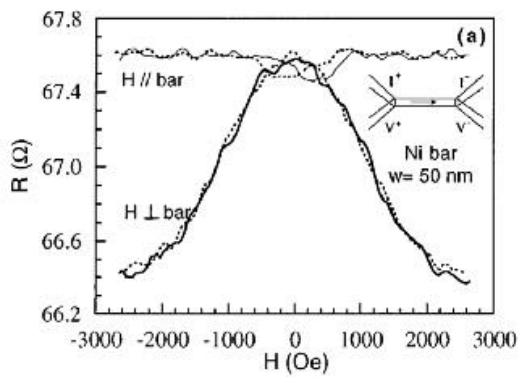
5. Literature Review of Patterned Magnetic Structures

5.1 Co, Fe, Ni, and $\text{Ni}_{0.8}\text{Fe}_{0.2}$ Wires of Small Widths

Hong et al reported transport measurements on Ni wires of approximately 200 Å thick and 200-800 Å wide [Hon95a]. The samples were prepared by evaporation deposition onto an insulating substrate (of glass) with step features. After deposition, the samples were ion milled at an angle where the step shadowed a portion of the film to result in a wire structure. They deduced from transport measurements such properties as domain wall formation and movement. They observed the shape of the longitudinal magneto-resistance (AMR where current is parallel to applied field) and noted that domain wall formation (at such small dimensions) occurs and is present by hysteresis arguments. They also observed sudden changes in resistance vs. swept field and attributed these to ‘escape’ of domain walls from pinning sites. They have suggested the variation in the width of the wire sample as possible pinning sites for the domain wall motion. To test their claim, they purposely fabricated a sample with rough edges to observe these pinning processes [Hon95b].



(a)



(b)

(c)

Figure 1.6 - From Jia et al, (a) SEM micrograph of Ni bar, (b) MR response of Ni bar of differing widths, (c) MR response of Co bar of differing widths [Jia97].

Jia et al fabricated Ni and Co 'bars' of 50-500 nm in width of 1 μm length by electron-beam lithography using PMMA resist spun on SiO_2 . They evaporated 35 nm of Ni and Co, followed by a lift-off in acetone [Jia97]. The patterning also incorporated current and voltage leads arranged at the ends of the bar (Fig.1.6(a)). These bars were characterized by transport measurements. They reported the longitudinal MR (current parallel to the applied field) response of Co to be flat (Fig.1.6 (c)) while Ni bars were not (Fig.1.6(b)). They attribute this difference to the fact that for Co, the bar widths are much below the domain wall size, resulting in a single domain formation. Since Co is in the single domain regime, magnetization will be either parallel or anti-parallel to all applied fields by shape anisotropy. Since magnetization is parallel to the axis, the current would be always either parallel or anti-parallel; thus, the MR response would be flat. Conversely, Ni response showed the magnetization to be non-uniform at low fields, which agrees with Hong et al [Hon95a].

They also observed a difference in transverse MR response between Co and Ni. While Co transverse response was independent of width, the Ni transverse response varied with width. This difference was attributed to the same reasoning as for the difference in longitudinal response. They have concluded the overall AMR ratio to be mostly independent of width, although they acknowledged the possibility of lowering the AMR ratio due to increase in resistivity due to electron scattering at bar edges.

Nozaki et al also looked at Co structures patterned by electron-beam lithography [Noz98]. In their processing procedure, PMMA was spun on 0.5 μm thick SiO_2 on an Si substrate. After exposure and development, they wet etched SiO_2 using buffered HF solution to obtain an undercut mask profile, which facilitates the lift-off process. They

patterned arrays of Co wires 1 μm wide and 280 μm long. The spacing between the wires was varied from 4 to 8 μm . They characterized their array structure by resonating-sample magnetometry (RSM) with a quoted sensitivity of 1×10^{-7} emu at room temperature for applied fields between ~ 5 kOe either parallel or traverse to the wire axis. They found that the magnetization values depended upon the directions, which they attributed to shape anisotropy. They calculated the uniaxial anisotropy constant assuming a domain wall width of 8.95 nm. They concluded the magnetization reversal to be by domain wall nucleation and propagation as opposed to rotation. This conclusion contradicts the claims reported above by Jia et al [Jia97].

The Cavendish Laboratory group has reported electron-beam patterned sub-micrometer wire arrays of $\text{Ni}_{0.8}\text{Fe}_{0.2}$ and Fe deposited by evaporation. The processing involved a series of wet and dry etching to transfer the pattern [She96]. They characterized these structures by both transport measurements and magnetization measurements such as magneto-optical Kerr effect (MOKE) [Ade97]. For the Permalloy arrays, they observed an increase in the coercive field vs. the linewidth (corresponding to sharp minima in longitudinal MR curves) from approximately 10 Oe at 10 μm to 400 Oe at 0.5 μm . The wire samples were 500 \AA thick, had a space to width ratio of ten, and the length was much greater than the width. They attributed the change in MR response to an inhomogeneous demagnetization field across the width of the wires resulting from spatial variation of the dipolar field due to edge charges [She94]. When the widths were decreased, a greater portion of the current was affected by the edges where demagnetization fields were large; thus, the response extends to larger applied fields.

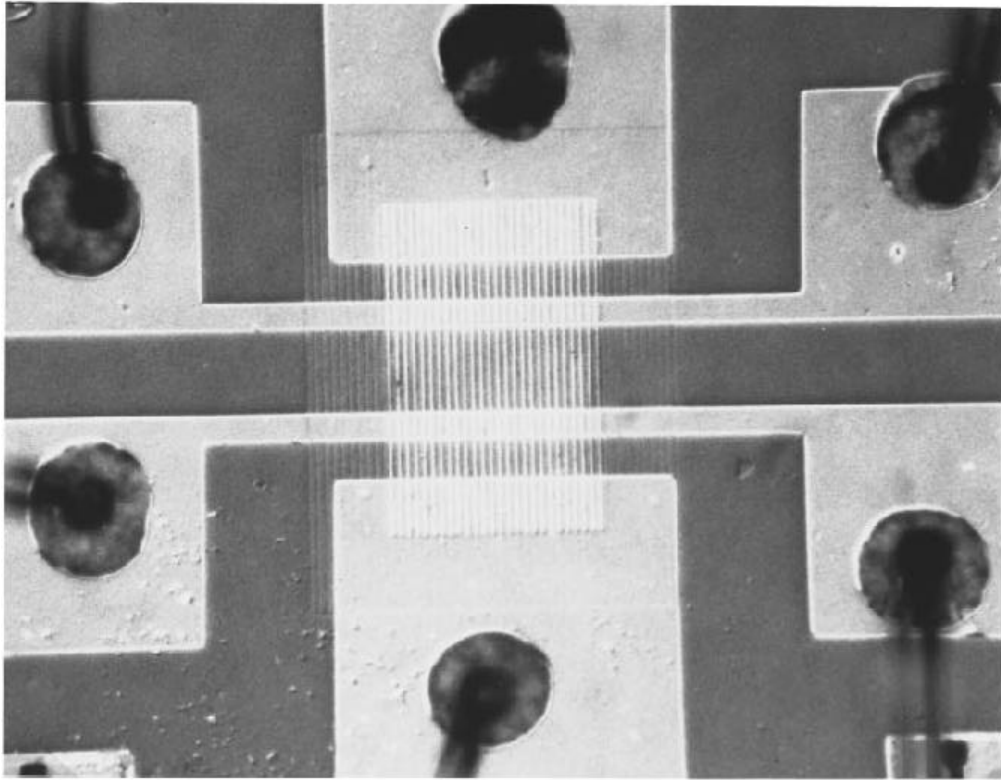


Figure 1.7 - From Adeyeye et al, an optical micrograph of the grating structure and contact geometry for transport measurements [Ade97].

MOKE measurements showed that patterning created ‘hard’ and ‘easy’ axes compared to four-fold anisotropy (no preferential direction in the plane) of unpatterned film.

Patterning of Fe arrays were complicated by the presence of uniaxial anisotropy present in single crystal Fe films in the [100] direction. By MOKE measurement, they observed this anisotropy and chose to align the wire axis at 45° , so that cubic magnetocrystalline anisotropy field, along the directions parallel and perpendicular to the wires, were equivalent. Shearwood et al also fixed the width at $0.5 \mu\text{m}$ with various space widths between wires. They found that the MOKE magnetization measurements and the MR measurements differed according to spacing widths. They attribute this to the angle of magnetization being non-uniform across the whole sample because the wires in the center array experienced different fields due to neighboring wires [She94].

Piroux et al have reported fabrication of arrays of Co, Ni, $\text{Ni}_{0.8}\text{Fe}_{0.2}$ and Fe sub-micrometer wires by electrodeposition through cylindrical pores of track-etched polymer membranes [Pir97]. In their study, the average spacing between the wires was much larger than $1 \mu\text{m}$ so that the dipolar interactions between the wires were weak. They conducted magnetization measurements with the applied field along the axis of the wires. They observed the coercive field to increase dramatically as the diameter decreased; i.e., Ni coercivity increased from approximately 200 Oe for 200 nm to 800 Oe for 50 nm. Like Jia et al, they observed a difference between Co and Ni. For Ni, the remnant ratio M_r/M_s was nearly 0.8 for all diameters, while for Co it varied from nearly 1 at 35 nm to 0.1 at 500 nm. They attributed this difference to the fact that the ‘squareness’ of the hysteresis loops (remnant ratio of one being ‘square’) for the applied field parallel to the wire axis occurred only if shape anisotropy was much greater than magneto-crystalline anisotropy.

They found by TEM that the c-axis of hcp Co (the ‘easy’ crystalline axis) was oriented perpendicular to the wire axes. For Fe, Ni, and $\text{Ni}_{0.8}\text{Fe}_{0.2}$, the shape anisotropy constant is approximately an order of magnitude higher than magneto-crystalline energy. This difference was also evident in AMR properties, where Co had the greatest longitudinal MR response while others had minimal response.

5.2 GMR Multilayer Structures of Small Widths

Kume et al utilized electron-beam lithography and lift-off to pattern arrays of wires with width and line spacing varying from 0.6 to 10.0 μm . GMR structures were deposited by ion-beam sputtering [Kum96]. Their goal was to obtain superior MR characteristics. They characterized the exchange-biased sandwich structure as $\text{Fe}_{0.5}\text{Mn}_{0.5}(70\text{\AA})/\text{Ni}_{0.8}\text{Fe}_{0.2}(34\text{\AA})/\text{Co}(6\text{\AA})/\text{Cu}(28\text{\AA})/\text{Co}(6\text{\AA})/\text{Ni}_{0.8}\text{Fe}_{0.2}(54\text{\AA})$ with magnetization and MR data while varying the angle between the wire axis and the applied field. They concluded that the strong shape anisotropy reduces the difference in coercivities of the exchange-biased layer and the free layer from the fact that the magnetization loops were rectangular. This reduction resulted in only a partial anti-parallel alignment, thus lowering the GMR value. Other GMR structures they considered were biquadratic coupled multilayers (coupling resulting in 90° alignment). For these structures, they observed an increase in MR compared to unpatterned films and higher sensitivities, where shape anisotropy improved the magnetic alignment in the multilayers.

As mentioned previously, certain nanowire structures are fabricated by electrodeposition through nano-pores of an etched membrane. This technique has been used by Beeli et al, Blondel et al, Schwarzacher et al, and Piraux et al to study GMR multilayers in the CPP geometry [Bee97, Blo94, Sch97, Pir97]. The use of nanostructures

for CPP structures is attractive, since contact and interface resistances are a large portion of the overall resistance for macroscopic structures in the CPP geometry. By inducing geometrical constraints, resistances across the layers are comparable to contact resistances.

CHAPTER 2 GENERAL EXPERIMENTAL PROCEDURE

1. Fabrication

1.1 Deposition Techniques

1.1.1 Sputter deposition

Parkin demonstrated that UHV sputtering deposition systems are capable of producing multilayer films with high GMR values [Die94]. Sputter deposition has great advantages in depositing magnetic thin films. It allows the use of alloy targets such as Permalloy and Super-Permalloy that produces films of the same stoichiometry. Sputter deposition rates are relatively high, which is an advantage in manufacturing. Most elements, alloys, and compounds may be sputter-deposited, including oxides.

Sputtering is a physical vapor deposition (PVD) technique. An atom is passed into a vapor phase by an ion. An electrical field accelerates this ion to a high enough energy so that the momentum transferred to target atoms is sufficient to eject them from the solid. After reaching low base pressures in sputter deposition system (typically $< 10^{-5}$), gas (with a pressure around few hundred millitorrs) is ionized by energetic electrons. Typically, noble gases* such as argon (Ar) are used as the gas if no chemical changes between the

* In the system used, the gas enters the chamber controlled by a mass flow controller, typically with a flow rate of 20 sccm. Pressure during sputtering is maintained by a butterfly valve, which varies the effective pumping rate of the vacuum pump (Fig.2-1).

target and the deposited film composition are desired. Once the process is started, many more gas atoms are ionized due to a cascading effect in the high electric field; i.e., one energetic electron may ionize several gas atoms from which other electrons participate – creating plasma. If the cathode is a conductor, a steady-state potential (due to a considerable difference in mobility between the ions and electrons) is created, and the potential drops across the ‘cathode dark space,’ typically 1 to 4 cm in length. In the case of an insulating target, surface charges are present that would terminate the process by creating an opposing field. An RF power supply (alternating polarity) solves this limitation. In this steady-state potential, ions are accelerated with typical energies of around 100 eV (threshold energy for Ar to yield Co atom is 25 eV) [Ohr92].

Such parameters as choice of gas, its pressure, and source power can alter the process to maximize sputter yield (number of adatoms created per ion) and deposition rate. Many of the processes involved in sputtering consume the delivered power in heating the target material, which, in turn, needs to be constantly water cooled [Wes80]. There are many more possible variations of the process described above to produce magnetic thin films. It can be as simple as using xenon as the sputtering gas or as elaborate as ion beam sputtering [Gan96, Doi93]. In this work, the magnetron-sputtering technique is utilized. This variation utilizes magnetic fields above the target to confine the plasma. This confinement results in higher concentrations of ions, which allows for deposition at higher rates and/or lower pressures (as low as 0.5 mTorr) [Ros93]. In the deposition chamber used (Fig.2.1), the target shape is round with a diameter of 2”. The sputtering gun has a magnet that creates a field, and field geometry confines the plasma in

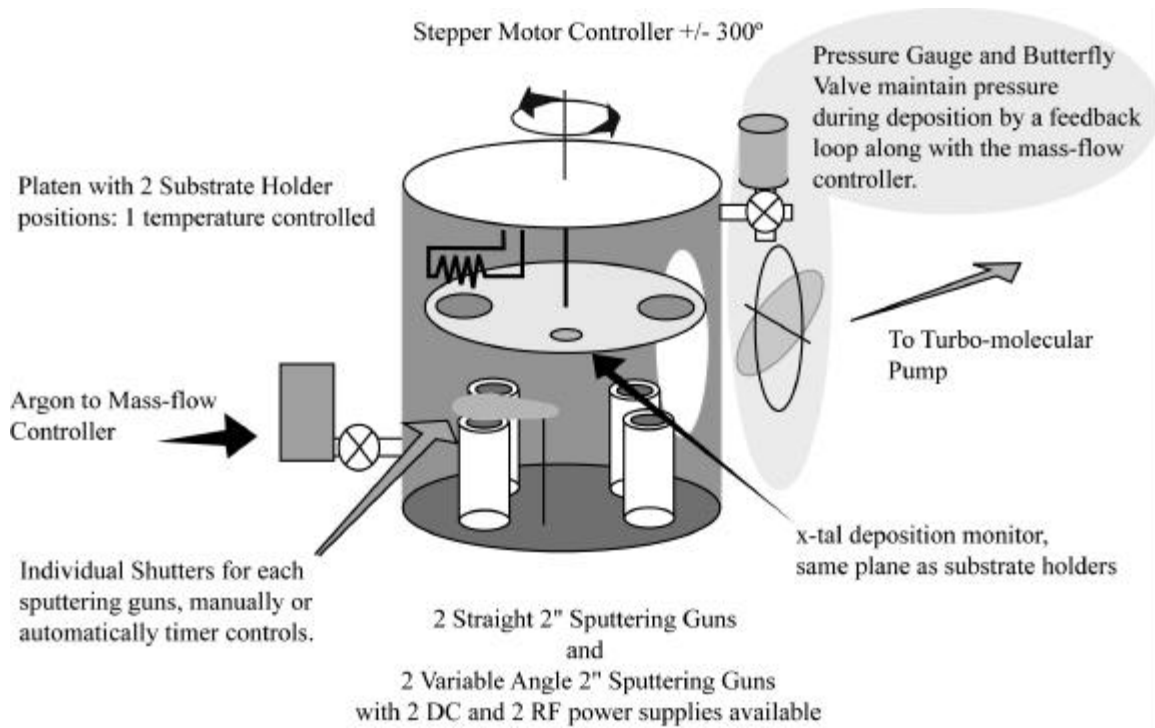


Figure 2.1 - Schematic representation of the UHV Sputter Deposition System utilized in this research. Note that a computer equipped with digital I/O, A/ and D/A converter cards automates much of the controls.

a 'race track' around the center of the target. A disadvantage of this variation is that the target suffers from non-uniform wear since the 'race track' region is sputtered away much faster. Non-uniform wear causes inefficient use of the target material. In addition, the magnetron sputtering guns have to be modified depending on whether the target material is strongly ferromagnetic or non-magnetic.

In fabricating high quality GMR structures, it is necessary to eliminate impurities in the films. This goal requires the vacuum to reach UHV (Ultra High Vacuum) base pressures. Typical pressures of 5×10^{-9} Torr are possible after overnight bake-out of the chamber at 100 ° C. The system is equipped with a 500 l/s turbo-molecular pump as well as a Ti gettering pump. All high vacuum pumps are oil free. Possible contamination during rough pumping of the chamber is avoided by an automatic pneumatic valve, which is set to close at 0.5 Torr. These automation features are described in Appendix A. During sputtering, high purity Ar gas (99.9999%) back-fills the chamber. After the deposition of one layer, the surface is susceptible to absorption of various contaminants [Stu83]. To minimize time between deposition of layers (with repeat layers as high as fifty or more), an automated system utilizing a personal computer drastically reduces time and error. By incorporating stepper motor controls to position a substrate over the relevant sputtering gun, and by controlling the gun power supplies and shutter controls, deposition of successive layers is accomplished within 10 seconds. Automation also conserves target material by lowering the power supplied to idling guns. To increase throughput, the use of a load lock drastically increases the up time of the system. Typically, much of the depositions were conducted at 2 mTorr of Ar with Ar flow of 20 sccm (standard cubic

centimeter per minute) and DC/RF power between 5 W to 100 W, resulting in deposition rates from 0.2 Å/s to 2 Å/s, depending on the material (see Chapter 4).

1.1.2 Evaporation deposition

Evaporation is another PVD process. Unlike the momentum transfer mechanism in sputtering, evaporation achieves vapor phase for adatoms by heating the source material to temperatures at which the source material's vapor pressure is high. Often, this temperature is above the melting point. Typical melting points for materials used in GMR structures vary from 1768 °C for Co to 3269 °C for Ta (used as a buffer layer for many multilayer systems). Such temperatures can be achieved by resistive heating in case of thermal evaporation where a tungsten boat is heated by passing tens of amperes of current. Electron-beam heating may also be used in which a heated filament creates electrons that are typically guided to target material by magnetic and electric fields.* In this study, thermal evaporation of Ni was found to be difficult due to the requirement for very high currents. Thermal evaporation was generally used to quickly deposit contact leads of Au/Ge alloy. These provided low resistivity and good coverage. Thermal evaporation was performed after reaching base pressures of 2×10^{-6} Torr. Currents ranging from 40-60 Amperes (Voltage of 1 to 1.5 V) were applied to the W boat, which held the material. The rate was not monitored but the deposition process was stopped by monitoring the frequency changes of the 6 MHz quartz crystal monitor.

* Molecular Beam Epitaxy (MBE) using Knudsen Cells (typically resistively/radiatively heated) have been used extensively and successfully in preparing high-quality single crystal magnetic thin films and multilayers elsewhere [Far98]. Such evaporation of sources to deposit magnetic materials was not used, and will not be described here.

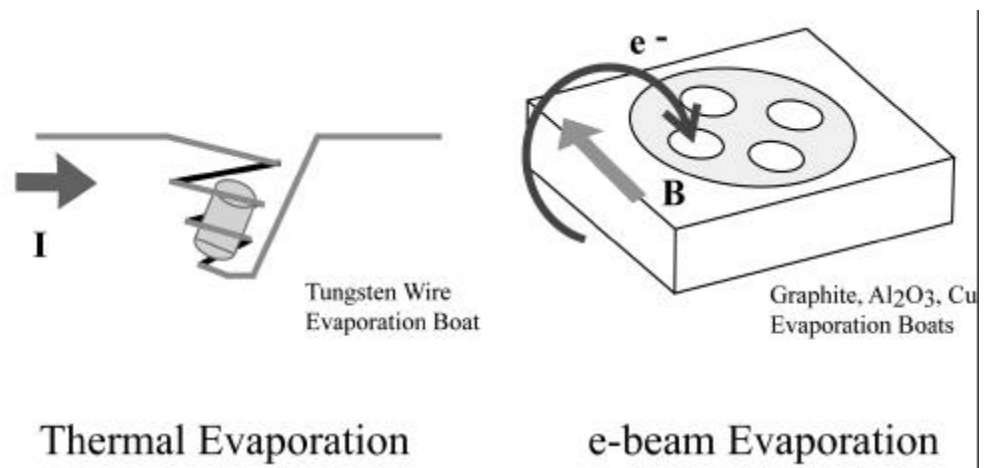


Figure 2.2 - Schematic representation of two types of evaporation utilized in this research. In thermal evaporation, the external power supply maintains a current upwards of ~ 30 A. In electron-beam evaporation, four crucibles were available for deposition by rotation, allowing for deposition of multi-layer structures.

The electron-beam was primarily utilized to evaporate materials and to deposit magnetic thin films and multilayers. The electron-beam source (Fig.2.2) allows for four materials that are rotated to deposit various materials in various orders. The electron-beam was initially swept in a circular pattern to evenly melt the material. When the electron-beam evaporated magnetic materials in 270° deflection geometry, precautions were taken to vary the electron-beam position during the evaporation. The control fields required to center the electron-beam at room temperature and during deposition are different, according to the degree that the magnetic field associated with the source disappears above the Curie temperature. The quartz-crystal deposition monitor controls the deposition rate by a feedback scheme. The shuttering mechanism does not engage unless a pre-set steady-state rate condition is met. Typical base pressure of the system is 1×10^{-9} Torr, which rises to $\sim 1 \times 10^{-7}$ Torr during deposition. Typical deposition rates were 0.5 Å/s for Ni for 8.5 keV with an electron current of 50 mA.

1.2 Patterning Techniques

The basis of the patterning techniques used in this work has been previously developed for semiconductor IC applications. Patterning required for this study ranged from tens of nanometers to hundreds of micrometers. Such a wide range required the use of electron-beam lithography, photolithography, and shadow deposition masks. It was necessary to use electron-beam lithography to pattern feature sizes as small as a few tens of nanometers [Cho96, Par97]. It was also necessary to pattern millimeter-sized contacts, which was accomplished using simple deposition masks or optical lithography [Sha89]. While masks and lithographic techniques allow the definition of patterns on samples, transferring such patterns requires other techniques such as dry etching or a lift-off

process [Shu88]. For pattern transfer with a deposition mask, patterned stainless steel foils were used for macro-sized features (>1 mm).

1.2.1 Photolithography

Photolithography was used here primarily for definition of contacts and leads whose sizes are on the order of hundreds to thousands of micrometers. With the advent of specialized resist materials, developers, and solvents, the main limitation of photolithography is wavelength of light. Due to diffraction, minimal feature sizes are related to the wavelengths of the light. Typical steppers use Hg-arc lamps whose spectrum has various lines (350-450 nm) available for exposure [Bow94]. With a proper light source, the design of optics requires considerable effort to aptly avoid problems with depth of focus and numerical aperture (NA), which is directly proportional to resolution. In the present research, various light sources including a commercial available Carl Zeiss stepper (Fig.2.3(a)) and a light source from a microscope were used as part of contact-proximity printing.* All light source powers were individually measured to determine exposure times for particular photoresists.

Resist comes in two types, either positive or negative. This categorization describes whether the resist, a polymer in solvent when spun onto the substrate and exposed to light, cross-links, or the resist molecules' bonds break. In positive resist, areas exposed to light will cause the bonds to break, which allows a developer solution to dissolve the exposed area. In the present work, mainly positive resists were used, which

* Other geometries include scanning projection printing and reduction step-and-repeat systems [Bru79, Buc89]. There is also considerable research into higher resolutions such as phase-shift mask techniques [Lev82].

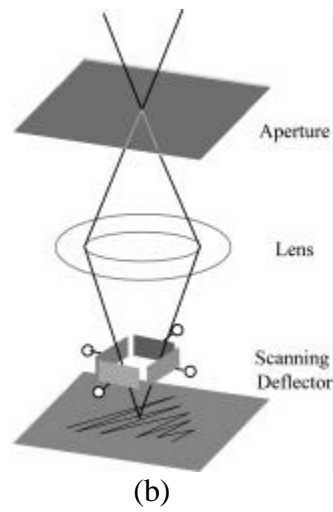
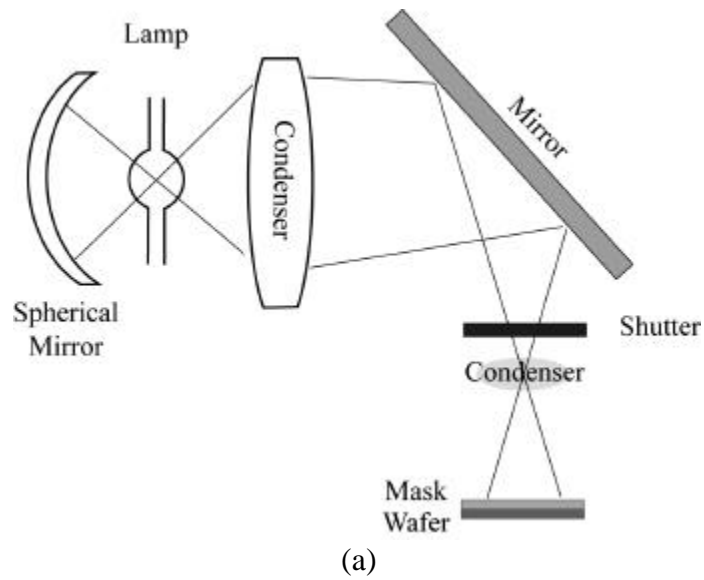


Figure 2.3 - (a) Schematic of a contact-proximity printing stepper such as the Carl Zeiss Stepper used in this work. In other applications, where feature sizes are in the order of millimeters, other light sources such as from an optical microscope were used. (b) Schematic of electron-beam writer used in this research.

usually have a superior resolution than negative resists. Positive resists can be further categorized into two types: Acrylates (or Diazoquinone) and Novolac.

Uniform application of resist is accomplished by spin applying the resist. The substrate is placed on a chuck and held by a vacuum pressure on the backside. The resist diluted to the proper viscosity by a solvent is dropped onto the surface of the substrate. The substrate is spun (several thousand revolutions per minute (rpm) depending on the viscosity of the resist and the desired thickness). Once the resist is uniformly applied, it is baked out in an oven at $\sim 100^\circ\text{C}$ up to thirty minutes. A hot plate at slightly higher temperatures for ~ 60 s may be used in place of an oven. The hot-plate method was used mostly in this study when defining contacts and leads in order to minimize thermal exposure to the underlying magnetic structures.

Once the resist is ready, the sample is aligned to a mask and exposed. A ferric oxide mask was used as opposed to a typical chrome mask. Ferric oxide is partially transparent to visible wavelengths and allows the user to align the sample and pattern more easily for unconventional exposure geometries, i.e., under an optical microscope light source. After exposure, the resist was developed using the recipe recommended for the particular resist. Rinsing the sample in de-ionized water (DI H₂O) stopped the development process. All of the above steps were conducted under light sources covered by a yellow filter to minimize background exposure of the resist.

1.2.2 Electron-beam (e-beam) lithography

As stated earlier, a major limitation of the photolithographic process is the wavelength of the light source, typically 350-420 nm for Hg-arc lamps. Wavelengths of electron-beams are four to five orders of magnitude shorter than the UV radiation found in

photolithography. Existing equipment can be used to achieve a fine focus of tens of angstroms and to scan the electron-beam, manipulated by several bit D/A converters. In this work, converted SEM (with tungsten filament as the source of electrons, thermal emission) was used for writing (Fig.2.3(b)). It lacked the automated sample stage manipulation found in many commercial systems.

In this research, poly(methyl methacrylate), PMMA (a common resist material* for electron-beam lithography), was primarily used (typically 2-4% thinned by chlorobenzene). After application, 'bake out' required long periods (six hours at 160° C). A copolymer, poly methyl methacrylate-methacrylic acid (PMMA-MAA, typically 9% thinned by 2-ethoxyethanol), that has a different sensitivity than the PMMA that was baked at the same temperature for one hour was also used. Both were spun applied to the substrate at 5000 rpm for 60 seconds. After the successive application and baking of PMMA-MAA, first, then PMMA, the resist was exposed in the converted SEM (JEOL JSM-6400). The dosages and development conditions were experimentally determined. Dosages differed for the magnification at which the pattern was written and development was very sensitive to temperature (<20° C). Important components of the developer and rinse solutions are methyl ethyl ketone (MEK) and methyl isobutyl ketone (MIBK). Dosages and development recipes are better explained and listed in Master of Science Thesis by Timothy Schultz (Department of Physics, UF, 1998) [Sch98].

* PMMA is a positive resist. Commercial negative electron-beam suitable negative resist is available, but due to cost and toxicity of the substance, such resists were not utilized in this work. Negative resist would be valuable in generating certain patterns due to the scanning nature of exposure in electron-beam writing.

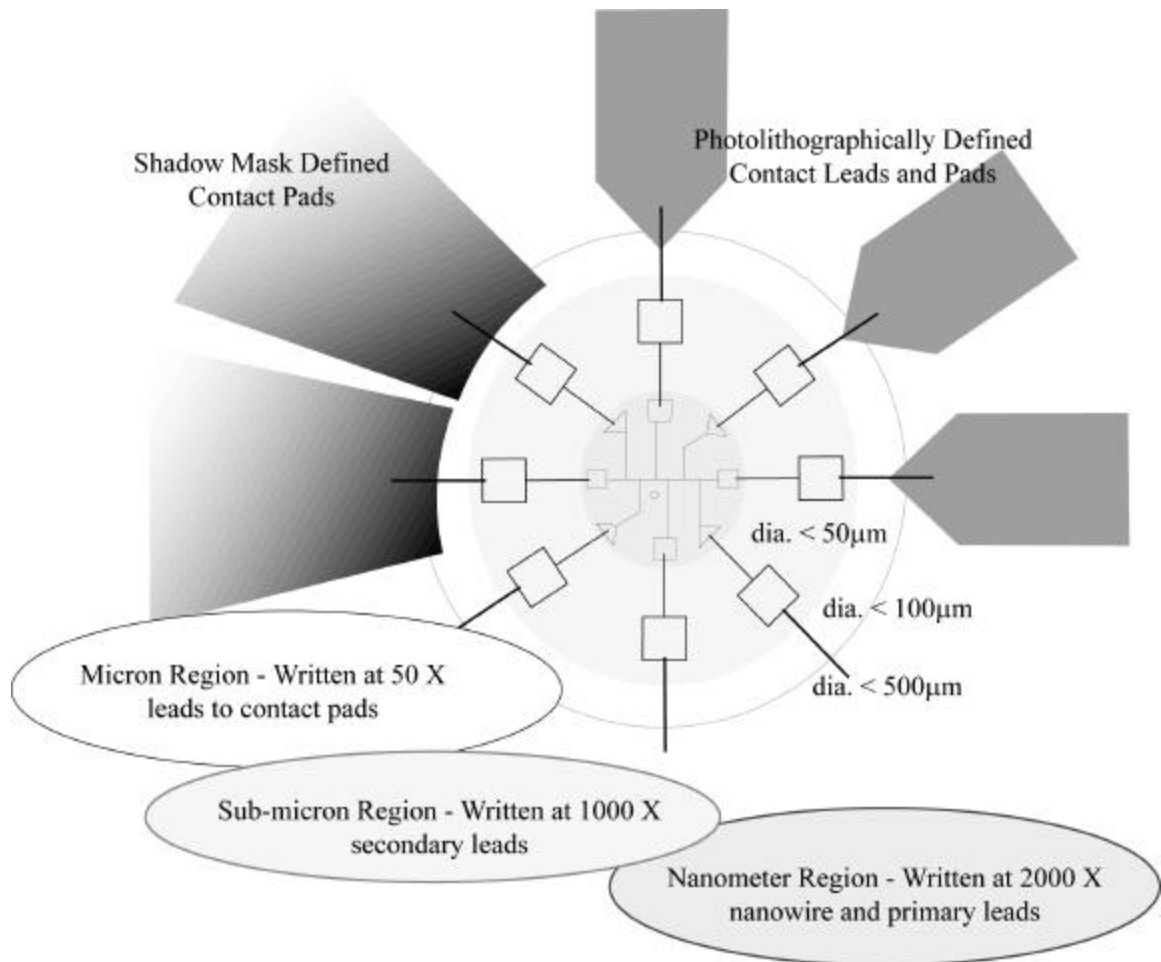


Figure 2.4 - Schematic of the nanowire structure electron-beam written with integrated leads. The figure is not drawn to scale although approximate sizes of differing levels are noted. The final leads and contacts (thermally evaporated Au/Ge) are defined either by deposition shadow mask (Au wire) or photolithography and subsequent lift-off of the organic resist.

In the actual writing process, setting the parameters on the SEM were more rigorously chosen to achieve the smallest feature sizes. Critical parameters include stigmatism and alignment of lenses, especially at higher magnifications than is called for in typical SEM procedures (i.e., stigmatism is set with wobble at 80,000X). Also, careful focusing was required to minimize hysteresis in the lenses. Focusing on a featureless PMMA surface was accomplished by using the electron-beam to burn a hole into the resist at the highest magnification of 300,000X. This feature was then used to focus the electron-beam. The shape of the hole also revealed the success of alignment and stigmatism settings. If all parameters were well matched, then the shape of the hole was perfectly circular. If x or y settings were less than ideal, the shape was more oval than a circle. Although the beam waist was in the order of 10 \AA , back-scattered electrons were major limiting factors in achieving the smallest feature sizes.* The smallest feature sizes were written at 2000X magnification at which point a D/A converter vector scanned a particular pattern generated by a computer running Nanometer Pattern Generation System (NPGS) software. The scan controls were externally controlled and the beam was brought to a particular point ('vectored') and a shutter opened and closed to deliver specific doses of electron charge. Other magnifications used were 1000X and 50X at which magnification leads to the wire structure were defined. These magnifications were found to be most favorable with minimal electrical noises.

* There are ways to minimize this effect such as using a thinner substrate allowing most of the scattered electrons to pass through. In addition, back-scattered electron profiles in the lateral direction are smaller for higher acceleration voltages. Electron-beam writing in this research is usually conducted at 35 kV.

The electron-beam lithographic techniques allowed the patterning of nanowire structures with integrated leads for further transport measurements (Fig.2.4). Depending on the dosage used and the development conditions (see Chapter 6), the width of wire ranges from 30 nm to 100 nm. Due to the use of vector scanning to write at differing magnifications, special care in the design of the test structure was necessary to ensure continuity from the smallest leads to the final leads. For example, there may be inherent offsets from 2000 X magnification to 1000 X magnification. Such offset tolerances required the use of polygon ends at the leads so that subsequent leads (written at lower magnifications) made physical and electrical contact with the previous leads. There were six leads that probed the nanowire and two leads that injected current. Each potential lead was separated by 4 μm . With this arrangement and by changing the exposure time when vectoring the nanowire, a series of five nanowires of differing widths was possible.

After exposure, the sample was developed in 1:1 MEK/IPA for 35 sec at 16° C, rinsed in 1:3 MIBK/IPA for 15 sec at 16° C, and finally rinsed again in IPA and DI H₂O. After development, an overhang structure was created due to differing sensitivities of bi-layers* (Fig.5.2(a)). The final steps necessary to complete a sample for measurement will be described in Chapter 5, since various techniques described in this Chapter in differing combinations can yield a nanowire structure.

Lift-off. Thus far, various deposition processes and fabrications of mask structures have been described. Defining contacts using a deposition mask is conceptually

* Multi-level resists have been used in the IC industry for applications where one resist layer does not meet all requirements [Tho94]. Typical layers perform such functions as planarizing layer, pattern transfer layer, and imaging layer [Mor79].

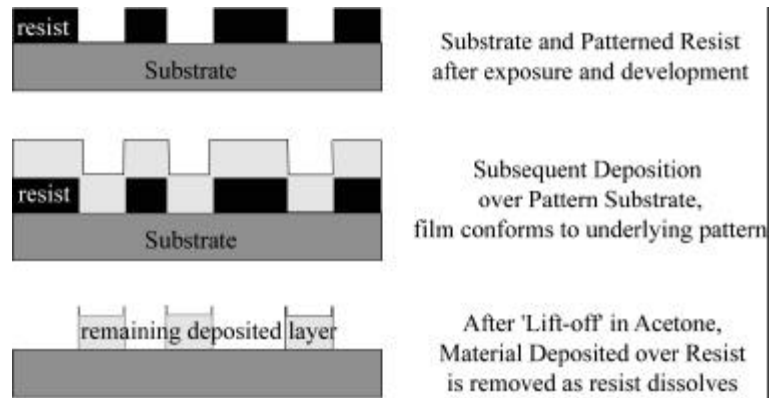


Figure 2.5 - Schematic of the lift-off process. Note that to enhance the structure of the remaining material and yield, the resist profile can be altered so that the opening at the resist surface is smaller than the exposed substrate area.

simple, where physical barrier is in close proximity to the sample substrate and blocks deposition. For the lithographically defined masks, the concept is the same except that the mask (photoresist or PMMA) is physically attached to the sample. Dissolving the resist material reveals the underlying patterned sample. In both cases, acetone is used to dissolve the resist to reveal the underlying pattern (Fig.2.5). Common commercially available resist removers are basic solutions that can alter the underlying material and thus were avoided. The sample is placed in an acetone bath and gently stirred. For the electron-beam defined structures, ultrasonic baths are avoided to minimize damage during lift-off.

1.2.3 Etching techniques

Patterning by a purely additive process has been demonstrated in STM systems, where atom level manipulations are possible; but in general, the patterning process includes an additional process (deposition) and certain specific removal processes (lift-off for the cases discussed thus far). Ideally, an etching process should transfer the pattern perfectly (i.e., that the resulting pattern should be exactly the same as the pattern itself) and have no detrimental effects on the underlying material. Ideal pattern transfer requires the etching process to be anisotropic. Etching processes occur by chemical means or by physical means and may alter the underlying material. A study to compare the effect of etching in terms of magnetic properties is described in Appendix B. Chemical etching occurs when a chemical reaction yields a volatile compound. Physical etching occurs when a momentum transfer process physically removes the material. Much more information and background into various etching processes can be found in Jewon Lee's Ph.D. dissertation (Department of Material Science, UF, 1997) [Lee97]. The two

methods of RIE (Reactive Ion Etching) and Ar ion-milling were used to pattern structures in this study.

Ar ion-milling. Ar ion-milling is an anisotropic etching process widely used in many applications [Muc94]. Much like the sputtering process, Ar is introduced into the vacuum chamber (2×10^{-4} Torr of background pressure from a base pressure of $\sim 2 \times 10^{-6}$ Torr) where it is ionized and accelerated to the sample. Typical beam voltages are set to 500 V with a beam current and a neutralizer current of 20 mA and 20-25 mA, respectively. Ar ion-milling is a relatively slow etching process and its rate does not distinguish much between various metals used in magnetic thin films. Ar ion-milling is a very reproducible technique. In the processing of nanowires, an Ar ion mill was utilized to etch underlying magnetic thin film while using patterned Nb as a sacrificial barrier (its removal is discussed in the following section). The etch time was experimentally found by depositing an equivalent amount of Nb on a glass substrate fashioned inside the chamber so that when the sample becomes transparent signifies the end of etch time.

Reactive Ion Etching (RIE). One of the differences between Ar ion mill and RIE is that, in RIE, the substrate is placed on the power electrode. This geometry offers higher energy ion-bombardment. In general, the introduction of gases enhances the etch rate where free radicals are primary etchant species [Meu79]. It has been previously established that RIE etch rates of magnetic materials such as Permalloy may be close to zero [Hsi97]. With this in mind, RIE was used to etch an Nb layer that was patterned by a lift-off process and used as a sacrificial barrier to pattern underlying material by Ar ion-milling. Nb was then etched in a parallel-plate reactor at pressures below 100 mTorr after the chamber was evacuated below 1 mTorr, where CF_4/O_2 are introduced with applied RF

power of 30 W. Samples were placed on a quartz disk centered on the system's lower metal electrode. An electrode was capacitively coupled to an RF source at 13.56 MHz.

2. Characterization

2.1 Dimension Measurements

2.1.1 Thickness measurement

Thickness is critical in magnetic systems. In multilayers of Co/Cu with an oscillatory coupling period of approximately 10 \AA , a variation on the order of a monolayer would reduce the anti-ferromagnetic coupling and, thus, the overall GMR. In this study, thickness was generally measured during the deposition by a quartz-crystal oscillator deposition monitor. The resonant oscillation frequency depends on the mass, which changes with the deposition of a film on the crystal. The deposition monitor in this study requires the input of density, a Z ratio of the material to be deposited and geometrical ratio. Once the deposition monitor is calibrated, the thickness of subsequent depositions is expected to be reproducible for the lifetime of the crystal.

For calibration of the deposition monitor, a film of thicknesses of hundreds of \AA were deposited and measured by a stylus profilometer (Tencor Alpha-Step 500 Surface Profiler). Other members of the group also contributed to the calibration process by measuring film thicknesses with RBS (Rutherford Back Scattering) [Cab97b]. The sputter deposition system was configured with the deposition rate monitor on the same plane as the substrates. For the evaporation systems, careful calibration was conducted. For the deposition techniques used, polycrystalline morphology with variation in thicknesses (surface roughness) on the order of tens of angstroms is expected. To measure such small

variations and quantify them as a root mean square (RMS value), Atomic Force Microscope (AFM) with a height resolution of 0.1 Å is used.

2.1.2 Linewidths

Although stylus profilometers are excellent in thickness measurements, due to the stylus movement mechanism, measuring dimensions along the plane of the sample is limited. To measure linewidths, Atomic Force Microscopy (Burleigh ARIS-3300 Personal AFM) with lateral resolution approaching 10 Å was generally used. A general caution for force measurements (stylus profilometer and AFM) is that for dimensions approaching tip dimensions (3 μm for profilometer and 100 Å for the AFM) and for sharp profiles, data include the convolution of the measuring tip geometry and the structure shape.

Scanning Electron Microscopy (SEM) does not suffer from such shortcomings for the dimensions considered in this research. SEM was utilized to verify sharp profiles of the processed structures for the smallest dimensions, which required SEM resolving power to measure linewidths down to an order of 50 nm. For the smallest sample widths, cross-sectional TEM micrographs, which give accurate measurement of widths, were also taken. Due to limitations, TEM was reserved for special investigations. SEM was used most often for measurement of linewidths.

2.2 SQUID Magnetization Measurements

SQUID (Super-conducting QuantUm Interference Device) is a super-conducting loop with one or two Josephson junctions in the loop's current path. A Josephson junction is a narrow physical gap or highly resistive area. Because of quantized states of the super-conducting ring, SQUIDS are able to resolve changes in external fields ranging

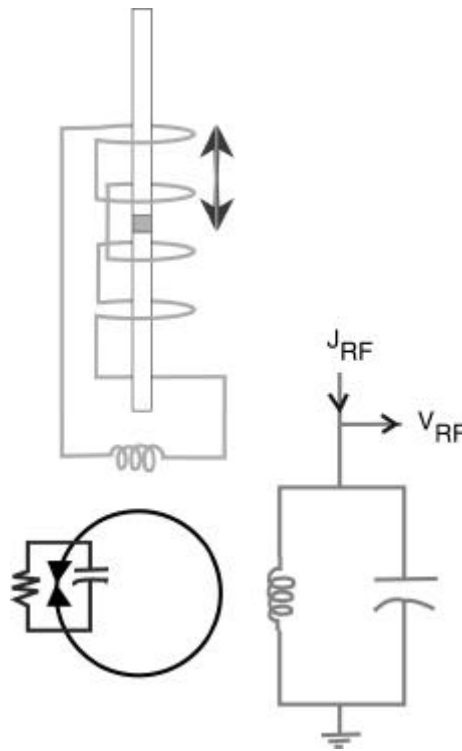


Figure 2.6 - Schematic of the SQUID magnetometer detection and electronics. Note that the sample is usually placed in a plastic sample holder, which is moved up and down along the coils to induce current in the circuit. The sample is centered in the middle of the coil by fully sweeping along the sample traverse range. During measurement, usually three sweeps are made for averaging purposes and with a scan length of 4 cm. Along the scan, 32 separate measurements are made, which are fitted to a signal of certain emu.

from small to large fields. The SQUID also exhibits excellent non-linear behavior associated with the Josephson junctions and works extremely well as a very sensitive current-to-voltage converter. Thus, the SQUID does not directly detect the magnetic field from the sample. In the commercial rf-SQUID system used in this study, the sample was moved through a series of super-conducting detection coils arranged as a second-order gradiometer (Fig.2.6). The sample moving through such arranged coils induces a current, which is inductively coupled to the SQUID sensor. The output voltage is proportional to the current flowing in the SQUID input coil [Van81].

The SQUID magnetometer is one of the most sensitive methods used to measure magnetization. The commercial rf-SQUID (Quantum Design MPMS-5S) has a range of 10^{-8} emu to 2 emu. Typical transition metal ferromagnets possess magnetization values on the order of 10^3 emu/cm³. Thus, theoretically, the SQUID magnetometer can detect a ferromagnetic particle with a diameter on the order of 2 μ m. Such theoretical limits are unattainable because of noise from electronics and background magnetic response (such as diamagnetic contribution from the sample holder and Si substrate).

2.2.1 Measurement procedure

The sample is placed in a plastic tube container (much like a drinking straw) and is secured by the straw's elasticity. Although the plastic straw may encompass magnetic contamination, as long as the sample holder is uniform along the length of the scan distance, it will induce no signal. The background signal ($\sim 10^{-8}$ emu at low fields < 200 Oe) is usually more than two orders of magnitude lower than the signal from the ferromagnetic thin films considered. Due to anisotropic effects, the plane of the substrate is aligned as parallel to the applied field direction as possible. During measurement, the

magnet is operated in the ‘non-overshoot mode’ where the set field is approached slowly and not exceeded. This precaution is important in ‘soft’ magnetic materials with small coercive fields. In addition, before measurement, the sample area is degaussed to remove any remnant magnetization, and the magnet is reset to remove any persistent current in the super-conducting magnet. The operation of the super-conducting magnet is by the persistent mode. In this mode, the persistent current in the super-conducting Nb alloy wires of the magnet provides the field. Fields are changed by applying more or less current by using a persistent switch. A persistent switch works by locally heating an area on the super-conducting magnet by which the action changes the super-conducting properties to normal. Although this operation is time consuming, it is much more sensitive since noise from a power supply is eliminated during measurement.

Before recording data, a nominal field is applied and a sweep of full length (16 cm) is done to center the sample. During measurement, the sample is swept at least three times (4 cm scan length) allowing three measurements of the SQUID response. For smaller signals ($<10^{-5}$ emu), the sample is swept five times. During each measurement, the computer fits a response by various iteration schemes and records the fit (emu value), deviation, temperature, time, and applied field, etc. Once the experiment is finished, the data is extracted and fitted, which requires subtracting diamagnetic contributions mainly from the Si substrate. Although the Si substrate constitutes the vast majority of the sample, the diamagnetic response is orders of magnitude smaller than the ferromagnetic response, especially at low fields. From most of the raw data in this study, hysteresis loops consist of a negative sloped component. This linear response can be fitted to extract $\chi_{\text{dia}} (<0)$, which is used to extract the ferromagnetic component.

$$M_{\text{measured}}(\text{H}) = M_{\text{ferro}}(\text{H}) + M_{\text{dia}}(\text{H}) \quad (2.1)$$

$$M_{\text{ferro}}(\text{H}) = M_{\text{measured}}(\text{H}) - \chi_{\text{dia}} \times \text{H} \quad (2.2)$$

For low field measurements ($\text{H} < 100 \text{ Oe}$), the sample area retaining magnetization complicates the matter. The specification for commercial SQUID magnetometer used in this research states a remnant field of around 20 Oe. This figure of merit depends on the history of the magnetic measurement itself. Thus, for ‘soft’ materials, the sweep was limited to $\pm 500 \text{ Oe}$. By calibration using a paramagnetic palladium sample, zero field offsets of few oersteds was found.

2.2.2 Notes on error in measurement

An error in SQUID magnetometer measurement is determined from the fit of the SQUID response. This error scales with the magnitude of the signal, and for the smallest signals considered, the deviation is always an order of magnitude less. User errors such as an imperfect alignment of the sample parallel to the applied field are minute. Such errors would correspond to asymmetry in the hysteresis loops. When coercive field values are reported, an average value between the left and right is quoted. Due to the nature of plotting hysteresis loops, error bars were not displayed to avoid cluttering a large ensemble of data points.

Table 2.1- Sample raw data file from a SQUID magnetometer experiment.

T(K)	H (Oe)	emu	Deviation
20	5	2.79e-05	3.76e-08
19.999	2	2.75e-05	2.23e-08
20.001	1	2.74e-05	4.34e-09

The error in the applied field and the temperature is minimal, as they are set by commercially available controllers. For each temperature setting, the sample is held at the temperature up to five minutes to ensure that the sample temperature is equalized to the temperature measured. For each field setting, the sample is held for at least ten seconds after the super-conducting magnet is charged.

2.3 Transport Measurement

Measurement of resistance or resistivity provides valuable information. The resistivity ($\mu\Omega\text{-cm}$) of certain elements at room temperature has been reported to be [Mea65]: Fe = 9.8, Co = 5.8, Ni = 7.0, Cu = 1.70, Ag = 1.61. Especially in metals, transport properties at room temperatures are dominated by phonons associated with the lattice colliding with conduction electrons. At cryogenic temperatures, impurity scattering and mechanical imperfection dominates. In ferromagnets, magnon-electron and electron-electron scattering dominate and can be characterized to determine the nature of the conduction band [Cam82]. In data for resistance vs. temperature, the resistance values are expressed as normalized to the room temperature value. This normalization is referred to as the resistivity ratio, which is a good indicator of the amount of impurity [Kit86]. For exceptionally pure bulk samples, the room temperature resistance can be as much as six orders of magnitude higher than the resistivity residual extrapolated to 0 K. Extrapolation can be complicated by a low temperature minimum associated with the Kondo effect, whose effect is usually small and is beyond the scope of this discussion [Kon69]. This effect is usually associated with magnetic ions in solution or magnetic impurities.

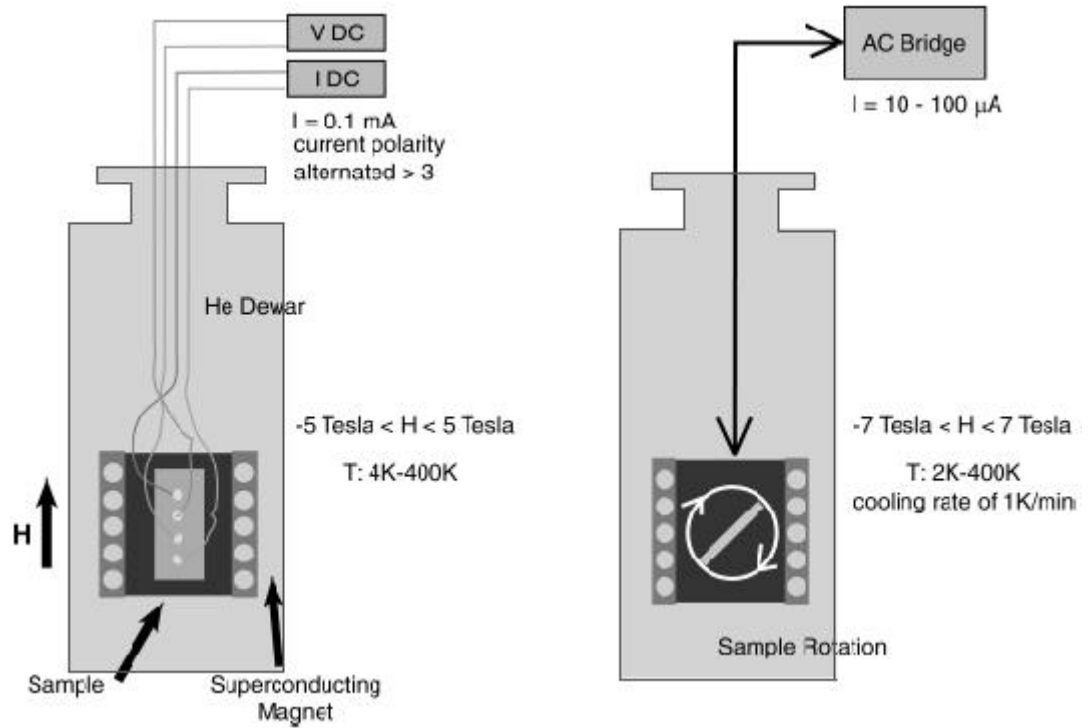


Figure 2.7 - Schematic of DC and AC transport measurement set-up

For thin films and patterned samples, surface scattering is also present. For the best 500Å Ni samples, a residual resistance/room temperature resistance of 0.2 was found (a resistivity ratio of five) (Fig.5.12). For the array of wire structures, although the geometry is well-defined, resistances vary. This indicates that some the wires carried current in parallel. For these reasons, absolute resistivity values will not be quoted for comparison purposes. In the nanowire samples, with only one wire carrying current, resistivity is found by

$$R = \rho l/a \quad \text{where } l \text{ is length and } a \text{ is the cross-section area. (2.3)}$$

No geometrical factors were used here in contrast to the four-point probe geometry measurement of thin films [Val54, Smi58]. When resistance was measured as a function of the applied field, the values were normalized to the saturation values (resistances at high fields). For MR calculated, the standard definition was applied [Die94, Fer94]:

$$\text{MR (or GMR)} = (R(H) - R_s)/R_s \quad (2.4)$$

Note that whether resistances or resistivities are used, the value is the same since the geometrical factors cancel.

2.3.1 Measurement set-up

Both DC and AC transport measurements (Fig.2.8) were conducted. Both measurements utilized four terminal geometry where two leads were used to inject and collect current and two leads were used to sense the potential difference. DC transport measurements were limited to thin film and a few arrays of sub-micrometer wires. The temperature controls and field controls for the DC measurement are part of the

commercial SQUID magnetometer, which allows the user external control of its functions.

The polarity of the current was alternated at least three times. This alternation eliminates any offsets in contact resistances and minimizes thermal conductivity effects [Cab97a].

AC measurements were conducted in a commercially available Quantum Design[®] PPMS (Physical Property Measurement System) with an optional sample rotation mechanism.

AC measurements were conducted at low prime number frequencies (11 Hz and 13 Hz) to eliminate background noise. Such sensitivity is crucial for characterizing nanowire structures where minimal injected current was used to reduce resistive heating.

2.3.2 Notes on error

Again like the magnetization measurement, more than one measurement was performed at a specific temperature and applied field. Special care as described above was used to minimize noise and fluctuations in the measurement. The commercially available controllers that are part of various systems controlled the temperature and the applied field. Temperature was usually set to one-thousandths of a Kelvin, and like magnetization measurements, the system was placed in idle for nominal periods to equilibrate the temperature and field. Sensitivity is an indirect function of the injected current since the greater the current, the greater the read voltage drop. To control cryogenic temperatures, there is a limit for current injected as the resistive heating load renders temperature control impossible. These limitations restrict injected currents on the order of a fraction of a milliamper, which gives a voltage signal on the order of hundreds of microvolts.

Commercially available voltmeters are well suited to measure such levels. For the AC measurement, injected current is much smaller along with the voltage, making it more

susceptible to noise. For such measurements, five measurements were read and plotted as an ensemble of data points.

Further specifics on the experimental procedures and their variations are presented along with data in the preceding Chapters.

CHAPTER 3 UNPATTERNED MAGNETIC THIN FILMS

1. Overview

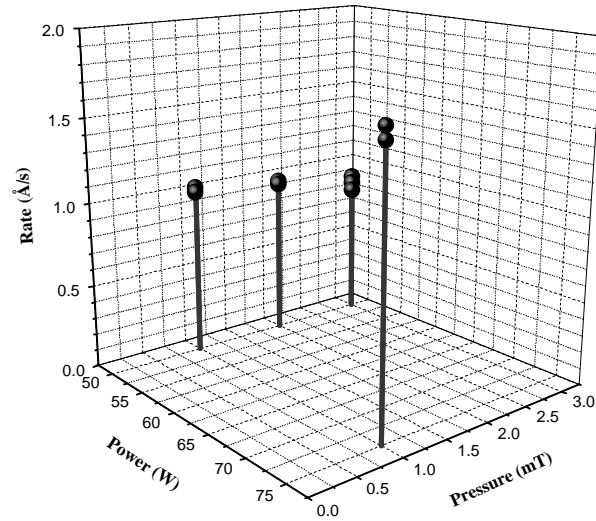
The magnetic properties of structures with dimensions between a few micrometers and a few tens of nanometers are reported in subsequent Chapters. In this Chapter, the properties of unpatterned magnetic thin film structures are reported. The unpatterned samples range from one layer of ferromagnetic thin film to multilayers of repeated bilayers of ferromagnetic and non-ferromagnetic spacer layers. Another important aspect to this study is the effect of the processing parameters on the structures, especially any thermal treatments ('bake-out') associated with lithographical techniques.

2. Magnetic Thin Films

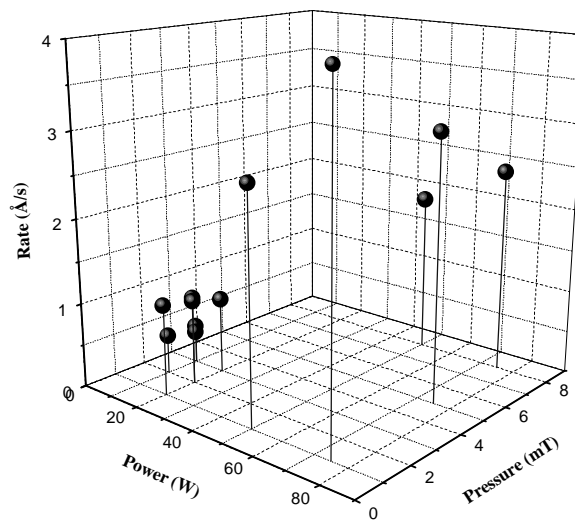
2.1 Single Layers of Transition Metals and Their Alloys

2.1.1 Deposition rates

Ferromagnetic transitional metals and their alloys, as reported in Chapter 1, play an important part in technological applications. Due to their electronic band structures, they respond differently in applied fields from diamagnetic and from paramagnetic materials. Responses of particular interest include magnetostriction and the anomalous Hall effect. Their AMR characteristics are of particular interest for transport measurements. These layers, combined with various non-magnetic spacer layers (both in thicknesses of only



(a)



(b)

Figure 3.1 - Deposition rate of (a) Co and (b) Cu as a function of Ar pressure (mTorr) and power (W) as measured by a crystal oscillator deposition monitor.

tens of angstroms), form multilayer structures that give a large MR response dubbed GMR [Bai88].

Deposition rates are dependent on both the power supplied and the pressure during sputtering. Figure 3.1 gives examples of Co and Cu deposition rate for various powers and pressures. Generally, the deposition rate linearly increases with applied power. In general, the deposition rate increased with a decrease in the pressure during sputtering, except for Ag and Ta (Fig.3.2). For most of this study, the deposition pressure was kept at 1 or 2 mTorr. A power setting of 100 W or less was used to prevent accidental heating of the sputtering guns. Deposition rates were relatively low ($< \sim 1 \text{ \AA}$) so that errors in shuttering time should have little to no effect on the total thickness deposited.

2.1.2 Effects of roughness and a buffer layer

There have been many studies on using a buffer layer to improve the magnetic properties of thin films [Par91b, Gri92, Tom92]. In this work, Fe was used as a buffer layer for cobalt based systems and Ta for Permalloy based systems. The importance of the buffer layer on magnetic properties may be deduced from the plot of the coercive field as a function of the thickness of Ta deposited prior to the deposition of 100 \AA of permalloy (Fig.3.3). The coercive field is at a minimum for a 100 \AA Ta buffer layer. Since Ta is a non-ferromagnetic material, the observed effect must be due to roughness of the thin film. However, AFM could not distinguish a difference in roughness between these samples.

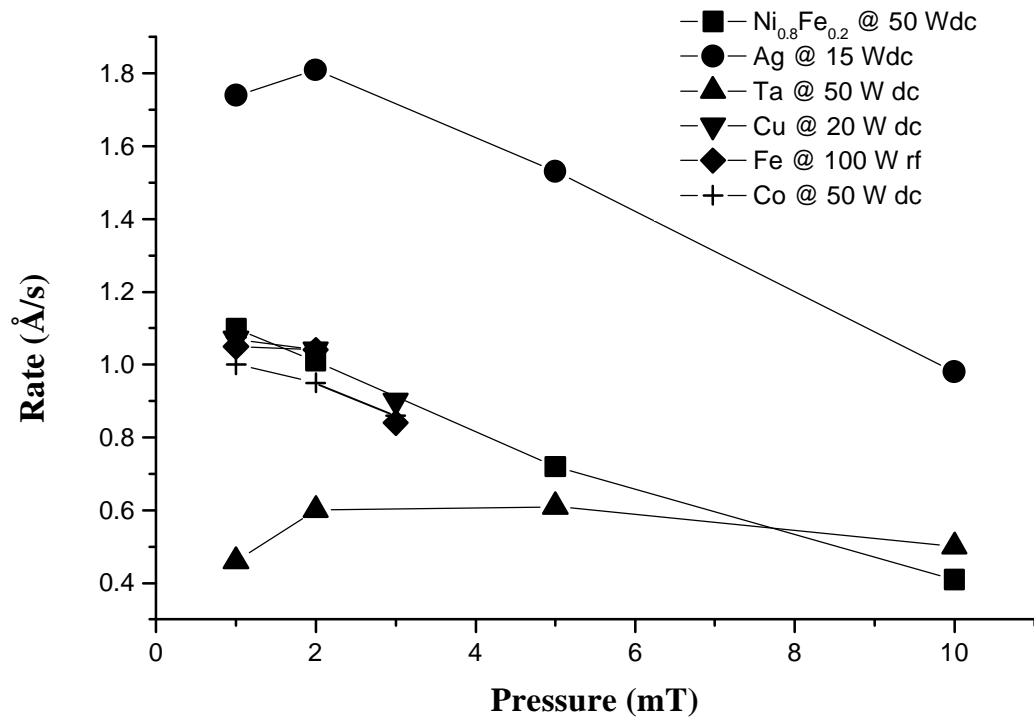


Figure 3.2 - Iso-power plots of deposition rates as a function of pressure for various materials compiled during various deposition runs performed for this research.

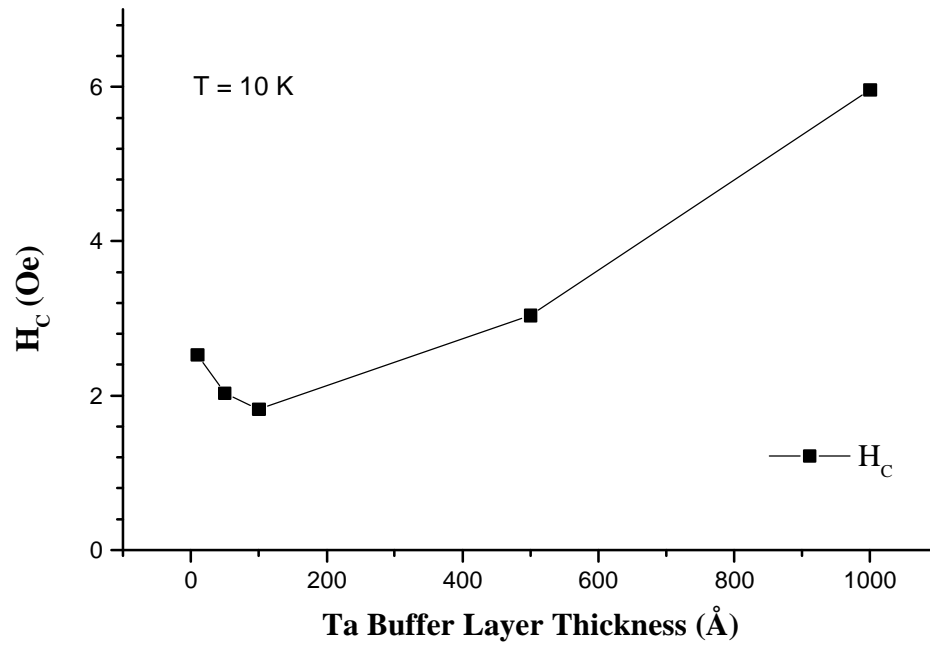
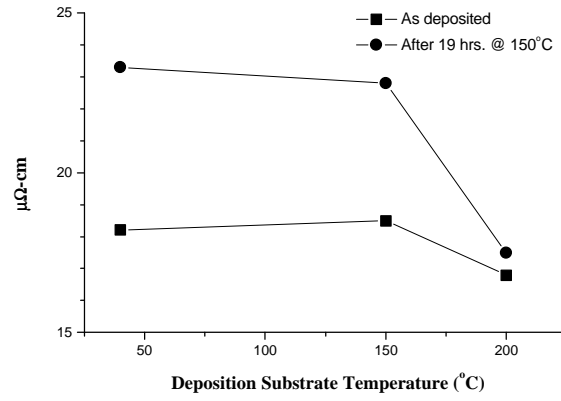


Figure 3.3 - Plot of the coercive field for Ta(x Å)/NiFe(100 Å)/Ta (20 Å) for various Ta buffer layer thicknesses.

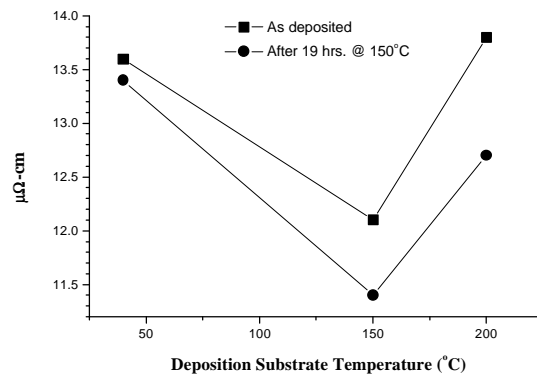
2.1.3 Effects of thermal treatment on magnetic thin films

Thermal treatment during or after deposition changes the microstructure of thin films and alters its transport and magnetic properties [Pet91]. Since an intended 'bake out' of the PMMA resist layer at temperatures as high as 160 ° C for several hours was required for patterning, changes in the properties of unpatterned films during heat treatments were measured. Films of Co and Ni at various elevated temperatures were deposited to determine if this would stabilize their properties (Fig.3.4). For Co and Ni, changing the temperature of the substrate (50°, 150°, and 200° C) caused 10% variations in resistivity. For Co, 150° C for 19 hrs caused resistivity to increase by 30% for deposition at 50° and 150° C, while a minimal increase (5%) was observed at 200° C.

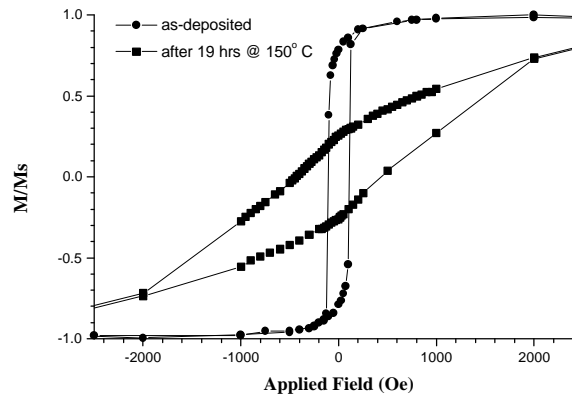
For Ni, changes in substrate temperatures caused +/-10% variation, but resistivity changed by < 5% for all samples after 150° C, 19 hrs. MFM (Magnetic Force Microscopy) images of the as-deposited and thermally treated Co thin films show an increase in domain size after the thermal treatment, which suggests grain size growth, since domain walls are likely to be pinned at grain boundaries [Boc95]. This growth is also evident in the magnetization measurement of 500 Å of Ni, since the remnant magnetization is much lower after equal thermal treatment. Lowering remnant magnetization is an indication of larger domains [Boo95].



(a)



(b)



(c)

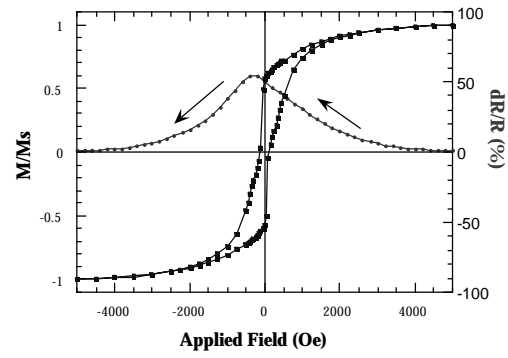
Figure 3.4 - Resistivity of 500 Å (a) Co and (b) Ni deposited at various temperatures and after thermal treatment of 150 °C for 19 hours. (c) Magnetization measurements of deposited 500 Å of Ni and after heat treatment.

2.2 Magnetic Multilayers

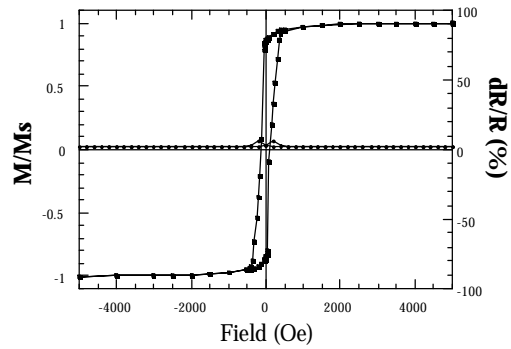
2.2.1 GMR multilayer stack

Co/Cu multilayers show one of the highest GMR values at room temperature, as high as 100% [Par91c]. The Co/Cu system response is controlled by an oscillating coupling mechanism, which varies as the spacer thickness (Cu) changes with a period of $\sim 10 \text{ \AA}$. This oscillatory response results from an anti-parallel alignment of magnetization at the first maximum of 10 \AA Cu spacer thickness, parallel alignment for a 15 \AA Cu spacer thickness, and another anti-parallel alignment around 20 \AA Cu spacer thickness. This switching continues for thicker Cu spacer layers. The coupling energy decreases at large Cu thicknesses until at very large Cu thicknesses, the layers are uncoupled. Thus, the highest reported values of GMR for these systems are at the first maximum with a Cu spacer thickness of around 10 \AA , with as many as forty repeated bilayers [Har94].

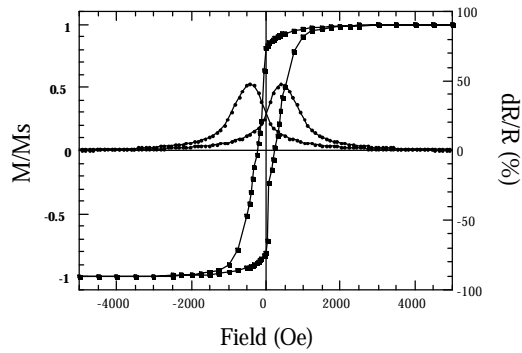
One of the first thin films made to test automation capabilities (Appendix A) of the UHV sputtering system is the Co/Cu multilayer. Deposition of these multilayers occurred for the following conditions: at 3 mTorr of Ar pressure with sputter gun powers of 10 Wdc for Cu (rate of 0.45 \AA/s), 50 Wdc for Co (rate of 0.9 \AA/s), and 100 Wrf for Fe (rate of 0.85 \AA/s). The bilayer was repeated twenty times with a fixed Co layer of 15 \AA and Cu spacer layers of 9 \AA , 15 \AA , and 20 \AA . These thicknesses correspond to anti-parallel, parallel, and anti-parallel alignment magnetization coupling, respectively. Magnetization and MR measurements are plotted in Figure 3.5. The GMR characteristic (negative magneto-resistance) is present for the anti-ferromagnetically coupled cases (a,c) with a first anti-ferromagnetic maximum (9 \AA (a)) GMR value of approximately 62% and with a second anti-ferromagnetic maximum (20 \AA (c)) GMR value of 54%.



(a)



(b)



(c)

Figure 3.5 - For an $\text{Fe}(50\text{\AA})/[\text{Co}(15\text{\AA})/\text{Cu}(y)]_{\times 20}/\text{Cu}(20\text{\AA})$ GMR multilayer structure with (a) $y = 9 \text{ \AA}$; (b) $y = 15 \text{ \AA}$; (c) $y = 20 \text{ \AA}$. Normalized magnetization and MR values.

2.2.2 Spin-valve structures

As mentioned in the introductory Chapter, anti-parallel alignment can be obtained by means other than anti-ferromagnetic coupling between the magnetic layers. Other methods, such as the use of $\text{Ni}_{0.8}\text{Fe}_{0.2}$ and Co layers as ‘soft’ and ‘hard’ layers, can be categorized as spin-valve structures. As seen in the above Co/Cu multilayer MR plot, a relatively large field is required (an order of several hundreds of Oersteds), which does not lend itself to sensing applications. The use of a ‘soft’ magnetic layer in spin-valve structures allows responses at low fields with high sensitivities, although the percent MR values are much less than the multilayer structures [Die94]. Unlike sandwich structures where a layer is pinned by another layer (usually by an anti-ferromagnet), for a spin-valve structure, spacer thickness should be large enough that the magnetic layers are not coupled. If the layers are coupled, their magnetization will likely rotate at the same fields, thus reducing anti-parallel magnetization alignment between the successive magnetic layers. If the spacer thickness is too large, the GMR value will fall as the total resistance decreases and much of the current in the CIP geometry is shunted through the spacer layer.

Spin-valve structures of $\text{Ta}(50\text{\AA})/\text{NiFe}(50\text{\AA})/\text{Cu}(x)/\text{Co}(20\text{\AA})/\text{Cu}(30\text{\AA})$ were studied to determine spacer layer thickness for optimum de-coupling (Fig.3.6). From the Figure 3.6, the MR values increase upon changing the thickness from 10 Å to 30 Å, then decreases at larger values. This initial increase is due to de-coupling of the magnetic layers. As the ‘soft’ and ‘hard’ layers are de-coupled, the ‘soft’ layer will rotate at lower applied fields than the ‘hard’ layer allowing for anti-parallel alignment of magnetization.

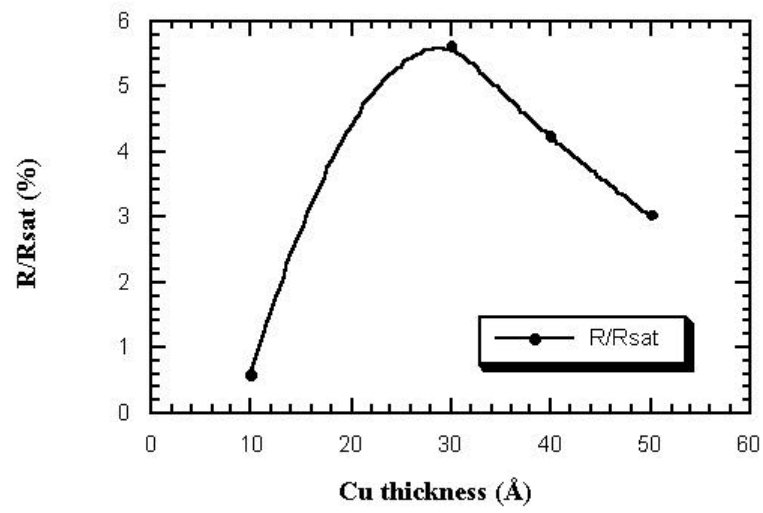


Figure 3.6 - Percent MR of Ta(50 \AA)/Ni_{0.8}Fe_{0.2}(50 \AA)/Cu(x)/Co(20 \AA)/Cu(30 \AA) as a function of spacer thickness at 10 K.

Again, as expected, the MR value decrease as the spacer layer gets thicker as more of the current is shunted through the spacer layer.

2.2.3 Effect of thermal treatment

The effect of thermal treatment on the characteristics of the GMR was determined by transport measurements. For single layered ferromagnets, an overall decrease in resistivity was reported above. A Co/Cu multilayer $\text{Fe}(50\text{\AA})/[\text{Co}(15\text{\AA})/\text{Cu}(20\text{\AA})/\text{Co}(15\text{\AA})]_x20/\text{Cu}(30\text{\AA})$ was placed in an oven for 19 hours at 150°C . Due to the relatively thin layers involved, the GMR value was expected to decrease as inter-diffusion occurred [Har93]. Inter-diffusion can cause a bridging of the successive magnetic layers, which will cause parallel magnetization by physical coupling. Indeed, a lowering of the GMR value after thermal treatment can be seen on Figure 3.7.

3. Discussion

Studies of deposition rates allow setting of suitable and relevant conditions, which allows a shuttering sequence to consistently reproduce thicknesses for layered thin films. Studies of the buffer layers effect on magnetic properties give more flat and conformal growth of subsequent layers. The relevance of other studies will become clearer in the following Chapters. The results gathered above constrain choosing various processings techniques and studies for patterned structures. Thermal treatment of magnetic thin films alters both magnetic and transport properties. In the case of a GMR film, the MR ratio decreased by approximately 20% from the as-deposited sample. Clearly, thermal treatments associated with types of processing such as 'bake out' of photoresist should be

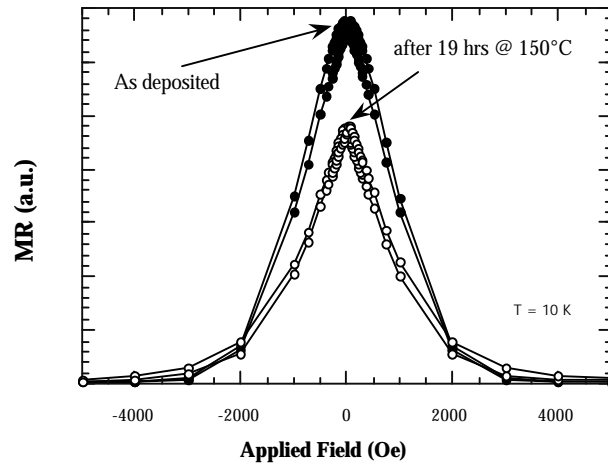


Figure 3.7 - MR of Fe(50Å)/[Co(15Å)/Cu(20Å)/Co(15Å)]x20/Cu(30Å) multilayer as-deposited and after thermal treatment.

avoided for underlying magnetic thin films. As mentioned in Chapter 2, lift-off could serve as an alternative. Also, to isolate shape effects, coupling between the successive magnetic layers may be warranted. In varying the spacer thickness in a NiFe/Cu/Co system, an optimal thickness was found.

In the following Chapter, patterning of spin-valve structures will be performed and characterized. The means of fabrication involves direct deposition and lift-off to minimize effects due to any thermal processing. This method allows many layered structures to be studied. From the results gathered in this Chapter, one of the structures chosen is a Co/Cu sandwich with a spacer layer of 50 Å Cu. Such thickness was chosen to ensure that the successive magnetic layers are not coupled. In addition, it has been demonstrated that a variation of 5 Å significantly alters the GMR values (Fig.3.5). Although spin-valve studies of varying Cu thickness showed that spacer thickness of 35 Å may suffice, 50 Å spacer layer may further ensure that physical coupling of magnetic layers does not occur at the edges of wire structures.

CHAPTER 4 SUB-MICROMETER SPIN-VALVE STRUCTURES

1. Overview

Background materials in magnetic structures and properties of unpatterned magnetic thin films have been discussed in the preceding Chapters. In the sections to follow, fabrication of spin-valve structures will be reported along with their magnetization and transport properties. Before discussion of patterned structures with minimum dimensions down to $0.5\ \mu\text{m}$, effects of the fabrication process would be discussed to show that there is minimal effects due to patterning and that comparison between various dimensions are justified. The patterning is mainly by direct sputter deposition and lift-off process, avoiding any thermal treatments to the metallic structure associated with lithographical and dry etching techniques.

In Chapter Two, limitation of electron-beam lithography was pointed out that samples of relatively large size ($>1\text{mm}^2$) with sub-micrometer dimensions are difficult to fabricate. Due to inability to pattern large areas, characterization techniques are limited to such as transport properties from which magnetic properties can be indirectly understood. As reviewed in the Chapter One, various research efforts have primarily used transport measurements for characterization [Hon95, Jia97, She96, Ade97]. For the Cavendish Laboratory group, magnetization measurements were performed using magneto-optical Kerr effect (MOKE) which utilizes focused light source to measure polarization change of

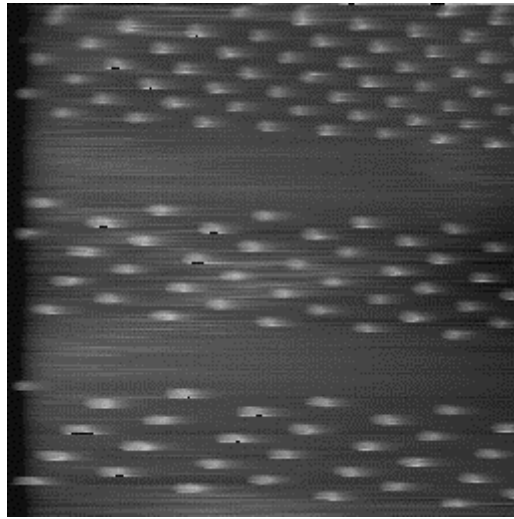
reflected light. This magnetization characterization give relative values and locally probes an area about the size of the light source. Although Nozaki et al and Piraux et al [Noz98, Pir97] have performed direct magnetization measurements, their studies differed than presented in this dissertation. Nozaki et al studied Co wires of 1 μm width separated by various widths (4 to 8 μm) patterned by electron-beam which dimensions are larger than studied here. Piraux et al wire structures were oriented for CPP measurements where the normal of the layers were parallel to the wire axis while CIP geometries are considered in this study.

In this study, specialized lift-off processing resulted in arrays of wires, which were patterned by photolithography with minimum feature sizes down to 0.5 μm . The use of photolithography allows exposure of large areas resulting samples suitable for SQUID magnetization measurements. The sample size requirements can be illustrated by considering that SQUID magnetometers are sensitive to 10^{-8} to 10^{-9} emu. Typical value of magnetic saturation of Co is 1400 emu/cm³. A wire of 1 μm width and length of 100 μm with thickness of 500 \AA would yield a saturation signal of only 7×10^{-9} emu. With such a sample, an experimenter using SQUID magnetometer would be hard pressed to even see the signal over background noise and to plot magnetization vs. applied field would be almost impossible.

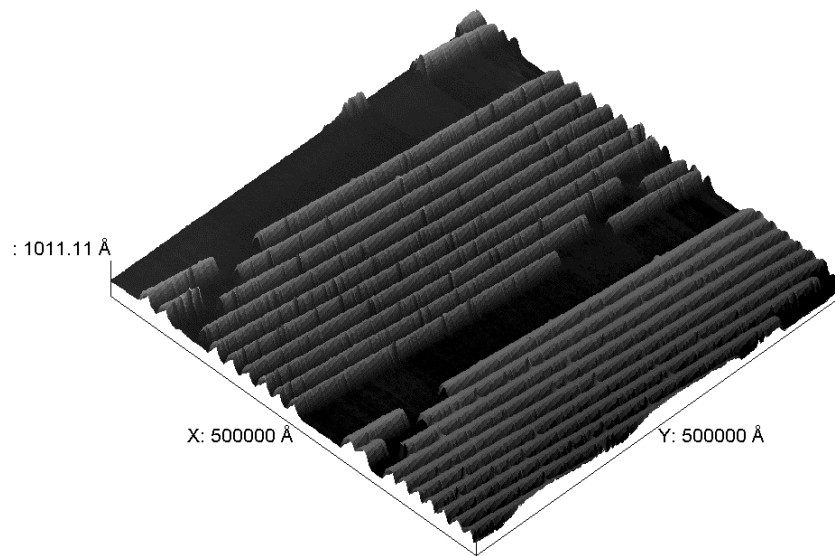
2. Experimental Specifics

2.1 Feasibility Studies

The fabrication of sub-micrometer arrays of wires (ranging from 20 μm down to 0.5 μm) was performed by MCNC (Microelectronics Center of North Carolina) in



(a)



(b)

Figure 4.1 - AFM micrographs of MCNC Lift-off test structures. (a) 0.6 μm structures of various lengths. (b) 0.6 μm lines with various line-spacing. Test structure was sputter-deposited at 2 mTorr.

Research Triangle Park, North Carolina. They provided wafers already patterned and developed resist structures for lift-off processing (Fig.4.1). Due to the fact that lift-off processing needs to be employed, certain experimental parameters had to be determined before carrying out the design and implementation of specific structures for the experiment. For example, sputtering is a major means of depositing magnetic thin films. Sputtering requires the presence of background gases to be ionized and accelerated for physical vapor deposition to occur. Due to the presence of gases at pressures of a few millitorrs, atoms are scattered resulting in poor collimation.

For thin film depositions, poor collimation has no ill effect since flux is usually constant over a certain area. An elevated substrate temperature can increase the surface mobility of adatoms and rotating the substrate can ensure an even flux along all areas to be deposited. The above solutions can improve uniform thickness over the sample area, but they are not applicable in this case. For lift-off processing, developed resists exist on substrates. While deposition at elevated temperatures, resists may degrade. Poor collimation presents a problem if the substrate is not flat, especially if a substantial step like structure is present where shadowing effects can reduce the deposition rate or result in incomplete, non-uniform coverage [Sch88]. Lift-off processing requires adatoms to traverse through an aperture opened by selective removal of the resist material. A solution to poor collimation is the use of a physical barrier such as a chimney whose length to aperture ratio improves collimation. Such solutions have been found to severely reduce deposition rate and are only effective for very small areas [Par97].

Fractional changes in deposition rate and optimum deposition conditions to minimize shadowing may be different for varying linewidths. It seems feasible for a

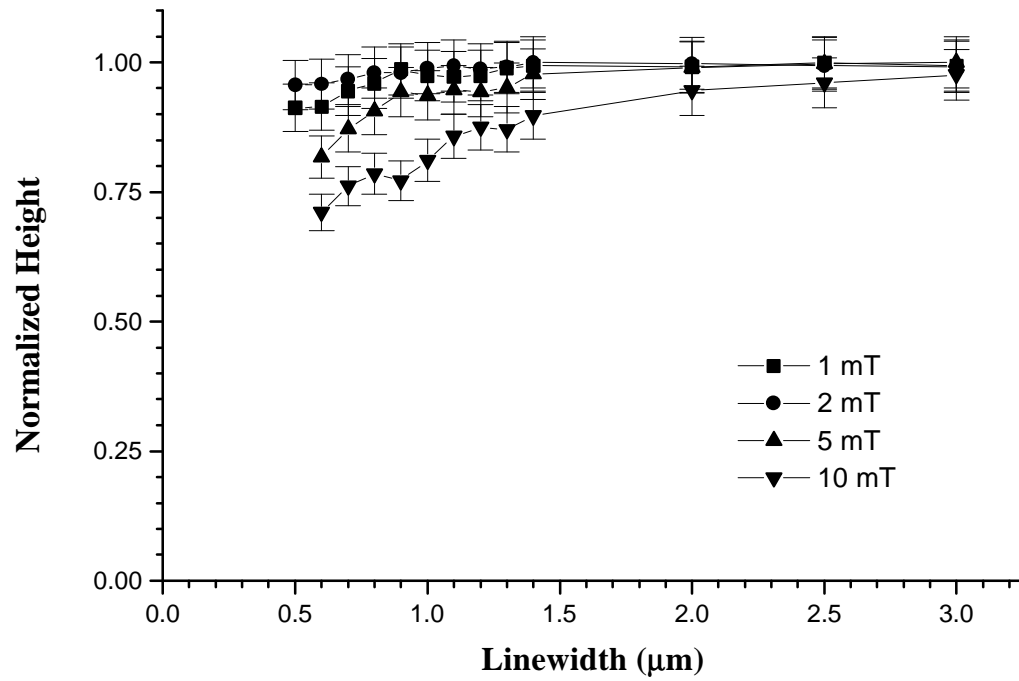


Figure 4.2 - Normalized height vs. linewidths for various sputtering gas conditions. Note that a single data point represents an average of five measurements using profilometer and the error is within 5%. For 5 mTorr and 10 mTorr, the smallest feature was lost during lift-off.

structure with large open channel dimensions to have little effect compared to a structure with small open channel dimensions. Shadowing would be expected to be more severe for sputtering with high Ar pressures. As deposition pressure is increased, sputtered and sputter gas atoms collide at higher probabilities, thus increasing angular distribution of arriving species. Significant variations of thicknesses can confuse any correlation between anti-ferromagnetically coupled magnetic multilayers.

In the test cases, NiFe/Ag multilayers with Ta as a buffer layer were deposited on a test pattern of varying linewidths from 0.5 μm to 3 μm . The deposition power was kept constant (Ta at 100 Wrf, Ni_{0.8}Fe_{0.2} at 50 Wdc, and Ag at 10 Wdc) and background gas pressure was studied over a range from 1 mTorr to 10 mTorr. After deposition, lift-off was accomplished in a bath of commercially available resist stripper at an elevated temperature of 60° C in an ultrasonic bath for fifteen minutes followed by a rinse in isopropyl alcohol. The resulting thicknesses of the deposited layers were measured using a profilometer. Thickness vs. linewidths for various Ar pressures is shown in Figure 4.2. For an Ar pressure of 10 mTorr, gas phase scattering and shadowing effects reduced the thickness of 0.6 μm features by ~30%. Presumably, this reduction resulted from the fact that deposition on the sidewalls prematurely closed the aperture. There was little difference between the 1 mTorr and the 2 mTorr conditions within the error of the measurement. To ensure a stable plasma during sputter deposition, 2 mTorr was chosen as the deposition pressure.

2.2 Design of Test Samples

Once it was established that sputter deposition was compatible with the lift-off process, various structures were designed for study. For SQUID magnetometry, the

pertinent design parameter was for the sample to possess at least 10^{-5} emu, well within the sensitivity of the measurement. With this parameter and again using Co saturation values (~ 1400 emu/cm³), the total area required is 0.12 cm by 0.12 cm assuming a total thickness of 50 Å (volume of $\sim 7 \times 10^{-9}$ cm³). Considering the effects of length to width ratio, a wire length of 500 μm was chosen for patterning so that the length is much greater than all the widths considered. For transport measurement, injected current densities can be substantial. Again, using a thickness of 50 Å and widths of 0.5 μm, a nominal current of 0.1 mA results in densities of 4×10^6 A/cm², which can heat and damage the wire. Therefore, an array of wires in parallel was designed. Using this approach, total injected current was dispersed. Allowing an area of 0.5x0.5 mm² for arrays for transport measurement, the following geometrical constraint was used: (number of lines) x (linewidth) + (number of lines – 1) x (space width) = 0.5 mm. Thus, the current density for 0.1 mA total injected current is reduced to 1.2×10^4 A/cm².

With a limited design space of 1 cm², the number of samples for SQUID magnetization measurements were limited to widths of 0.5, 0.8, 1.2, and 2.2 μm. Arrays of 0.5x0.5 mm² were fashioned for transport measurements of sixteen different wire widths ranging from 0.5 μm to 20 μm. As described in Chapter 2, leads and contacts were fashioned from thermal evaporation of Au/Ge after a short ion mill etch and lift-off. Ar ion-milling was performed immediately before deposition to clean the surface to ensure good conductivity between the contact leads and the wires. The contact leads cross the array perpendicular to the axes of the wires. The resulting reticle design is shown in Figure 4.3. During characterization, the samples were oriented with the axis of the wires

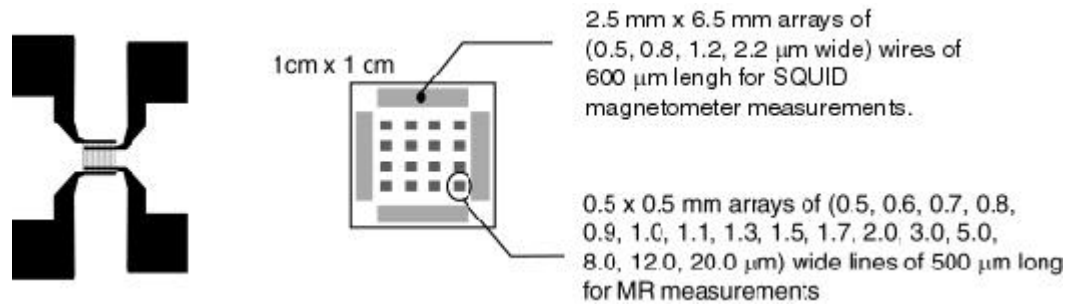


Figure 4.3 - Left: schematic representation of the contact lead pattern over the 0.5 mm x 0.5 mm array for MR measurement; Right: reticle layout for the MCNC sub-micrometer lift-off structures to be characterized by MR and SQUID magnetometer of various widths with a length of 500μm.

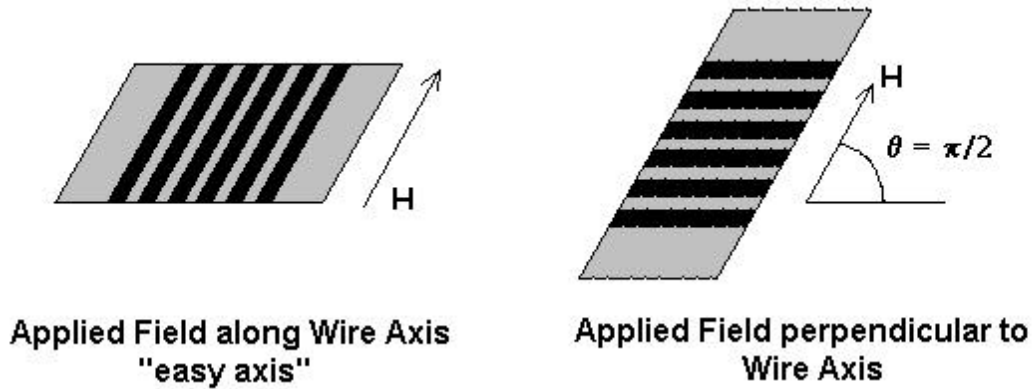


Figure 4.4 - Two orientations considered for SQUID magnetometer measurements. Left: axis of wires is along the applied field direction (H), 'easy axis.' Right: the axis of wires is perpendicular to H , 'hard axis.'

either parallel or perpendicular to the applied field, while the substrate lay in the plane with the field (Fig.4.4).

3. Properties of Sub-micrometer Array of Wires

3.1 General Properties of All Sub-micrometer Wire Arrays

3.1.1 Physical properties

As mentioned above, a stylus profilometer was used to measure the thickness of these wire structures. Profile characterization was not possible using the stylus profilometer due to the large radius (3 μm) of the stylus. AFM images and scans reveal well-defined sidewalls without the presence of ‘rabbit ear’ structures, a remnant of bridging between the layer over the resist and the layer over the substrate. This feature signifies minimal interaction between the layer on top of the resist and the substrate. With the thickness to width ratio being very small for these structures, cross-sectional SEM to study the sidewall profiles would be difficult. Cross-sectional TEM of a Co/Cu sandwich structure with an Fe buffer layer has been performed (Fig.4.5). Due to the atomic number and weight of Fe, Co, and Cu being similar, a clear distinction of individual layers was not evident. Figure 4.5 shows two micrographs, one near the center and one near the sidewall of the wire structure. The cross-sectional micrograph near the edge shows a slight sloping, which can possibly be attributed to shadowing effects near the edge. This sloping can be best quantified as a loss of approximately 40% extending 800 \AA from the edge.

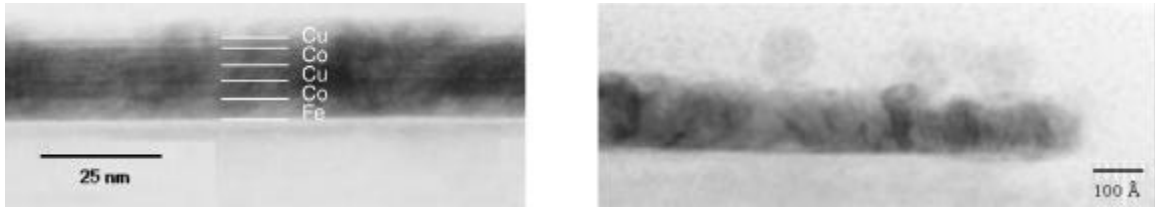


Figure 4.5 - Cross-section TEM of an Fe(50Å)/Co(50Å)/Cu(50Å)/Co(50Å)/Cu(20Å) structure. Left micrograph shows the cross-section far from the edge (right micrograph). The edge structure shows slight sloping due to shadowing effects extending approximately 800Å from the edge. Note that due to similar Z values of Fe, Co, and Cu, it is difficult to discern individual layers.

Table 4.1. The table below is an example of data required to formulate the magnetization value for each sample. W1 and W2 are width measurements; L1 and L2 are length measurements. The space to line ratio for the wires is 2:1 for all widths.

ID	w1(mm)	w2(mm)	l1(mm)	l2(mm)	A(mm ²)	Emu (10 ⁻⁵)	emu/cc
film	2.59	2.56	6.92	6.82	17.690	12.584	889.19
0.5	1.93	1.53	5.91	5.92	10.233	2.4900	912.49
0.8	2.58	2.52	6.11	6.18	15.670	3.5405	847.29
1.2	2.54	2.05	6.69	6.57	15.216	3.6405	897.21
2.2	1.98	1.91	5.08	5.38	10.172	2.2900	844.20

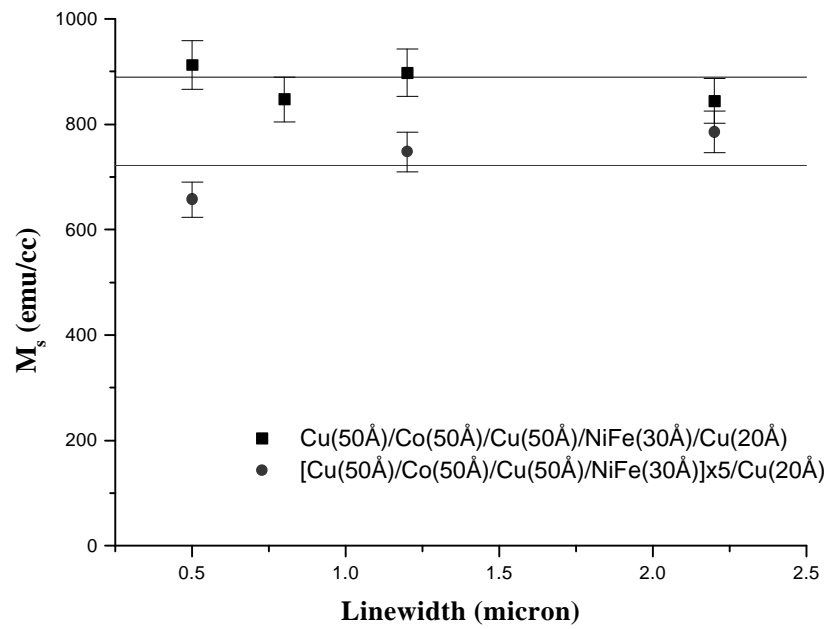
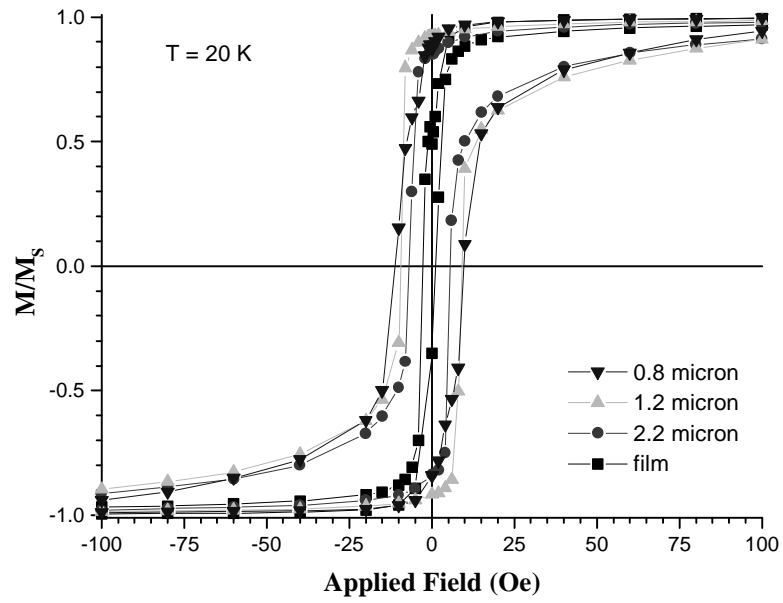


Figure 4.6 - Saturation Magnetization vs. Linewidth for spin-valve multilayer structures, $\text{Cu}(50\text{\AA})/\text{Co}(50\text{\AA})/\text{Cu}(50\text{\AA})/\text{NiFe}(30\text{\AA})/\text{Cu}(20\text{\AA})$ and $[\text{Cu}(50\text{\AA})/\text{Co}(50\text{\AA})/\text{Cu}(50\text{\AA})/\text{NiFe}(30\text{\AA})]_5/\text{Cu}(20\text{\AA})$. Solid lines depict the saturation values of unpatterned films. Note that the volume calculated factors in the total thickness of the magnetic layers.

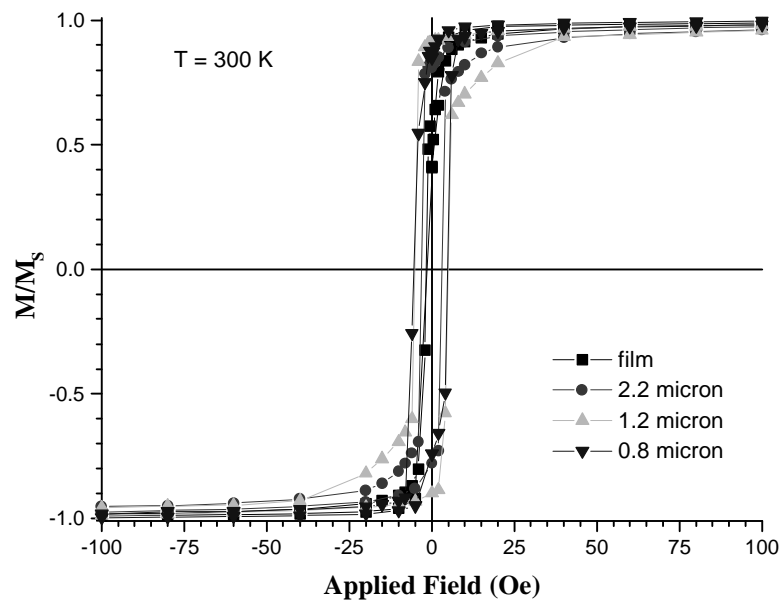
3.1.2 Magnetization properties

From cross-section TEM images, a tapered edge exists in these structures. This profile can be detrimental to magnetic properties where, due to tapering, successive magnetic layers can be physically coupled. In a study of GMR thin films, many have an attributed drop in GMR values due to ‘pin holes’ [Par92]. This concern could not be settled until transport measurements are considered (later sections show the MR to be independent of width). Another concern raised by the imperfect profile is the possibility that the tapering scales with the linewidth, i.e., as width increase, tapering occurs over a smaller fraction of the width. This concern can be easily resolved by tabulating magnetic saturation for various linewidths. From SQUID measurements along with a careful measurement of SQUID sample dimensions, one can calculate the magnetization in terms of emu per cubic centimeter (emu/cc). As an example, a tabulation of widths and lengths of samples along with emu value from SQUID measurements is shown (Tab.4.1).

Tabulations of emu/cc versus linewidths for various samples yield plots like Figure 4.6. The plot is for spin-valve samples of NiFe/Cu/Co/Cu multilayer. The solid lines represent unpatterned thin film values. For a single repeat structure, saturation magnetization values seem to be independent of linewidth. For a repeat multilayer structure, M_s values seem to be slightly dependent on linewidth as saturation value increases for larger linewidths. This dependence suggests that sidewall deposition reduces the deposition rate at greater thicknesses. The significant reduction in M_s value between these single repeat layer and the multilayer can be attributed to degradation of ordering in the case of repeated layers as bilayer quality deteriorates above certain repeats [Pet91].

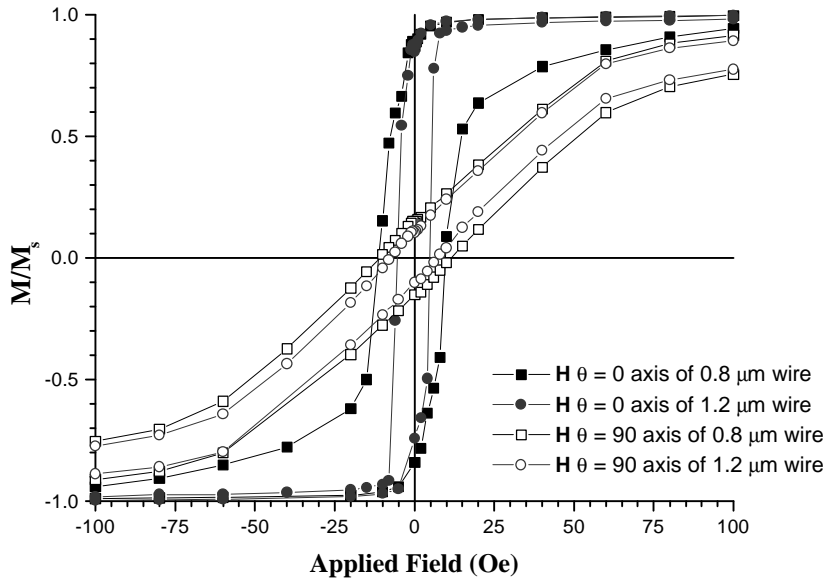


(a)

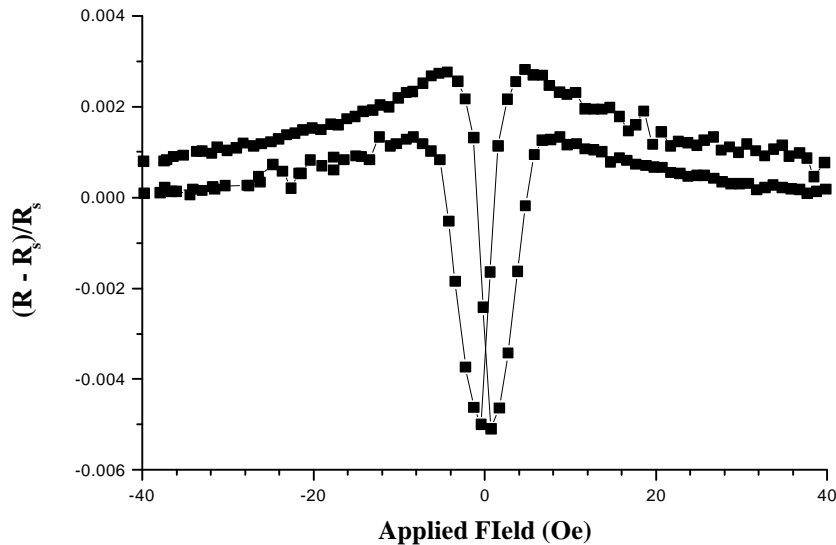


(b)

Figure 4.7 - Hysteresis Loops at 20 K (a) and 300 K (b) with the wire axis parallel to the applied field, easy-axis of NiFe/Ag multilayers.



(a)



(b)

Figure 4.8 - (a) Magnetization curve of NiFe/Ag multilayer showing that the easy axis is defined along the axis of the wire in plane to substrate at $T = 20$ K. Note that the hysteresis loops defined by the solid circle and square points ('easy axis' geometry) the magnetic reversal is much more sudden than hysteresis loops the open circle and square points ('hard axis' geometry) in which cases the magnetic reversal requires greater applied field. (b) MR response of $0.8 \mu\text{m}$ NiFe/Ag multilayer wire.

3.2 NiFe/Ag Multilayers

Ta(50Å)/Ag(28Å)/NiFe(20Å)/[Ag(55Å)/NiFe(20Å)]_{x4}/Ta(20Å) multilayers were deposited (Ni_{0.8}Fe_{0.2} sputter target composition). Magnetization was measured at both 20 K and 300 K with the wires both parallel and perpendicular to applied field (Fig.4.7 and Fig 4.8 (a)). For the wire axis along the axis of H (Fig.4.7), coercivity increased as linewidths decreased for both 20 K and 300 K, although the change at 300 K was not large. At T = 20 K, coercivity increased from 6 Oe for wires of 2.2 μm wide to 11 Oe for widths of 0.8 μm. For unpatterned films, the coercivity was in the order of 1 Oe. Remnant magnetization at both temperatures decreased at smaller widths after initially maximizing at 1.2 μm, M_r/M_s of 0.92 at 20 K and of 0.90 at 300 K. The preferred orientation of magnetization (easy axis) is along the wire. All magnetization measurements along the easy axis show ‘square’ hysteresis loops without a significant ‘shoulder’, consistent with little to no anti-parallel alignment between successive NiFe layers. This lack of anti-parallel alignment is consistent with MR data (Fig.4.8(b)). MR showed no negative magneto-resistance but did show a typical character of longitudinal anisotropic magneto-resistance (AMR). Due to the high length to width ratio of these lines, the dipolar fields may be insufficient to create anti-ferromagnetic coupling, which is necessary for negative magneto-resistance.

3.3 Fe/Co/Cu/Cu Sandwich Structures

The first system studied was Fe(50Å)/Co(50Å)/Cu(50Å)/Co(50Å)/Cu(20Å). This system is a sandwich structure in which ferromagnetic layers (Co) are separated by a relatively thick spacer. At 50 Å spacer thickness, the coupling strength should be at

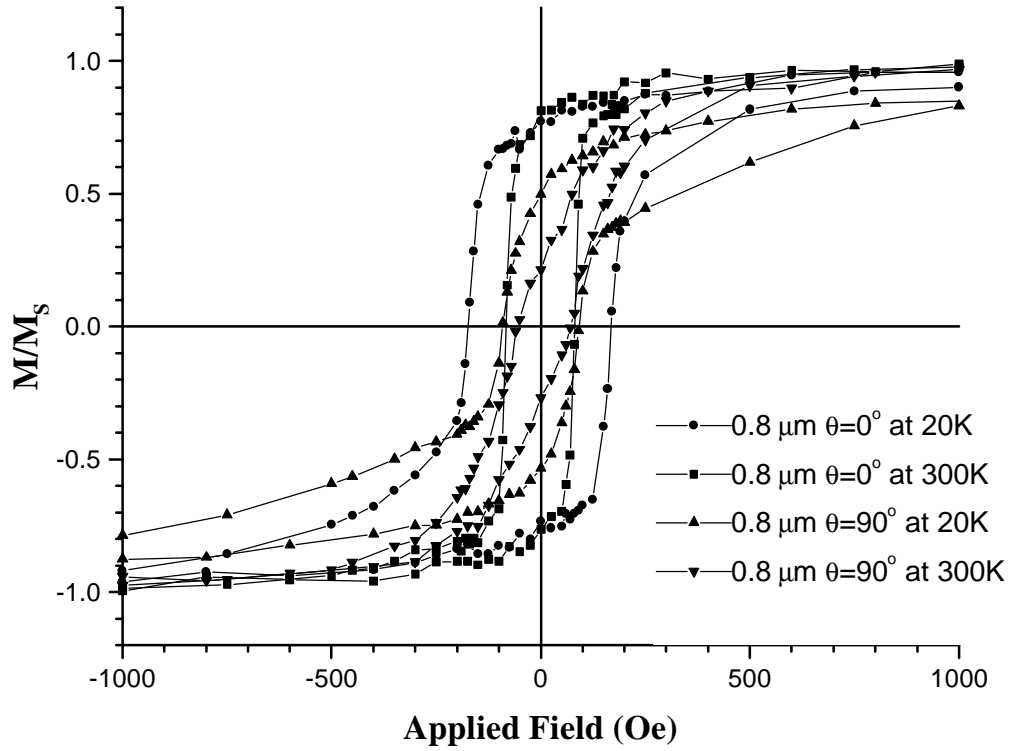


Figure 4.9 - Fe(50Å)/Co(50Å)/Cu(50Å)/Co(50Å)/Cu(20Å) sandwich structure of 0.8 μm wire at the applied field parallel and perpendicular to the axis at 20 K and 300 K.

minimum (Chapter 3) and the anti-parallel alignment may be induced by a difference in the magnetization switching characteristic between the Co layer coupled to the Fe buffer layer and the top Co layer. Again, the measurements were conducted with the applied field along the axis of the wire and perpendicular to the axis of the wire (Fig.4.9). The coercivity and remnant magnetization trends are similar to the NiFe/Ag multilayers. At $T = 20$ K, the coercivity increased with decreased width from 110 Oe (2.2 μm wire) to 170 Oe (0.8 μm wire); the normalized remnant magnetization ranged from 0.75 to 0.93. The shape of the hysteresis loops is less square than for the NiFe/Ag multilayers.

Plotting MR vs. the applied field for various linewidths allows comparisons of the MR value and its shape, which indicates how the magnetic reversal occurs. To compare the shape, MR has been plotted as the normalized MR values for various linewidths. Normalization is legitimate since MR values for various linewidths are rather constant (all around 1%) (Fig.4.10). The shape shows that for narrower widths (Fig.4.11), complete technical saturation is much more difficult. Higher applied fields are needed to completely saturate the wire. The maximum MR value according to GMR theory should indicate the maximum anti-parallel alignment where the greatest scattering would occur.

For the above sandwich sample, values gathered from an MR plot do not agree with coercivity values measured from a SQUID magnetometer (Fig.4.12). This disagreement results from the ferromagnetic Fe buffer layer. Exponential fits for both the MR maximum field vs. linewidth and coercivity vs. linewidth seem to be offset by a constant value of around 130 Oe. It is speculated that the Fe/Co layers' magnetization reversed first (see Chapter 4.4). This mechanism is consistent also with the shape of the

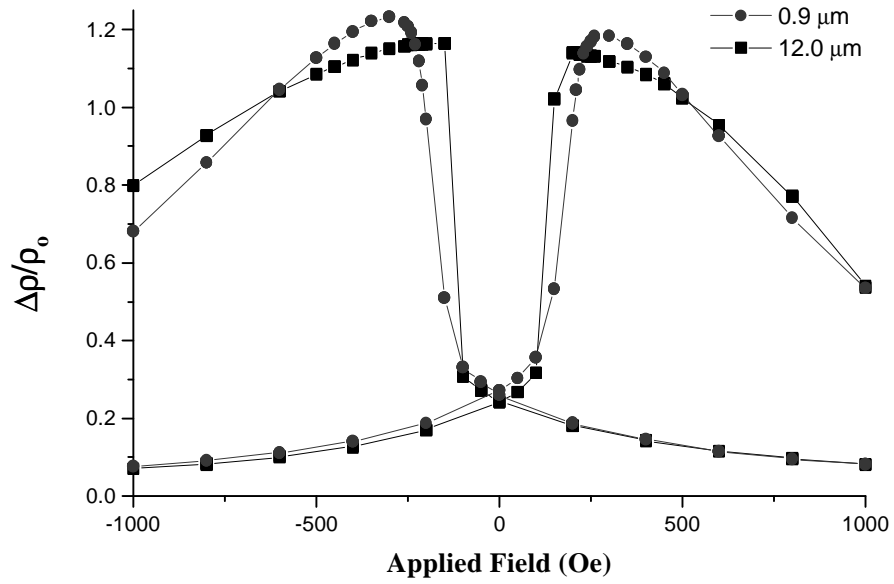


Figure 4.10 - Typical MR vs. Applied Field for Fe(50Å)/Co(50Å)/Cu(50Å)/Co(50Å)/Cu(20Å) sandwich structure for two linewidths. $\Delta\rho/\rho_0 = ((R - R_s)/R_s) \times 100\%$ is defined as MR where R_s is resistance at saturation.

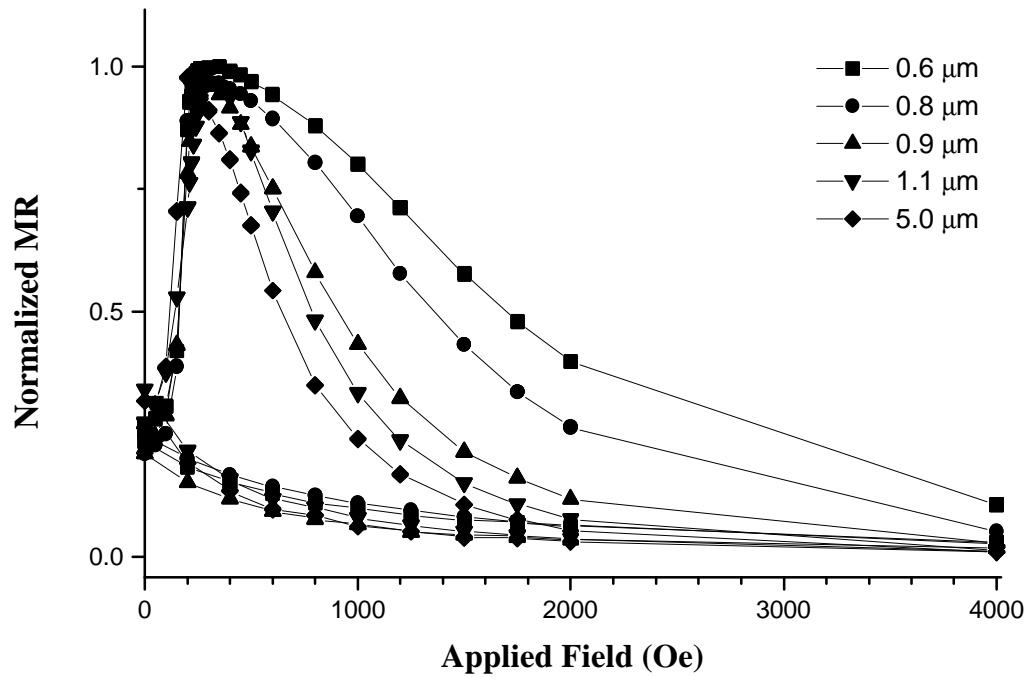


Figure 4.11 - Normalized MR vs. the applied field of Fe(50Å)/Co(50Å)/Cu(50Å)/Co(50Å)/Cu(20Å) sandwich of various linewidths. All samples were cycled at ± 1 Tesla.

MR curve, which is very asymmetrical (more so at smaller widths), signifying that one layer switches much faster than the other. In addition, discrete jumps are not observed in the MR curves. Such discrepancies could be attributed to Barkhausen noise and were not observed. This observation indicates either the domain wall motion is coherent (i.e., there are no significant defect states at which the domain walls can be pinned) or the steady-state PPMS measurement washes out such noise since resistances are taken after the field is set for a few tens of seconds. As mentioned earlier, the MR values are essentially independent of linewidth (Fig.4.13).

3.4 Co/Cu Pseudo-Spin Valve (PSV)

The term pseudo-spin valve describes systems that are essentially a tri-layer, much like a sandwich. For spin valves, anti-parallel alignment of subsequent magnetic layers is accomplished by pinning one layer, usually to an anti-ferromagnet, while one layer is free to rotate with the applied field. Pseudo-spin valve achieves anti-parallel alignment by one layer's thickness differing from the other, which in essence allows one layer to align with the applied field either faster or slower than the other (i.e., difference in coercivities). For the Co/Cu system, the layer structure $\text{Cu}(x_1)/\text{Co}(y_1)/\text{Cu}(x_2)/\text{Co}(y_2)/\text{Cu}(x_3)$, or the repeated units structure $\text{Cu}(x_1)/[\text{Co}(y_1)/\text{Cu}(x_2)/\text{Co}(y_2)/\text{Cu}(x_2)]_n$, can be studied. Cu was employed as the buffer, spacer, and cap layers. Due to the use of only two materials, these structures were deposited by both UHV sputtering and electron-beam evaporation.

The first structure to be considered is the $\text{Cu}(50\text{\AA})/\text{Co}(20\text{\AA})/\text{Cu}(60\text{\AA})/\text{Co}(50\text{\AA})/\text{Cu}(30\text{\AA})$ pseudo-spin valve deposited by electron-beam evaporation at MCNC. The plot of field at maximum MR vs. linewidth and coercivity from SQUID magnetometer measurements shows a significant difference (Fig.4.14 and Fig.4.15) at 10 K. Transport

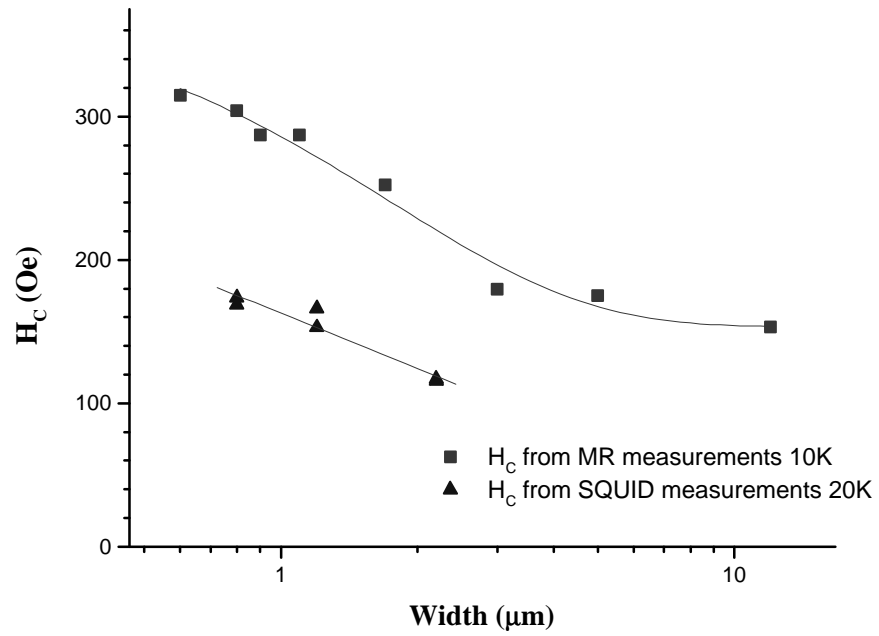


Figure 4.12 - Plot of maximum MR and coercivity measurement from SQUID for Fe(50Å)/Co(50Å)/Cu(50Å)/Co(50Å)/Cu(20Å) sandwich structures of various linewidths.

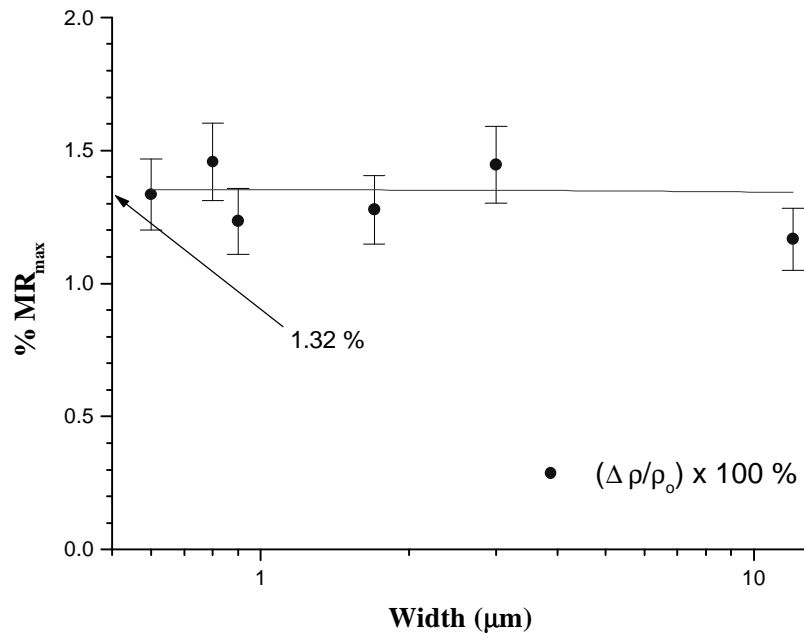


Figure 4.13 - Plot of MR values vs. linewidth for Fe(50Å)/Co(50Å)/Cu(50Å)/Co(50Å)/Cu(20Å) sandwich structures.

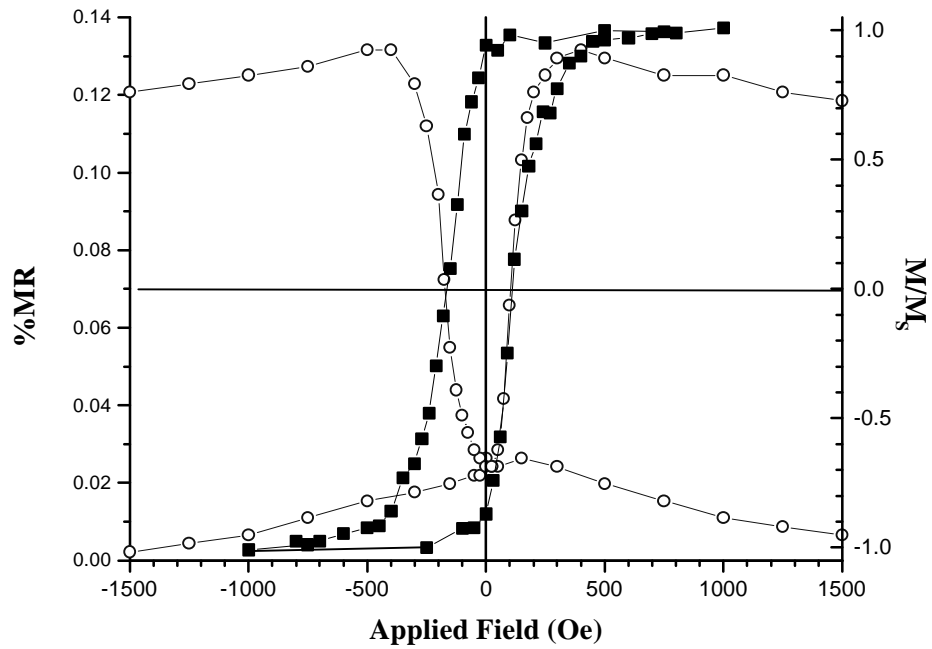


Figure 4.14 - Magnetization measurement of 1.2 μm wide (closed square) and MR measurement of 1.1 μm wide (open circle) at 10 K of Co/Cu PSV.

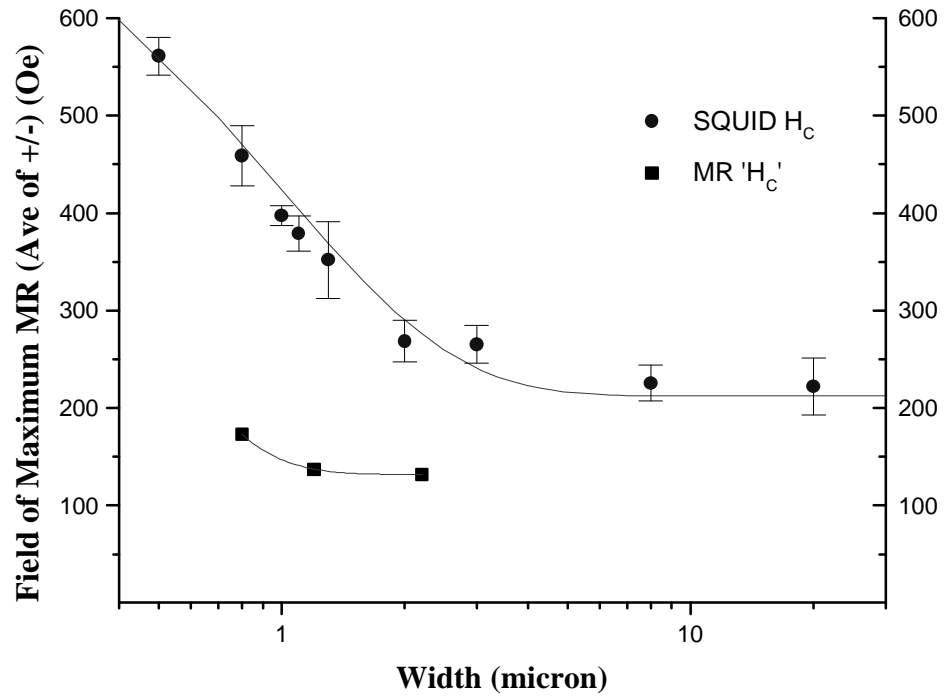


Figure 4.15 - Cu(50Å)/Co(20Å)/Cu(60Å)/Co(50Å)/Cu(30Å) field of maximum MR and coercivity from SQUID magnetometer measurements vs. linewidth.

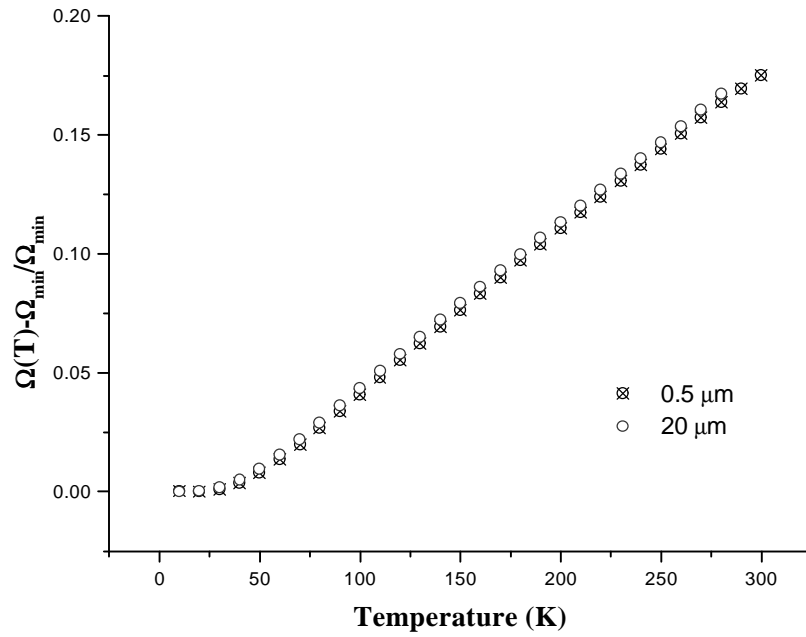


Figure 4.16 - Normalized resistance vs. T for 0.5 μm and 20 μm wire structures of Cu(50Å)/Co(20Å)/Cu(60Å)/Co(50Å)/Cu(30Å) and the difference between two wires.

data as a function of temperature gives insight into these structures (Fig.4.16). If growth is similar for various linewidths (growth through various aperture openings), then the resistivity value extrapolated to 0 Kelvin would be expected to be equal. The normalized R vs. T plot shows good agreement between 0.5 μm and 20 μm linewidths (Fig.4.16). The shape of MR vs. the applied field, like the Fe/Co/Cu sandwich, is asymmetrical, indicating that one layer switches much faster than the other layer.

4. Discussion

The data in Figure 4.16 show that the sputter deposition at low deposition pressures (< 2 mTorr) through sub-micrometer opening and subsequent lift-off have a minimal effect on the quality of the structure especially in terms of transport properties. From various general properties studies of these lift-off structures (thickness and magnetization), up to certain thicknesses (~ 1000 Å) the resulting structures are equivalent, and their properties such as M_s and height are independent of their minimum feature sizes at low pressures (Fig.4.6). Thus, for feature sizes down to 0.5 μm , direct sputter deposition and lift-off are compatible and viable alternative patterning processes.

From the SQUID magnetometer measurements, the patterning indeed creates a preferred direction or 'easy axis' along the length of the wire (Fig.4.8) and that the coercivity and M_r/M_s are a function of the geometry, the width of the sample. Easy axis orientation shows that the shape anisotropy is much larger than any magneto-crystalline anisotropy by the same arguments of Piraux et al [Pir97]. Due to the limited area of the test reticle, there are only SQUID magnetometer samples of four differing widths; thus, it cannot be definitely stated what this dependence is, but similar trends in NiFe/Ag

multilayers and Fe/Co/Cu/Co/Cu sandwiches indicate that geometry has a strong influence. As for the MR measurements, negative magneto-resistances for Co/Cu structures are indeed apparent (Figs.4.10,4.11,4.14). Although other groups have seen negative MR for annealed and patterned NiFe/Ag multilayers [Hyl95], only AMR characteristics were observed. The high length to width ratios prevented dipolar coupling, which is the suggested means by which the NiFe/Ag attains anti-parallel magnetization alignment.

MR plots show interesting characteristics parallel to the SQUID magnetometer measurements. The sharp increase in the applied field at which the maximum MR values occur is observed. These maximum MR values correspond to maximum anti-parallel alignment. Studies of sub-micrometer NiFe and Fe structures by Shearwood et al and Adeyeye et al [She94, Ade97] show similar behavior (Chapter 1). In this study, particularly the Co/Cu sandwich structures, the MR shape was found to be highly asymmetrical (Fig.4.10, 4.11). In the Co/Cu sandwich structure, as the applied field is increased, the resistances for all widths rise quickly. Once the maximum is reached and as the applied field is increased more, the resistance reaches saturation values depending on the widths (Fig 4.11). This behavior seems to be rooted in geometrical effects. The effect cannot be the same as given by Adeyeye et al to describe AMR behavior of their NiFe wires, since such effects should give symmetrical broadening. Observed behavior in this work may be explained by the following.

A model for magnetization reversal based on the MR data is proposed. If indeed the anti-parallel alignment of magnetization is energetically favorable, the asymmetry in the MR response can be explained. The initial reversal process to reach energetically

favorable an anti-parallel case only requires a very low applied field. Due to the geometry (shape anisotropy) of the narrowest width, this anti-parallel dipolar arrangement is more stable and requires much more applied fields to again parallel align both ferromagnetic layers magnetizations. This explanation seems contradictory to the explanation as to why negative MR in the NiFe/Ag multilayers was not observed. This contradiction may be resolved by taking domain wall behavior into account. Due to the requirement of considerable fields to change the magnetization, it may be concluded that the magnetization of the wire structure reverses by creation and growth of domain walls, which have favorable direction. Indeed, if a single domain is expected and present throughout the process, a sharp response to the applied field is expected, since due to shape anisotropy, magnetization not along the axis of the wire is highly unstable (the same argument as to why little to no longitudinal AMR response was seen in Co wires in Jia et al [Jia97]). In the NiFe/Ag case, it may be expected that the multi-domain structure, which may be favorably dipolar-coupled along the same layer as opposed to across the spacer layer. If the wire structures were shorter in length, the edge fields may favorably align the layers. In the Co/Cu sandwich case, one layer is coupled to the Fe magnetic layer; thus, enhancing the one layer to flip faster than the other.

The coercivity from the SQUID magnetometer measurements and the ' H_C ' from MR measurements do not agree. Both Hong et al [Hon95a] and Adeyeye et al [Ade97] assigned coercivity to MR minima in longitudinal AMR measurement for Ni nanowires and again for NiFe and Fe sub-micrometer wires. However, the GMR structures are different. This difference is evident when the definitions of H_C and maximum GMR values are considered. H_C corresponds to when the total magnetization is zero, and maximizing

the GMR values require maximizing the anti-parallel alignment. In the cases of the Co/Cu sandwich and the pseudo spin-valve structures, maximizing the anti-parallel alignment would mean a non-zero total magnetization value, since for the Co/Cu sandwich, one Co layer is coupled to the Fe buffer layer, and for Co/Cu PSV, one Co layer is thicker than the other. On the other hand, the observed minima in the NiFe/Ag MR responses correspond closely to the H_C value from the SQUID magnetization measurements.

From the following arguments, it can be known which ferromagnetic layer switches first. For simplicity, consider the PSV case and denote $\uparrow\uparrow\uparrow\uparrow$ as 50 Å of Co and $\uparrow\uparrow$ as 30 Å of Co. At the start, the structure is saturated: $\uparrow\uparrow\uparrow\uparrow \uparrow\uparrow$, and at the end, again saturated: $\downarrow\downarrow\downarrow\downarrow \downarrow\downarrow$. Somewhere in between, there are two choices that would allow maximum MR: a) $\uparrow\uparrow\uparrow\uparrow \downarrow\downarrow$ or b) $\downarrow\downarrow\downarrow\downarrow \uparrow\uparrow$. For magnetization to be zero, two choices are: a) $\uparrow\uparrow\uparrow\uparrow(\frac{1}{2})\downarrow \downarrow\downarrow$ or b) $\downarrow\downarrow\downarrow\downarrow(\frac{1}{2})\uparrow \uparrow\uparrow$. For case a), the field at which magnetization is zero occurs after the field is at maximum MR (i.e., sequence of 1) $\uparrow\uparrow\uparrow\uparrow \uparrow\uparrow$ 2) $\uparrow\uparrow\uparrow\uparrow \downarrow\downarrow$ 3) $\uparrow\uparrow\uparrow\uparrow(\frac{1}{2})\downarrow \downarrow\downarrow$ 4) $\downarrow\downarrow\downarrow\downarrow \downarrow\downarrow$). For case b), it is vice-versa and it is what has been observed. In case b), the thicker layer reverses magnetization before the other. This logical progression can be applied to show then that the Fe/Co layers switches first in the Fe/Co/Cu/Co sandwich structures, also.

CHAPTER 5 MAGNETIC NANOWIRE FABRICATION AND CHARACTERIZATION

1. Overview

The initial excitement for starting the study of magnetic systems is from a simplified argument: an increase in MR in the GMR structures could be observed. The argument is as follows. In Chapter 1, it was pointed out that the GMR in CIP (Current in Plane) depends on the carrier electron being able to ‘see’ at least two successive magnetic layers before scattering, i.e., the electron must remember the spin orientation between two magnetic layers (MFP must be larger than layer thicknesses). The characteristic length for this phenomenon is essentially the electron mean free path, which is in the order of 100 Å for metallic materials [Kit86]. One would see a drop in the MR for GMR systems if the layer thicknesses are increased although the overall resistance is lower [Die94]. In the thin film plane geometry, there have been several studies and solutions to enhance this scattering. The seminal work by S.S.P. Parkin shows an increase in MR by the addition of Co at the NiFe/Cu interface [Par92a, Par93]. In this simplified view of transport, scattering in the plane has been neglected. One could expect electrons travelling along the plane to travel its mean free path, which would scatter it to another direction. Such paths would not contribute to the GMR effect. Now, imagine the in-plane dimensions to be comparable to the electron mean free path and imagine the wall boundary to scatter electrons coherently and reflect perfectly such that its spin is unaffected. This scenario

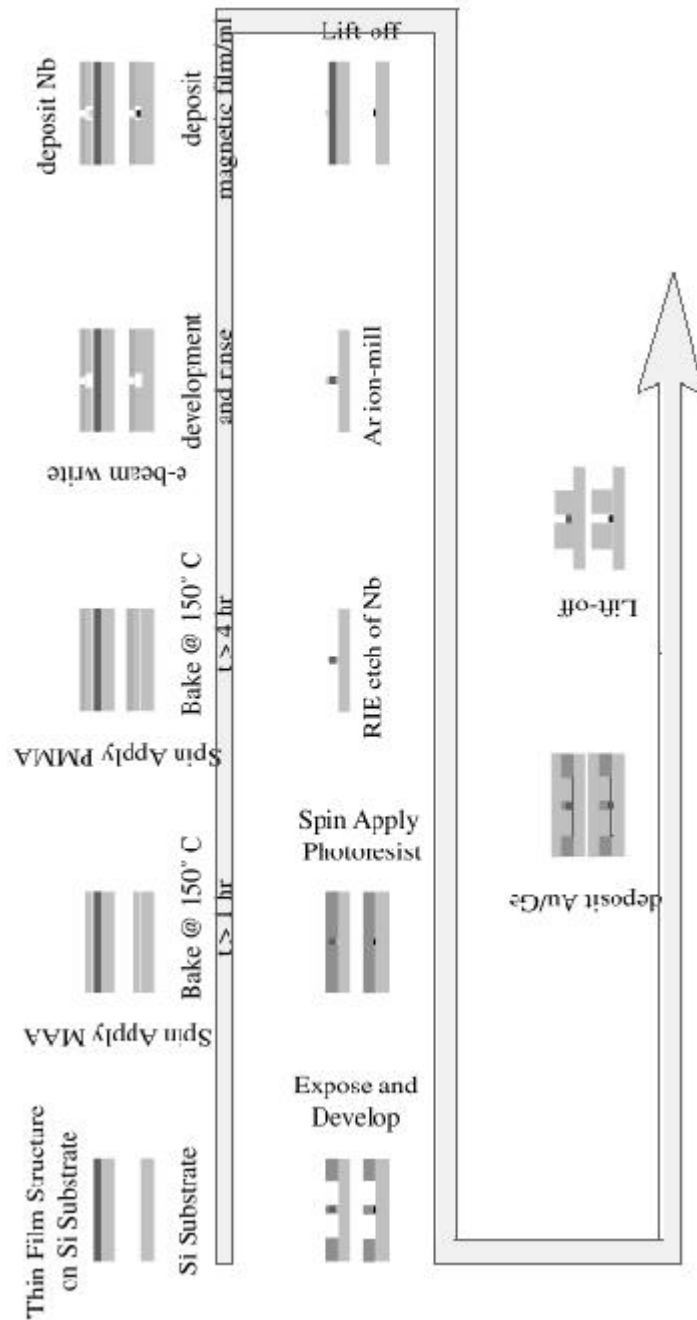


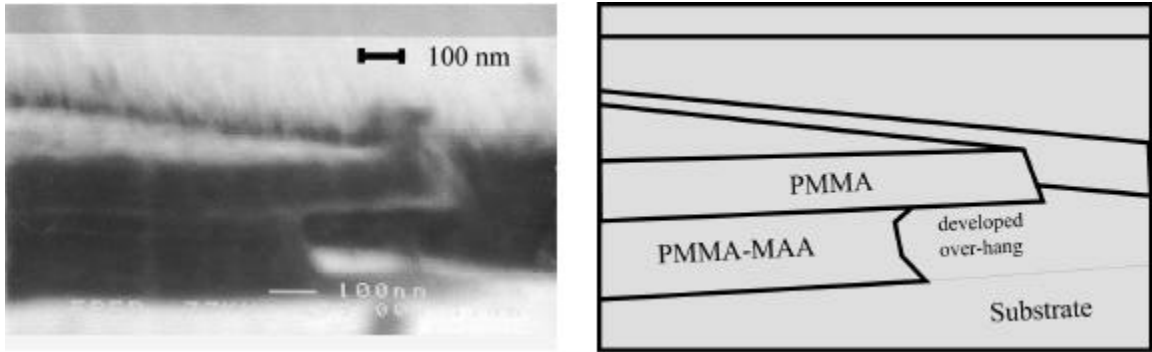
Figure 5.1 - Schematic and summary of processing steps in fabricating nanowire structures.

would, in essence, favor the vast majority of all scattering events contributing to GMR. Such an argument has been utilized to explain why the GMR in the CPP (Current Perpendicular to Plane) geometry is much bigger than the GMR in CIP geometry [Bas98]. In the CPP geometry, the carriers travel perpendicular to the film plane; thus, the electrons 'see' successive magnetic layers. It is hoped that a successful patterning process would yield structures with sidewalls that will coherently reflect the electrons so that all scattering processes will contribute to the GMR.

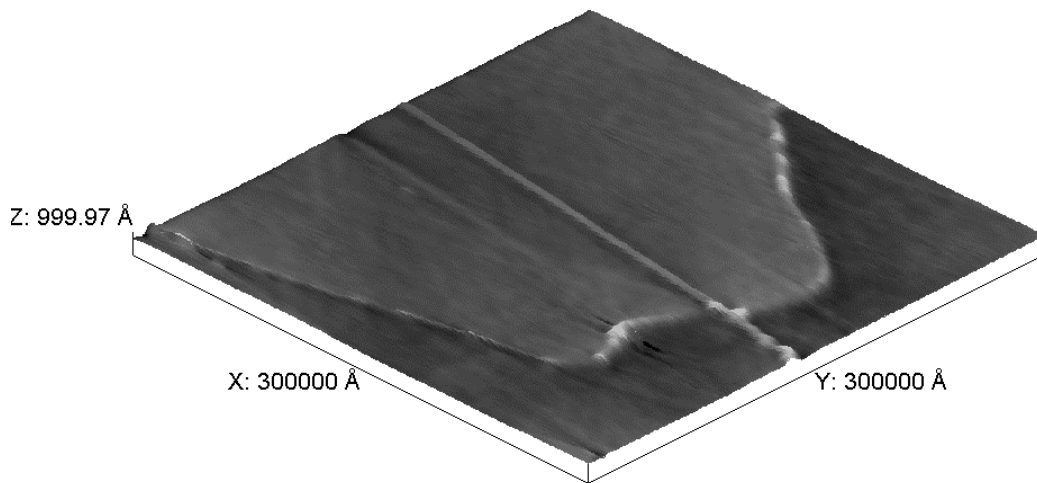
2. Fabrication Schemes

The general scheme for electron-beam lithography has been described in Chapter 2.1.2.2. The focus of this study has been diverged to improving fabrication techniques due to difficulties encountered in fabricating the samples. Various schemes to be described later can be best described by Figure 5.1. The first attempts to fabricate and study magnetic nanowires were very much like fabrication processes involved in patterning sub-micrometer spin-valve wire structures where direct sputter deposition and lift-off were used. The second attempts incorporated the use of evaporation, both thermal and electron-beam. The most successful scheme involved an etching process versus lift-off for patterning.

In all fabrication schemes, the bi-layer mask structure was fabricated using PMMA/ PMMA-MAA resist layers shown in Figure 5.2. The desired patterns were written at line dosages ranging from 0.8 nC/cm to 1.4 nC/cm. These dosages usually result in wire widths ranging from 30 nm to 90 nm. The resulting pattern (Fig 2.4) was characterized by AC transport measurements described in Chapter 2.2.3. The SEM



(a)



(b)

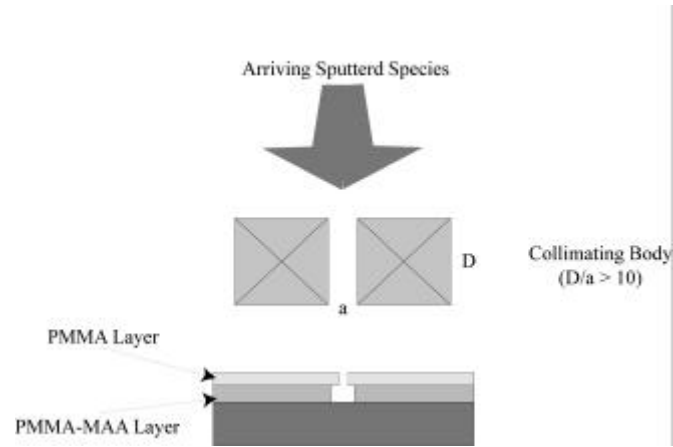
Figure 5.2 - (a) SEM micrograph (left) and illustration (right) of the overhang bi-layer resist structure of PMMA/PMMA-MAA. (b) $30\ \mu\text{m} \times 30\ \mu\text{m}$ AFM micrograph of the Au/Ge leads, patterned by photolithography and lift-off, to nanowire structure leads.

micrograph and the schematic of the overhang structure and the AFM micrograph of the Au/Ge lead (patterned by photolithography) are shown in Figure 2.2 (a) and (b).

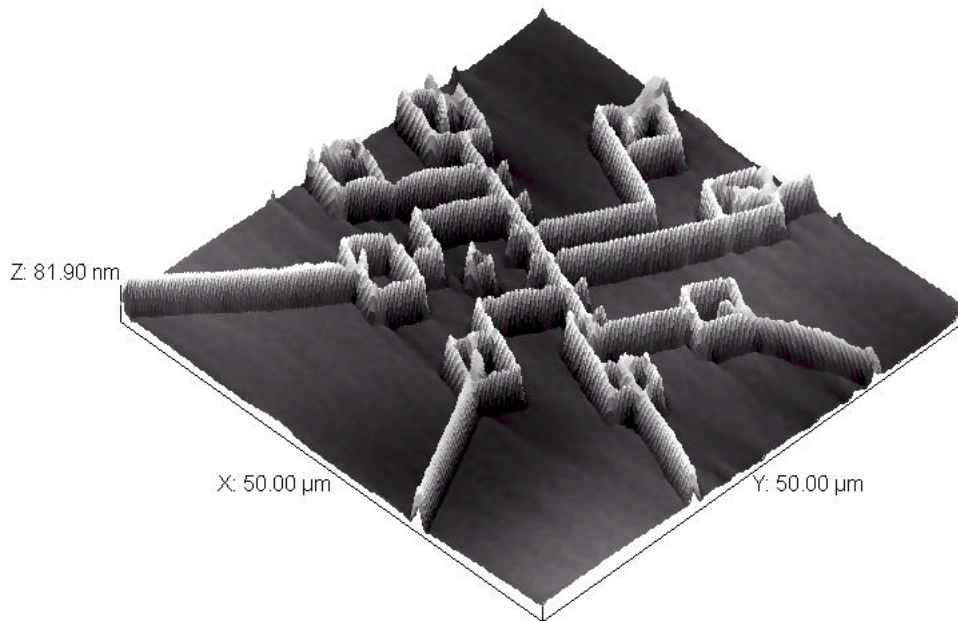
For all schemes requiring sputtering through the developed bi-level mask structure, a physical chimney was placed in front of the sample to collimate and minimize deposition on the sidewalls (Fig.5.3 (a)). With collimation, the deposition rates were reduced by ~17%. Typical deposition rates were as follows: 0.15 Å/s for Co (75 WDC); 0.32 Å/s for Cu (75 WDC); 0.16 Å/s for Nb (75WDC) and 0.12 Å/s for Fe (75WRF), all at 1 mTorr. For comparison purposes, Ni was deposited and studied. Thermal evaporation and electron-beam evaporation of Ni is described in Chapter 2. Thin film Ni samples (500 Å thickness) were prepared by sputtering with a deposition rate of 1.05 Å/s at 50 WDC and 2 mTorr. These Ni films were patterned by a deposition of Nb (500 Å thickness) used as an etch mask. Ar ion-milling was used to remove Ni and RIE was used to remove the remaining Nb (see Chapter 2.1.2.3).

3. Physical Properties of Resulting Nanowires

The first attempts were to directly sputter deposit through the bi-level resist via the collimating body. The resulting structures are shown in Figure 5.3 (b) and Figure 5.4 (a) and (b). SEM micrographs (Fig.5.4) show a 80 nm wide, 30 nm thick Cu test structure. The sidewall profile, observed at an angle and higher magnification (Fig.5.4(b)), is found to be smooth and nearly vertical as seen from the test pattern circle which underwent the same preparation steps as the wire test structure. The sidewall profile indicates that the

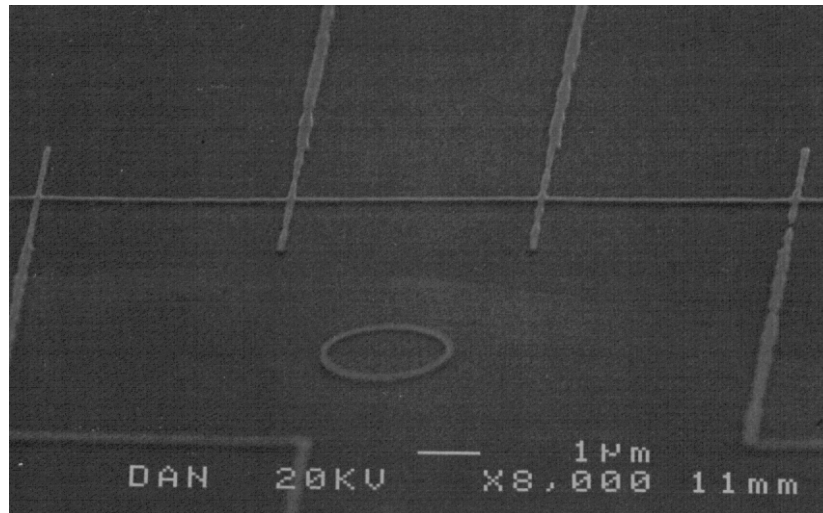


(a)

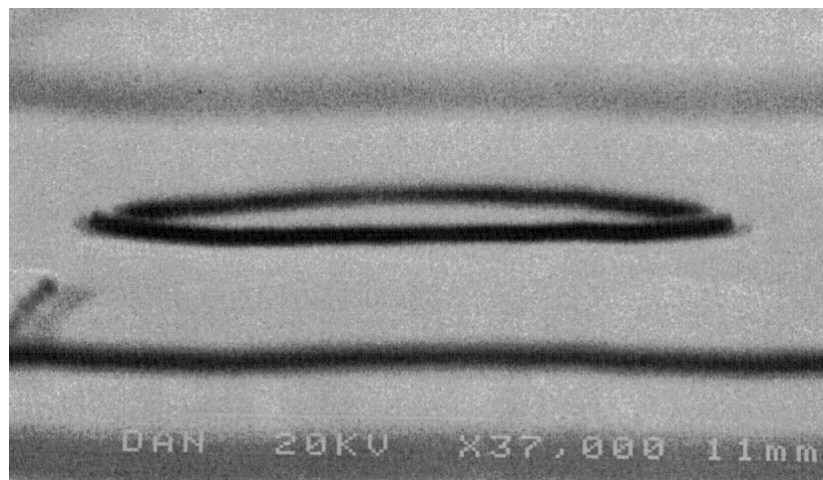


(b)

Figure 5.3 - (a) Schematic of the collimating body and the bilevel resist to a sputter deposit nanowire structure, which results in structures seen in (b) a $50\ \mu\text{m} \times 50\ \mu\text{m}$ AFM scan of a $\text{Fe}(50\text{\AA})/[\text{Co}(15\text{\AA})/\text{Cu}(20\text{\AA})]_{\times 10}/\text{Cu}(30\text{\AA})$ wire structure with integrated leads for transport measurements.



(a)



(b)

Figure 5.4 - (a) a SEM micrograph of 80 nm wide, 30 nm thick Cu wire structures. (b) a SEM micrograph of the same structure as in (a) showing sidewall profiles of a circular test pattern.

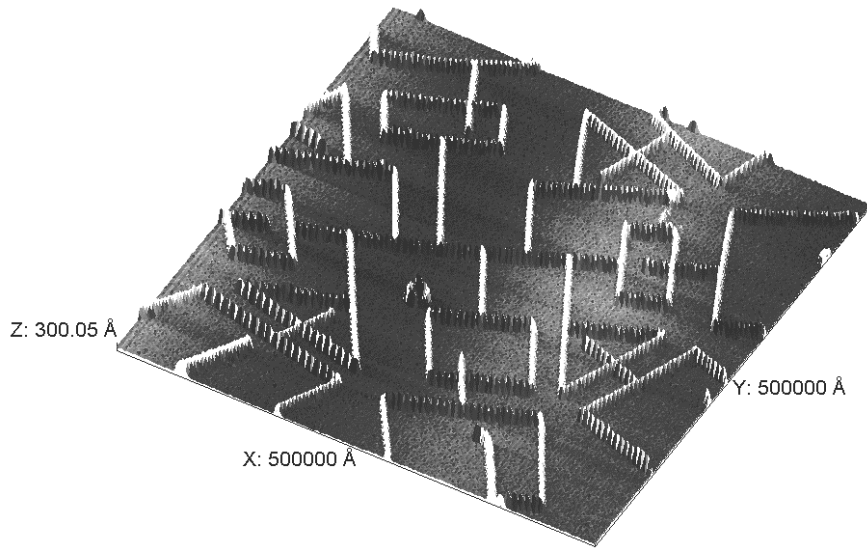
arriving sputtered species were adequately collimated and there was minimal interaction between the deposited wire and the resist due to the overhang bi-level resist structure.

Thermal evaporation and electron-beam evaporation of Ni show markedly different characteristics. AFM micrographs for the evaporated Ni nanowires are shown in Figures 5.5 (a) and (b). These nanowires do not display smooth sidewall profiles as seen in Figure 5.3 (b) for the sputter-deposited nanowire. The evaporated nanowires appear as a “string of pearls.” Such a structure may be postulated due to the fact that arriving atoms in the evaporation case do not possess as much energy as the sputtered atoms. Arriving species of higher energy would be more likely to diffuse on the surface (thus layer by layer growth) instead of coalescing into island like shapes. Whether these islands physically touch will become more evident in the transport measurements to be reported later.

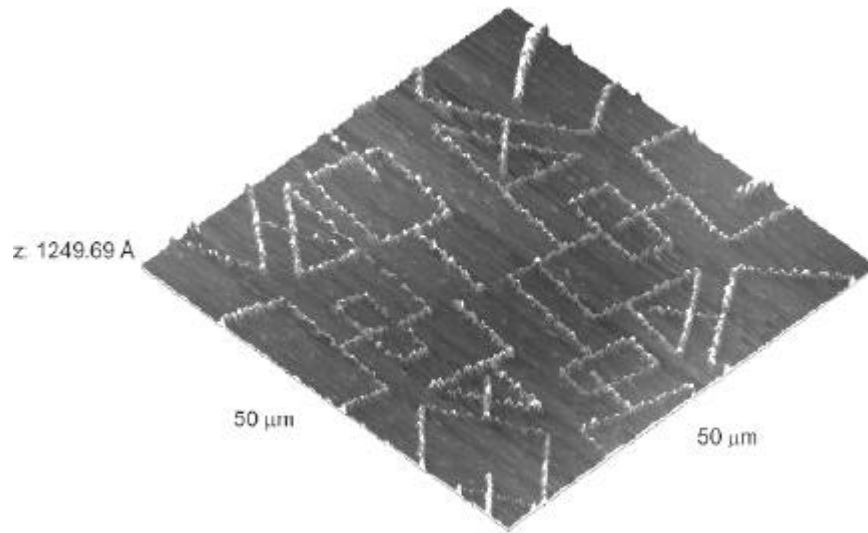
In addition to the AFM images and the SEM images, a cross-section TEM was performed on Ni nanowires fabricated by the Ar ion-milling. The resulting micrographs are shown in Figure 5.6. The Ni nanowire of approximately 75 nm in width sits on a mesa created by over etching of Si substrate by $\sim 200 \text{ \AA}$. The remaining height of the Ni nanowire is approximately 500 \AA , equivalent to the original thickness of the thin film. This thickness is a good indication that RIE etch essentially removed all of Nb without etching Ni. The shape of the wire, especially the sidewall slope, either indicates that the Nb mask layer did not have a sharp profile or that re-deposition during etching occurred.

4. Transport Properties of Nanowires

Again, the sizes of these structures are too small for SQUID magnetization measurements. Transport measurements were conducted for various nanowires. The first

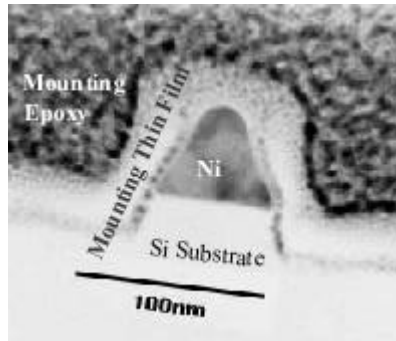


(a)

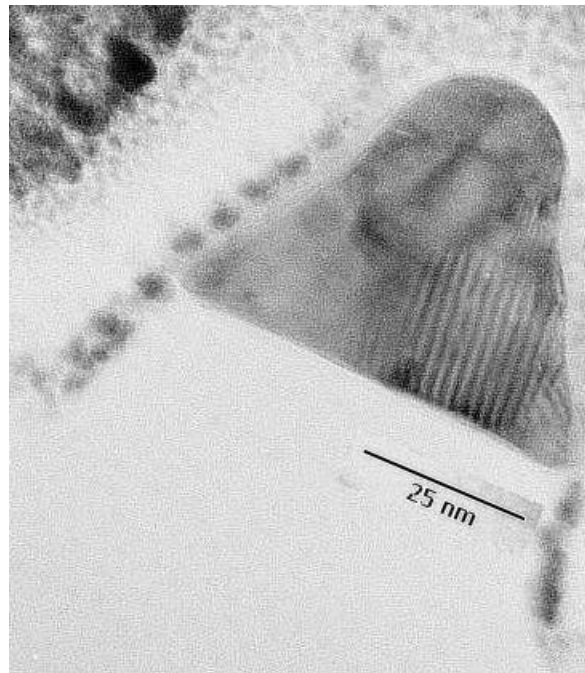


(b)

Figure 5.5 - (a) $50\ \mu\text{m} \times 50\ \mu\text{m}$ AFM micrograph of an Ni nanowire fabricated by thermal evaporation and by lift-off. (b) Ni nanowire fabricated by electron-beam evaporation and by lift-off.

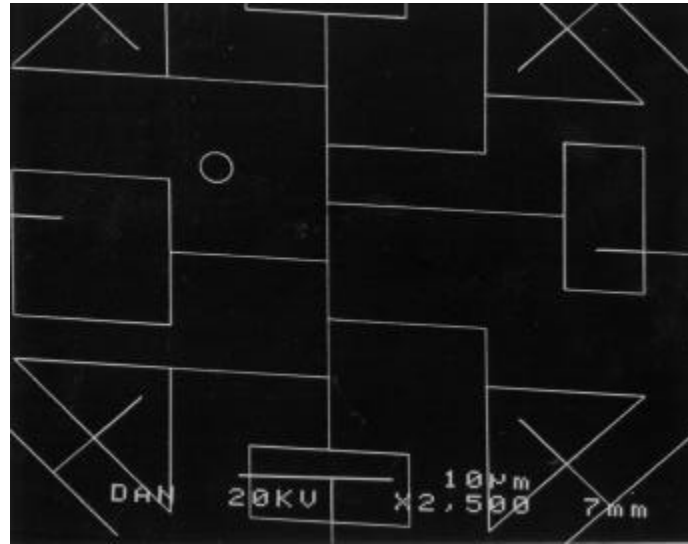


(a)

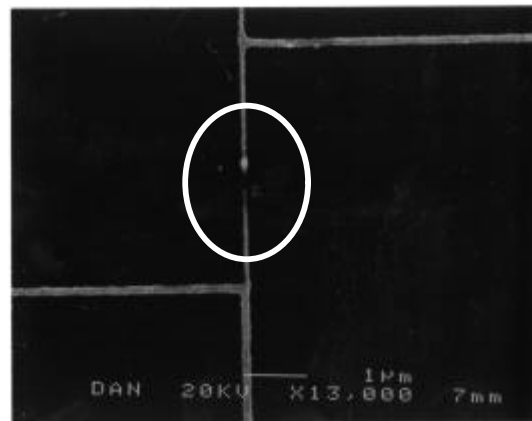


(b)

Figure 5.6 - Cross-section TEM micrograph of an Ni nanowire patterned by ion-milling using Nb as an etch mask. (a) Image shows the width is 75 nm and height is 50 nm. The original thickness of the Ni film. (b) Image is a magnification of (a). TEM courtesy of D. Temple, MCNC.



(a)



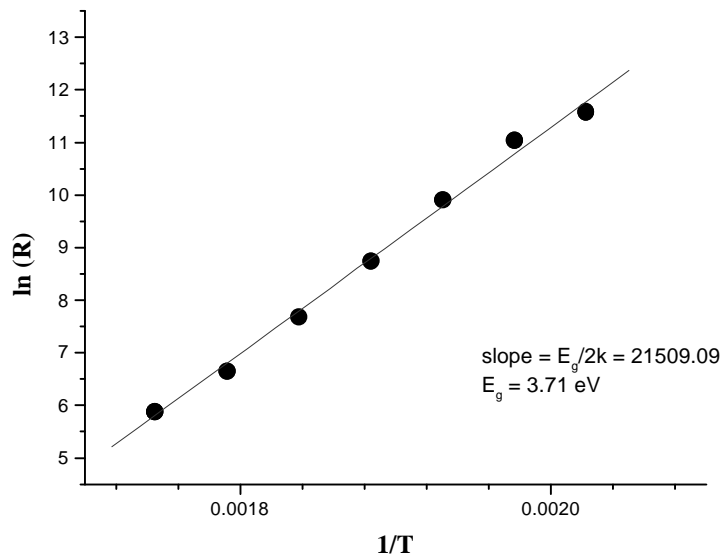
(b)

Figure 5.7 - (a) SEM micrograph of the nanowire structure with integrated leads for transport measurements. (b) SEM micrograph demonstrates the effects of high current densities on nanowire.

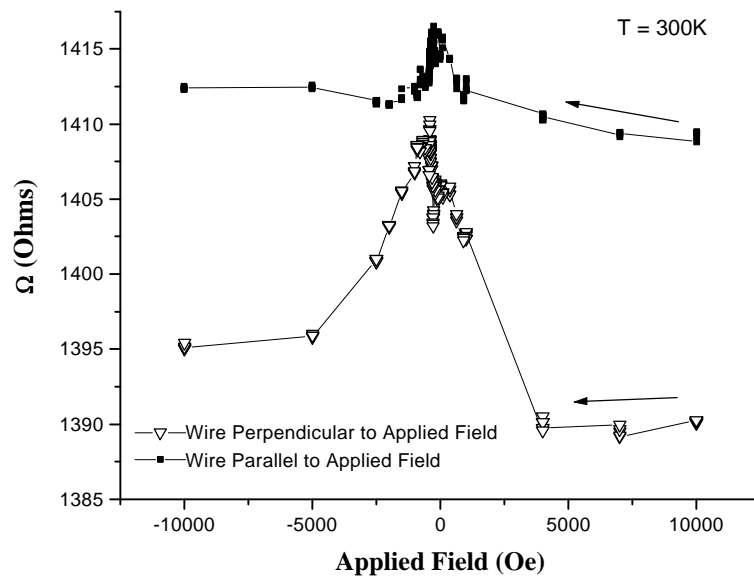
nanowire considered was a Fe nanowire fabricated by sputtering through bi-level resist and lift-off. Room temperature resistivity was found to be roughly 30 times than the bulk Fe, indicating a disordered structure with a high impurity and/or defect concentration. As expected from such high room temperature resistivities, the wire resistance was nearly temperature-independent from 300 K to 5 K. The high resistance of these nanowires prevented further studies. The highly disordered structure may stem from sputter deposition (see discussion at the end of this Chapter).

Evaporated Ni nanowires had better resistivities at room temperature. For thermally evaporated Ni nanowires, resistance vs. temperature scan was unsuccessful because the wire became 'open' at approximately 220 K (Fig.5.8(a)). This behavior may suggest that the Si substrate was probed instead of the nanowire, but the MR response showed a distinct difference in resistances when the injected current was parallel and perpendicular to the applied field (Fig.5.8(b)). This temperature behavior suggests that the nanowire is not continuous as-deposited (see AFM image Fig.5.5(a)). The possibility of actual damage to the nanowire during the temperature scan can be ruled out since the MR response was taken after the temperature sweep. A more feasible mechanism will be presented later.

The electron-beam evaporated nanowire showed a metallic behavior in that the nanowire resistance decreased with a decrease in temperature (Fig 5.9 (a)). The residual resistance of the nanowire is 0.748 of 300 K value (resistivity ratio of 1.337) while the residual resistance of thin film deposited under the same conditions is .4599 of 300 K value (resistivity ratio of 2.174). Along with better resistance vs. temperature results than a thermally evaporated sample, the MR responses were better defined. The MR response

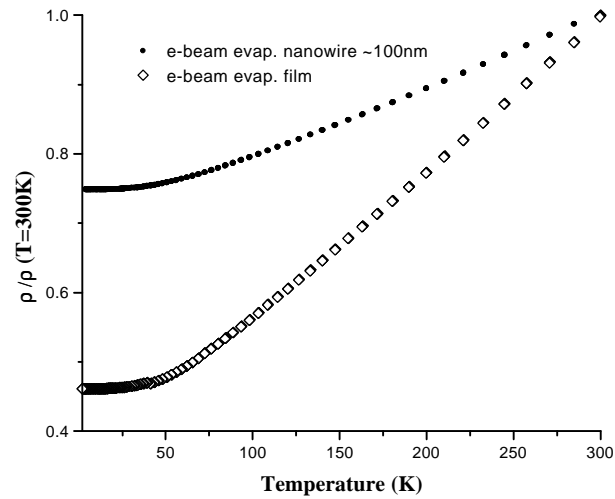


(a)

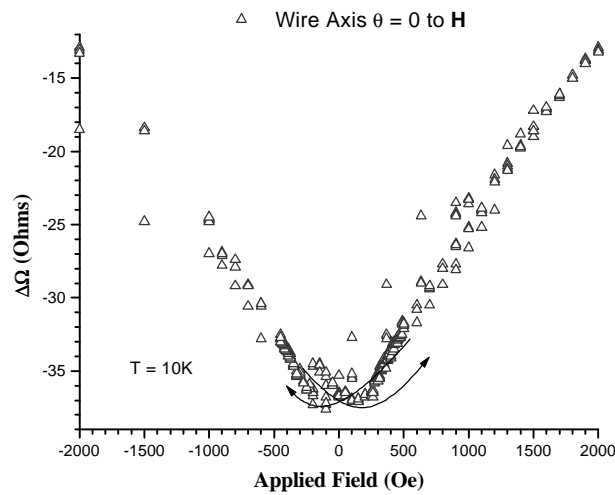


(b)

Figure 5.8 - Ni nanowire fabricated by thermal evaporation and lift-off. (a) Log (Resistance) vs. $1/\text{Temperature}$. (b) Resistance vs. Applied Field for nanowire axis as parallel (closed square) and perpendicular (open down triangle) to the applied field.

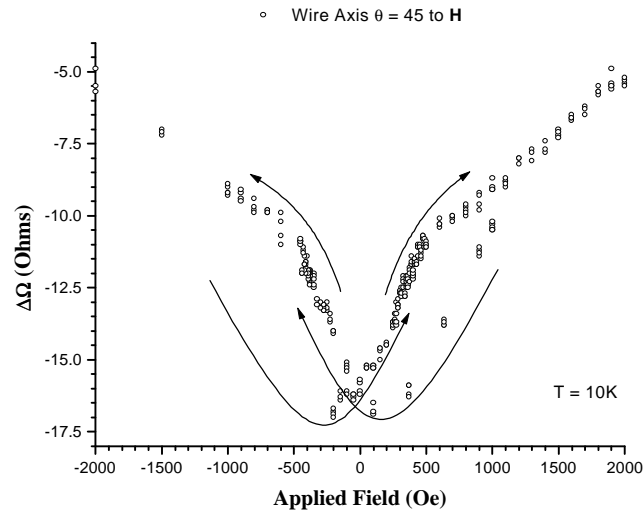


(a)

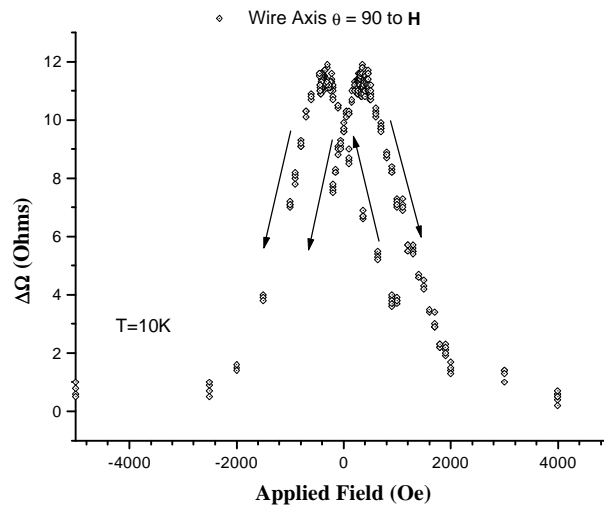


(b)

Figure 5.9 - Ni nanowire fabricated by electron-beam evaporation and lift-off. (a) Normalized Resistance vs. Temperature of nanowire (closed circle) and thin film (open diamond). (b), (c), (d) MR response of nanowire at 10 K for 0° , 45° , and 90° between nanowire axes and applied magnetic field. Continued on next page.



(c)



(d)

Figure 5.9 - Ni nanowire fabricated by electron-beam evaporation and lift-off. (a) Normalized Resistance vs. Temperature of nanowire (closed circle) and thin film (open diamond). (b), (c), (d) MR response of nanowire at 10 K for 0° , 45° , and 90° between nanowire axes and applied magnetic field.

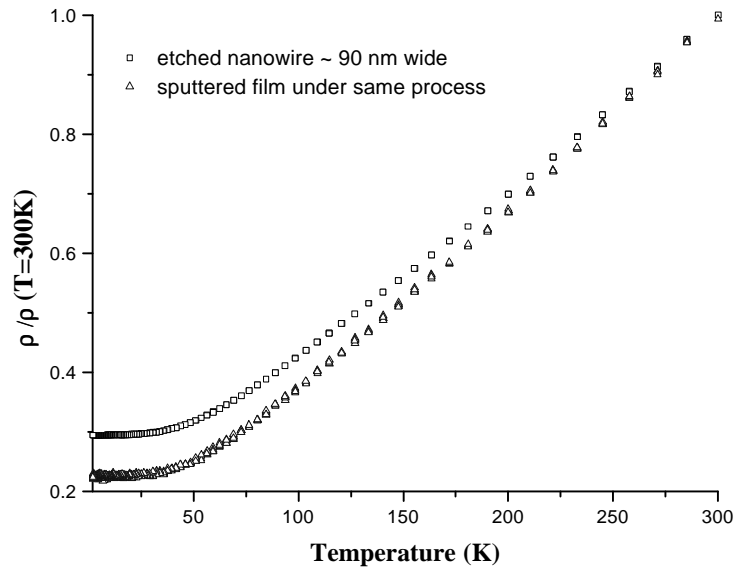
at 10 K for a nanowire axis 0° , 45° , and 90° to the applied field is plotted in Figures 5.9 (b,c,d). The Figures 5.9 (b,c) show ± 2000 Oe sweep to detail features.

For the nanowires fabricated from sputter-deposited thin film by etching using Nb as an etch mask, the resistance vs. temperature is plotted in Figure 5.10 (a). Like the electron-beam evaporated nanowire, this behavior is metallic with a residual resistance 0.2981 of resistance at 300 K (resistance ratio of 3.5593) while compared to sputtered Ni thin film with a residual resistance of 0.2242 of resistance at 300 K (resistance ratio of 4.4603). The resistance ratio of the etched nanowire compared to electron-beam nanowire of similar width is improved by almost a factor of three while the thin film (between electron-beam evaporation and sputter-deposited) is improved only by a factor of two. The MR response is also well-defined at 10 K with an AMR value of approximately 1 % (Fig.5.10 (b)).

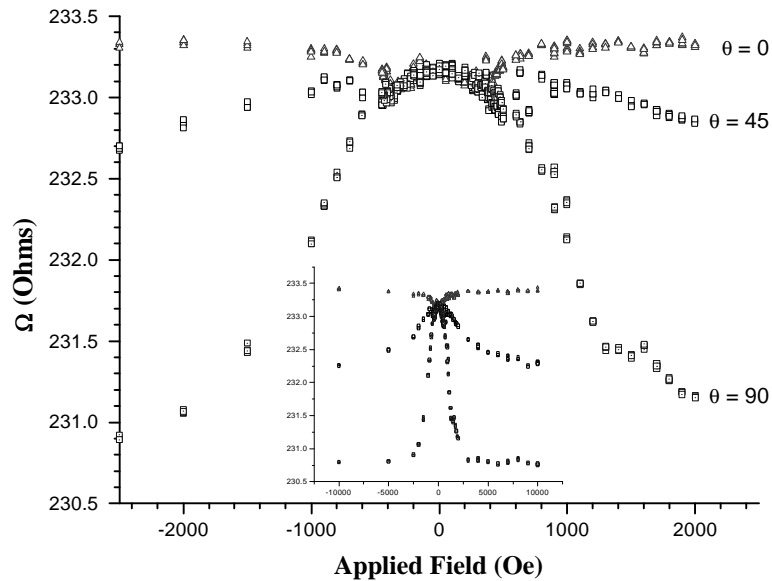
For the etched nanowire, the MR responses as a function of angle are plotted in Figure 5.11(a). The angles 0° and 90° signify the nanowire axis parallel and perpendicular to \mathbf{H} , which was held to 1 Tesla. Angular sweeps were performed at various angles for temperatures from 2 K to 300 K. As shown in Figure 5.11(b), MR ratios for 75 and 90 nm wide nanowire, along with the thin film, exhibit a broad maximum between 150 K and 250 K with a lower response above and below this temperature range. The maximum MR for unpatterned film occurs at ~ 125 K.

5. Discussion

In summary, the experimental results show that direct sputter deposition and lift-off results in smooth sidewalled wires. Direct evaporation and lift-off results in wires that

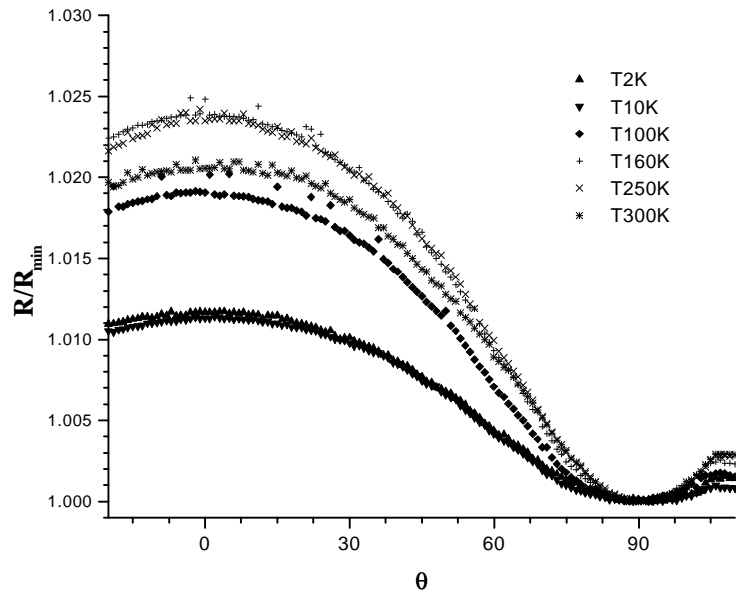


(a)

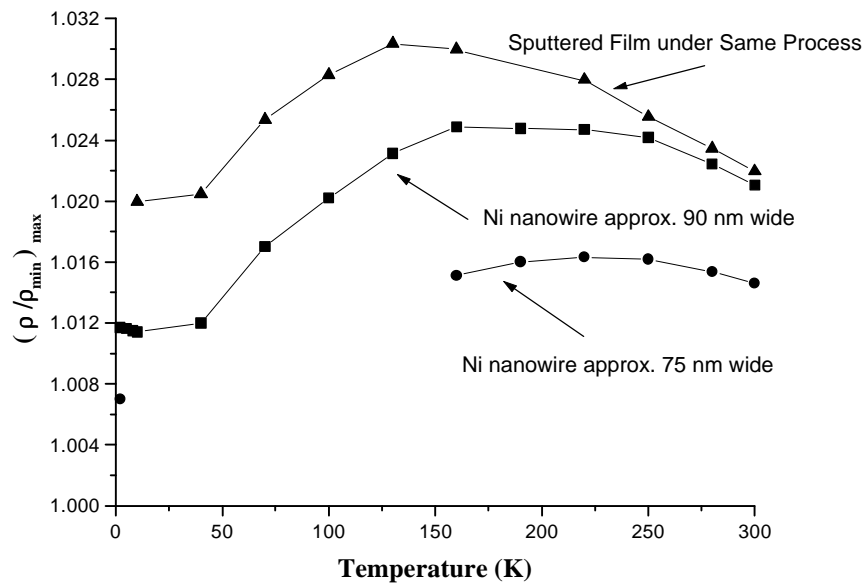


(b)

Figure 5.10 - Ni nanowire fabricated by ion-milling from sputter-deposited Ni thin film using Nb as an etch mask. (a) Normalized Resistance vs. Temperature for nanowire and thin film. (b) MR response at 10 K to applied field for 0° , 45° , and 90° orientations.



(a)



(b)

Figure 5.11 - (a) MR response of Ni nanowire fabricated by Ar ion-milling of 90 nm width as a function of wire orientation in respect to 1 Tesla applied field at various temperatures. (b) Maximum MR ratio for each temperature for various structures.

have rough sidewalls and are possibly discontinuous. Neither resulted in good transport properties. Reasons for such behavior will be postulated below along with a discussion of Ni nanowires fabricated by Ar ion-milling. Such nanowires showed good transport properties such as low residual resistances and MR responses.

Physically, it has been demonstrated that fabrication of a wire as small as 50 nm is possible. Wires were grown by thermal and electron-beam evaporation and sputter deposition through bi-level masks. These masks were the result of electron-beam lithography. The resulting overhang structure due to difference in sensitivities of the two resist layers minimized interaction between the wire structure and the resist, allowing lift-off. The nanowires were also fabricated by using this process to define an etch mask, Nb, which was selectively removed by RIE from sputter-deposited Ni thin film. Although all nanowires under SEM and AFM examinations showed well-defined physical structures, transport measurements reveal properties that are much more complicated. This was especially true for wires grown by deposition through nanometer-sized openings. Direct sputter deposition with lift-off processing showed great promise when studied under SEM and AFM with smooth sidewall profiles and continuous structures. Yet, transport measurements revealed the structure to be highly disordered, as evidenced by resistance vs. temperature data. The data revealed a non-metallic behavior, resistance being independent of temperature. Although considerable care was exercised to produce structurally sound nanowires (i.e., use of a collimating body in efforts to minimize premature closing of the resist opening), direct sputter deposition and lift-off to fabricate these nanowires did not result in metallic samples which were suitable for transport characterizations.

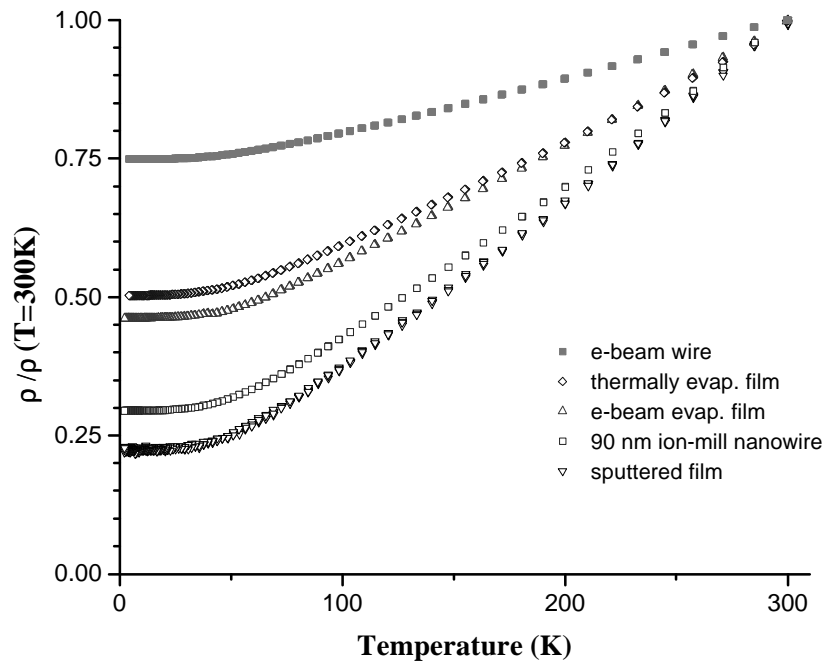


Figure 5.12 - Normalized resistance vs. temperature plot for various Ni structures of 500Å thickness.

Resistance vs. temperature measurement by far is the most important means of determining the quality of the resulting nanowires (Fig.5.12) as defined by residual resistance and resistivity ratio. The resulting nanowire was compared to the unpatterned thin film by plotting the normalized resistance as a function of temperature. A large drop in resistance with decreasing temperature indicates metallic response. At low temperatures, impurity scattering and other scattering mechanisms (such as lattice itself) dominates and eliminates the dependence of resistance on temperature. By comparing the fraction of resistance at low temperatures to that at room temperature, the quality of the nanowires can be compared (Fig.5.12).

Although total resistances of these structures were an order of magnitude higher than nanowires fabricated from ion-milling, they did display AMR. For the electron-beam evaporated nanowires, AMR characteristics were well-defined in the longitudinal and transverse orientations, along with a metallic R vs. T behavior. From AFM studies, the evaporated nanowires were found to be a discontinuous (thermally evaporated) to continuous collection of mound like structures (electron-beam evaporated). This result can be attributed to the fact that arriving evaporated species possess lower energies than sputtered species (especially after collimation, which selectively passes adatoms that have been scattered the least). If arriving adatoms possess low energies, islands of coalescing adatoms are not expected to be able to diffuse along the surface to create layer by layer growth. Although for unpatterned film growth, elevated temperature substrate conditions are the norm, the use of PMMA resist layers, which have a glass transition temperature of approximately 150°C, limits alteration of the substrate condition. For the thermally

evaporated nanowires, R vs. T behavior indicated that the conduction mechanism at room temperature was due to electrons with significant energy crossing discontinuities. From the $\ln(R)$ vs. $1/T$ plot (Fig.5.8(a)) and the intrinsic model of resistance for a semiconductor ($R = R_0 \exp(E_g/2k)$), E_g is found to be 3.71 eV suggesting that current may have shunted through short a gap by the SiO_2 substrate. In addition, at room temperature, there is a weak AMR response, indicating that current was injected into Ni.

As stated previously, residual resistance can be used to compare the quality of the resulting structures. Electron-beam deposited Ni nanowire by lift-off resistance at low temperatures is 0.748 of the room temperature resistance, as compared to the thin film of 0.4591. Ni nanowire by Ar ion-milling of similar width resistance at low temperatures is 0.2981 of the room temperature resistance, as compared to the thin film of 0.2242. Thus, due to patterning, if all other conditions are equal, the increase in low temperature resistivity should be equal for both cases (i.e., the increase in resistivity should be attributed to an increase in surface scattering). The lift-off case should increase by 49% while the ion mill case to increase by 35%. Such differences cannot be attributed to error in measurement. It is proposed that the marked increase can be attributed to the structure of the electron-beam lift-off nanowire. More specifically, the continuous string of islands would require a higher surface area than a continuous smooth structure in the sputtered ion milled nanowire structure.

By far the best transport results stem from processing steps where the sample starts with sputter-deposited thin film. The overall resistivity of the nanowire is close to values reported elsewhere of $10 \mu\Omega\text{-cm}$ [Hon95a]. With a triangular cross-section from a TEM image, the calculated resistivity of the wire structure is $14.6 \mu\Omega\text{-cm}$. The

corresponding field value (~500 Oe) for the minimum MR value in the longitudinal orientation is close to values reported elsewhere [Pir97a]. An interesting result of this investigation is the dependence of 'AMR' values on temperature. Much of the AMR investigations have been conducted at room temperature, since other scattering mechanisms complicate the analysis [McG75]. The temperature where the maximum MR occurs differs from the film and nanowires of different widths. The MR values initially increase as temperature is decreased. This behavior can be attributed to the fact that the overall resistance is falling due to a decrease in phonon scattering mechanisms. At lower temperatures, other scattering mechanisms come into effect, namely defect and surface scattering. These scattering mechanisms do not possess directionality and will result in the decrease of an anisotropic scattering mechanism. Thus, a decrease in MR values results as the temperature is lowered further.

CHAPTER 6 CONCLUSIONS

1. Summary

Fabrication of sub-micrometer-sized magnetic structures such as Co/Cu sandwiches and pseudo spin-valves was successfully demonstrated using direct depositions by UHV magnetron sputtering or evaporation and lift-off processing. Magnetization measurements on these patterned arrays of wire structures with minimum feature sizes as small as 0.5 μm showed saturation values equal to the deposited unpatterned thin films (Fig.4.6). This result indicated that there were minimal effects from patterning by direct deposition and lift-off for the size range. AFM and cross-sectional TEM (Figs.4.1, 4.5) images indicated minimal shadowing effects due to resist structures during sputter deposition for specific conditions, which were founded empirically. Cross-sectional TEM indicated for the Fe(50Å)/Co(50Å)/Cu(50Å)/ Co(50Å)/Cu(20Å) sandwich structure that at the edge, profile has a rise to run ratio approximately 1:8 extending approximately 800 Å from the edge (Fig.4.5). For dimensions as small as 0.5 μm , direct deposition and lift-off was found to be a viable alternative to processing, which requires underlying magnetic thin film to undergo thermal treatments.

NiFe/Ag multilayer structures were first studied to determine if geometrical patterning would induce anti-parallel alignment between successive magnetic layers by dipolar coupling. Magnetization measurements showed clearly that the wire pattern

induced an 'easy' axis in the direction parallel to the axis of the wire. This was observed from the remnant magnetization values normalized to the magnetic saturation values. For the 'hard' axis (the applied field perpendicular to the wire axis), this ratio was around 0.15 while for 'easy' axis, it was around 0.9 (Fig.4.8). Transport measurements indicated that the magnetic layers were not aligned anti-parallel to each other across the Ag spacer layer from positive magneto-resistance, much like the longitudinal AMR response. Such a response may be due to the high length to width ratio and the dipolar fields at the ends may not be strong enough to align the magnetization anti-parallel across the length of the wire.

Another system studied was Fe(50Å)/Co(50Å)/Cu(50Å)/Co(50Å)/Cu(30Å) whose magnetization measurement followed similar trends as a NiFe/Ag multilayer, indicating that shape anisotropy has a strong influence. Transport measurements on this Co/Cu sandwich structure indicated a negative MR characteristic of the GMR with a value around 1.32% (Fig.4.13) independent of width. This result or, more specifically, that GMR value not decreasing with linewidth, was a strong indication that the patterning process did not have detrimental effects. Such effects could have been a physical bridging of successive magnetic layers at the edges. Physical bridging would couple the magnetic layers, reducing anti-parallel magnetization between the layers. Although MR values independent of linewidth were observed (0.6 μm to 10 μm), this finding did not take into account that total resistivity was increased by more than a factor of 15. Such findings are similar to AMR vs. linewidth findings by Jia et al in Ni and Co bars [Jia97]. The small value of the GMR in this case was due to the fact that relatively thick layers were used, especially 50 Å of Cu spacer layer. Relative thick spacer layers would allow currents to be

shunted, thus lowering the MR values (Chapter 3.2.2.2, Fig.3.6). The shape of the MR response was asymmetrical (Fig.4.11) indicating a relatively sudden reversal of the first magnetic layer followed by a protracted reversal of the second layer and eventual technical saturation, whose value was largely dependent on width.

Properties such as the coercive field measured by SQUID magnetometer and the field of maximum MR were strongly size-dependent. Due to the multilayer structure and the GMR being the dominant magneto-transport characteristic, the proposed correspondence to local minima in longitudinal MR responses of Ni and $\text{Ni}_{0.8}\text{Fe}_{0.2}$ to coercive field does not hold true in this case [Hon95a, Ade97]. The field at maximum MR corresponds to an anti-parallel alignment of successive magnetic layers, which does not necessitate the total magnetization being zero. Specifically, for the Co/Cu sandwich considered, the magnetization of the Fe buffer layer was postulated to cause the offset between these two characteristic fields. This argument also holds true for the Co/Cu pseudo spin-valve structure studied.

This study of spin-valve structures with widths down to $0.5\ \mu\text{m}$ showed that the fabrication process used allowed comparison of varying linewidths. This direct deposition and lift-off processing resulted in wire structures. Characterization of these structures showed that dipolar coupling plays an important role in these dimensions. From MR characterization, the switching characteristics of various magnetic layers can be surmised by a correlation to magnetization measurements. Due to the high length to width ratios, the dipolar interaction was not successfully utilized to achieve anti-parallel alignment to achieve the GMR response in NiFe/Ag multilayer structures. Dipolar interaction was significant enough to delay complete saturation in the Co/Cu sandwich and PSV

structures. With the identified fabrication and characterization techniques, many more systems can be studied, which will be described in a later section.

In efforts to extend the studies to dimensions less than 0.5 μm , nanowire structures with widths as small as 50 nm have been fabricated using advanced electron-beam lithography techniques. By utilizing a bi-level resist structure, the ‘lift-off’ technique was found to yield well-defined structures. Although these structures’ volumes were not sufficient to produce high enough signals for direct magnetization measurements, by incorporating leads, characterization was performed by transport measurements. Direct deposition through the nanometer-sized openings yielded highly disordered samples, especially for sputter-deposited samples. Such conclusions stemmed from transport measurements where direct sputter-deposited samples showed high resistances and resistances that were temperature independent.

By incorporating evaporation depositions, the total resistances were lower. For a thermally evaporated Ni nanowire, transport measurements indirectly revealed possible discontinuities in the structure since the resistance ‘opened’ as the temperature decreased. This characteristic was explained by postulation that at room temperatures the transport was carried out by shunting through small gaps via a SiO_2 substrate layer. This assumption is supported by AFM images (Fig.5.5) and from $\ln(R)$ vs. $1/T$ plot (Fig.5.8(a)). The transport characteristic cannot be wholly attributed to conduction through the substrate since magneto-transport measurements reveal AMR characteristics, which the substrate by itself would not indicate. Nanowires by electron-beam evaporation showed metallic resistance vs. temperature behavior, although its resistivity ratios indicated considerably higher impurity ratios than thin film sample. These samples also

displayed well-behaved MR characteristics for various orientations to the applied field (Fig.5.9(b,c,d)).

Another method was to start with high quality thin film structure and pattern Nb nanowire structures that served as a mask for an ion-milling etch process. These structures' resistivity were in the $10 \mu\Omega\text{-cm}$ range, a value close to what is reported elsewhere [Hon95]. The longitudinal MR showed that at moderate fields ($<2000 \text{ Oe}$) the resistances decreased from saturation values (Fig.5.10(b)). This response indicates formation and growth of domain walls. If the domain reversal processes were a coherent rotation, due to shape anisotropy, a sharp reversal would be expected and a flat longitudinal MR response would be seen. Cross-section TEM reveals the cross-section geometry to be triangular. This deviation from rectangular may be due to a sloped cross-section of an Nb mask layer deposition or re-deposition effects during Ar ion-milling. Such shapes must be considered if any micro-magnetic modeling were to be performed.

From various fabrication and characterization of Ni nanowires, it can be concluded that Ni nanowires fabricated by an etching process were most successful. Comparing residual resistances for various structures considered can directly lead to this conclusion. This distinction can be attributed to the fact that the quality of the thin film is far superior than the structures produced by direct deposition through nanometer-sized apertures. It can be speculated that high resistivities of direct deposition and lift-off samples stem from contaminants that may be introduced during deposition by the resist structure and possibly high gas pressures within the developed openings of these structures. Although processing steps involved thermal treatments, for dimensions less than 100 nm, fabrication

methods utilizing high quality thin film, which is further processed, are more advantageous than direct deposition and lift-off processes.

2. Future Work

In this dissertation, a fabrication process has been found to produce magnetic structures with minimal feature sizes from near-micrometer to tens of nanometers. Through the course of the research, many interesting properties have been observed that can be expanded for future considerations. One conclusive result of this study is that for dimensions greater than $0.5\ \mu\text{m}$, relatively quick direct deposition and lift-off processing yield structures that can be utilized to study dimensional effects. By simply adding more numbers of samples where the distance between structures are varied, one can deduce the effects of neighboring elements on magnetic and magneto-transport properties. These effects need to be studied as magnetic recording densities increase. Such effects would be more relevant as elements are closely packed, and new geometries or arrangements may lessen the media requirement to have extremely high coercive values. Also, for MRAM applications, such studies would be warranted as current to switch a particular element may cause a neighboring element to incidentally switch. Other than an obvious increase in the number of permutation and number of samples, there are other relevant future considerations.

Although Ni did not show single domain characteristics even for widths as small as 70 nm, evidence of Co wires (for sub-micrometer dimensions) reversing magnetization by a single domain rotation is found elsewhere [Jia97, Pir97]. Such behavior does not fully agree with MR behaviors of the Co/Cu sandwiches and PSVs studied for dimensions

down to 0.5 μm . This study has shown the MR response to be asymmetrical where total saturation of resistance occurs at much higher fields (Figs.4.11, 4.14). Such behavior may be due to the layered structure where dipolar coupling between the layers require much higher total saturation fields. Such experiments as varying the spacer thickness (to study coupling effects) to simply observe Co wires may explain why single domain response was not seen in the layered system.

The above mentioned studies of Co/Cu sandwiches and PSVs as well as other GMR systems can be expanded to dimensions approaching tens of nanometers by using electron-beam lithographic techniques. This study has found that direct deposition and lift-off process utilized for structures with dimensions as small as 0.5 μm do not yield samples with low resistivities. This has been attributed to various causes that can be tested. Such future tests may include a slight elevation of the substrate temperatures, increasing the time that the sample spends in vacuum before deposition, and careful study of out-gassing characteristics of the resist structure. A proven method to fabricate nanowires is to start with high quality thin film structure and pattern by using Nb as an etch mask for Ar ion-milling. Such a method produced Ni nanowires of low resistivities and, more importantly, low residual resistivities. This method has only been demonstrated for an Ni nanowire and can be expanded to layered structures.

APPENDIX A NOTES ON THE UHV SPUTTER DEPOSITION SYSTEM

In this addendum to the body of work presented thus far, a record of the customized circuitry and software, which are tantamount to our UHV sputter deposition system, is presented. Due to the customized nature and the fact that a record of its legacy is incomplete, a more complete documentation is warranted. In this Appendix, a complete 'blueprint' will not be presented, but the general layout will be detailed with the hopes that in the future a competent person will be able to quickly modify and repair the system.

1. Electronic Circuitry and Interface

1.1 Safety Interlocks

One of the major functions of the customized circuitry is for a safety interlock system. Such conditions as pressure, water flow, and various valve positions play a critical role in what functions are available to the user at a particular point of time. The interlock logic is realized by relay network. AND logic is easily realized this way. For example, to open the high vacuum gate valve, the following conditions must be met: 1) pressure in the main chamber and the high vacuum elbow must be less than 0.5 mTorr; 2) the turbo pump must be at set-point rpm. If any of the conditions are not met, the gate valve would be automatically closed. Other functions that are interlocked are:

- turbo pump (TP) - interlocked to cooling water flow and set-point rpm of the backing pump, the Molecular Drag Pump (MDP).

- gate valve (GV)
- roughing pump valve (RV)-interlocked to the pressure in the chamber and elbow, along with status of the turbo pump.
- sputtering guns' power supplies (GS) - interlocked to the cooling water flow to the guns with the status of the gate valve
- lift (LT) - interlocked to the pressure in the chamber

Some of the interlocks have an over-ride mechanism. The over-ride is only possible by turning the key switch to 'over-ride enable,' thereby enabling that particular switch. Over-ride is the only mechanism by which the chamber can be returned to atmosphere. To achieve a return to atmosphere, the roughing pump valve (which closes automatically for pressures less than 0.5 mTorr), the interlock must be over-ridden to open it and let dry nitrogen to re-enter the chamber.

1.2 Interlock Realization

As mentioned, the interlock circuitry logic is realized by a relay network. Such parameters as pressure, water flow, and status of the pumps are able to be read by passing current through manufacturers' relays associated with the pressure gauge controller, water flow meter, and pump controllers. Each parameter has an external relay that is energized when current passes and energizes them as manufacturers' relays are closed when their respective conditions are met. The use of this redundancy is to protect the commercial circuitry from any user errors. Each interlock condition would have a series of relays connected in a series such that a closed circuit occurs when all conditions are met. The interlock over-ride mechanism works by shorting the series of relays through a turn-key switch and an over-ride specific switch.

1.3 Process Control Circuitry

An interface between the various commercial components has been implemented. This interface allows for automated controls of the DC and RF power supplies, shutters control, step-motor, and controller. Each component requires a unique implementation. For example, the DC power supplies require binary settings for their mode of operation and an analog signal for the amount of power (current or voltage) delivered. The step-motor controller communication and programming is conducted by serial connection, which are controlled by string commands. The shutter controls allow for both computer control and user control.

All of these components are tied by an interface circuitry and work in harmony as described by the following software implementation.

2. LabView Program for Automated Deposition

Even with low base pressures, to ensure good quality multilayer structures, time between subsequent depositions must be minimized. As an example, the deposition of Ta/NiFe/Cu/Co/Ta spin-valve at 1 mTorr requires the use and control of a four magnetron sputtering gun, power sources, substrate positioning, and shuttering control with deposition times on the order of tens of seconds. All variable parameters require precise timing and accuracy, which a human operator may take minutes to complete. The use of a micro-computer allows lag time between subsequent deposition of layers in the order of seconds. Thus, a computer-assisted deposition system is in place. The overall command program is written in LabView, a graphical language which allows creation of VI's (Virtual Instruments) which are, in essence, subroutines that carry out specific tasks. The

commands are executed by a series of solid-state relays, D/A converter, and serial port communication.

The software can be found in the “desktop” in the folder “Multi-Lay” in the computer by the sputter deposition chamber. The main VI, **Deposition Controller VI.**, is nothing but an organizational tool, a map. In front of the **Deposition Controller VI.** is a listing of specific tasks, which are broken down further by other VIs which are currently hidden to the user. These VIs pass pertinent information/variables globally. This organization of tasks means that it is imperative that the user input variables to the front panel of VIs when such a VI is properly called (i.e., the actual VI, which is running at the time of data entry). To ensure the panel on screen is the active VI, the software automatically opens SubVIs panels when it is called and closes the panel when exiting the SubVI. For a successful deposition run, the task has been broken up into the following:

- 1) Registration of the sputtering guns. This task requires the material associated with that position (gun); the power supply associated with the gun; the deposition power and the idle power. Guns' positions are fixed as POSITION I (tilt non-magnetic), POSITION II (straight non-magnetic), POSITION III (straight magnetic), and POSITION IV (tilt magnetic). Each position requires the material (only for user purposes of associating and double-checking, i.e., the program doesn't care if there is an Au target or no target), the power supply, the deposition and idle power. The ability to co-deposit is also included in the software.



is the icon associated with REGISTRATION OF GUN INFO

2) Specifying the deposition sequence. It is essential that the user specify the deposition sequence once the guns are registered. It is not essential for the software to have the correct sequence (it can do without it), but the user may require otherwise. The user's request may or may not be what she/he intends. To ensure successful operation, it is highly advised that the user be fully aware of the necessity for understanding how to specify the deposition sequence.



is the icon associated with DEPOSITION ORDER SPEC

3) Displaying the user's input(s). To ensure that there is no misunderstanding between the user and Igor, a display of current inputs is available on request. The VI will display graphically the gun assignments and the deposition sequence. This VI has a simple error checker to make sure that there are not major flaws in the user's input.



is the icon associated with CURRENT INPUT DISPLAY

4) Initializing the system. For safety considerations, certain aspects of the system must be reset and set according to certain guidelines. In addition, the hardware/software interface must be configured. This VI call will allow the user to configure the SSR (Solid-

State Relays (they are red modules located in the interface box), manipulate the platen position and 'light' guns.



is the icon associated with CONFIGURE INITIAL STATE

Due to many tasks associated with CONFIGURE INITIAL STATE, this VI has another level of VI which requires USER input.



is the icon associated with LIGHT GUN

(hidden at the Deposition Controller VI. level)

5) Controlling and monitoring the deposition run. This VI starts the deposition run when the user is satisfied with all inputs and the state of the system. This VI also contains some error checking displays and a final check list to ensure the safety of the system and the user. In this VI, the user monitor can monitor which stage of deposition that is current. Such actions as shutter opening can be monitored in real time.



is the icon associated with SPUTTER TIME

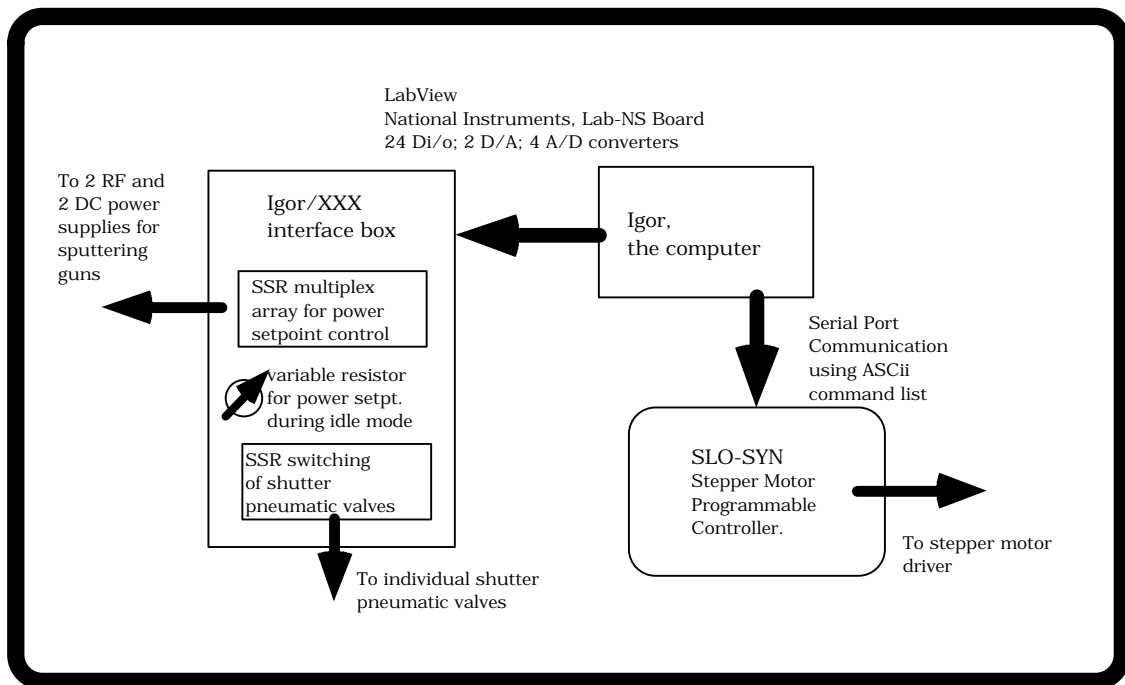


Figure A.1 - Schematic of Igor and computer control interface

A more detailed description can be found in the manual. During deposition, the computer controls the following:

- 1) moves the correctly specified substrate holder over the specified gun.
 - algorithm that takes into account that there are three fixed objects of interest, the temperature controlled substrate position, the room temperature substrate position, and the crystal oscillator head with a limited rotation of $\pm 300^\circ$ from a specified relaxed position
 - Computer communicates with the stepper motor controller through the serial port with information about number of steps, direction, and speed.
- 2) ramps up the power of the corresponding power supply at a specified rate to specified power and mode (for DC power supplies).
 - Due to limited number of D/A converters, D I/O is utilized to multiplex externally the analog signal to a specific power supply
- 3) once the power setpoint is reached, the shutter over the corresponding gun opens for a specified time.
 - Solid-state relays switch a 24 VDC signal to the corresponding solenoid valves to the pneumatic shutters
- 4) after closing of the shutter, the power supply is ramped down to a specified idle power at a specified rate.
- 5) determines next position or whether the deposition run is finished.

APPENDIX B EFFECT OF DRY ETCHING ON MAGNETIC PROPERTIES

In Chapter 5, Ar ion-milling was utilized to transfer pattern. In this addendum to the main work, the effects of Ar ion-milling on magnetic properties will be presented. For this particular study, Kee Bum Jung and Professor Pearton in the Department of Materials Science and Engineering are acknowledged for their help in etching the samples. The samples etched were Ni, Permalloy, and Super-Permalloy; ICP (Inductive-Coupled Plasma) etch reactor was used. For the same etching conditions (15 sccm of Ar, 500 W ICP, and 250 W RF), various 500Å of magnetic films on 50 Å of a Ta buffer layer on Si substrate were etched for various time intervals. After the etch process, the sample dimensions were measured by stylus profilometer and further characterized by SQUID magnetometer and AFM.

From Figure B.1, the etch rate is found by a linear fit of etched depth vs. time of etch. For all Ni and its alloys, etch rate is nearly equal. The non-zero x-intercept for Permalloy and Super-Permalloy indicates that etch process is not instantaneous, possibly due to an oxide layer covering the film. AFM rms roughness is within 5 Å of as-deposited roughness for all considered (Fig.B.2). SQUID magnetization measurements indicate that Ar ion-milling does not create significant damaged 'dead' layers. All physically left thickness seems to contribute magnetically, as Figure B.3 shows saturation magnetization to be independent of remaining thickness.

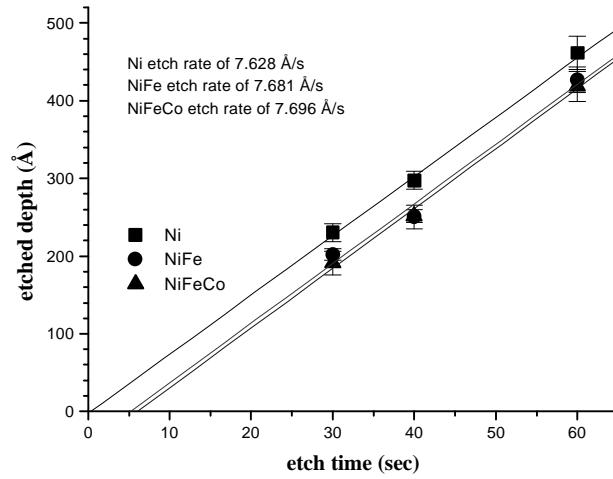


Figure B.1 - Stylus profilometer measured height vs. etch time where linear fit gives etch rates for various Ni and its alloys.

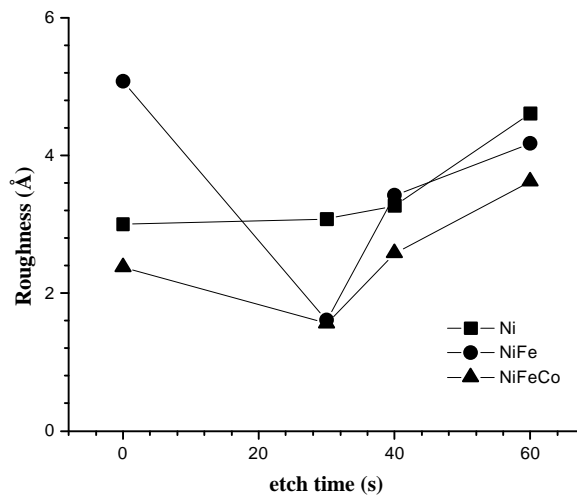


Figure B.2 - AFM rms roughness vs. etch time.

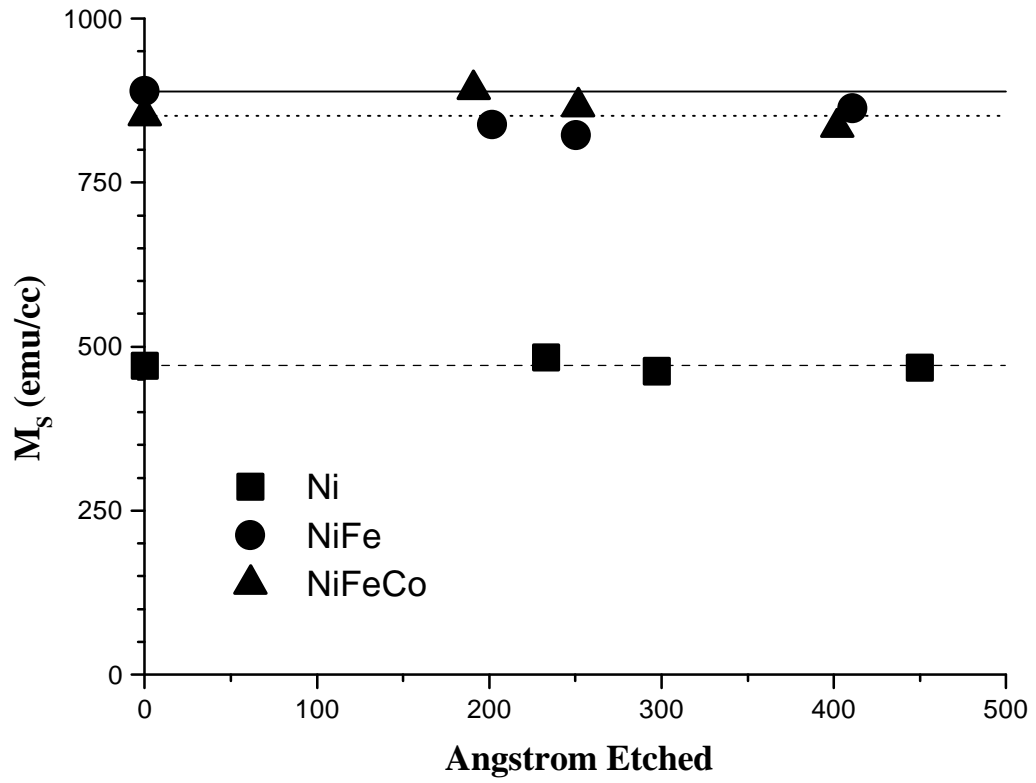


Figure B.3 - Saturation magnetization measurement vs. Å of material etched. Note solid line is the M_s for Super-Permalloy as-deposited, dashed line is Permalloy, and dotted line is Ni.

LIST OF REFERENCES

- Ade96 A.O. Adeyeye, J.A.C. Bland, C. Daboo, J. Lee, U. Ebels, and H. Ahmed, *J. Appl. Phys.* **79**, 6120 (1996).
- Ade97 A.O. Adeyeye, G. Lauhoff, J.A.C. Bland, C. Daboo, D.G. Hasko, and H. Ahmed, *Appl. Phys. Lett.* **70**, 1046 (1997).
- All98 R. Allenspach and W. Weber, *IBM J. Res. Develop.* **42**, 7 (1998).
- Bai88 M.N. Baibich, J.M. Broto, A. Fert, F. Nguyen van Dau, F. Petroff, P. Etienne, G. Creuzet, A. Friederich, and J. Chazelas, *Phys. Rev. Lett.*, **61**, 2472 (1988).
- Baj74 C.H. Bajorek, C. Coker, L.T. Romankiw, and D.A. Thompson, *IBM J. Res. Develop.* 542 (1974).
- Bar90 J. Barnas, A. Fuss, R.E. Camley, P. Grünberg, and W. Zinn, *Phys. Rev. B*, **42**, 8110 (1990).
- Bas98 J. Bass, W.P. Pratt, and P.A. Schroeder, *Comm. on Con. Matt. Phys.* **18**, 223 (1998).
- Bee97 C. Beeli, B. Doubin, J.-Ph. Ansermet, P.A. Stadelmann, and *Ultramicroscopy*. **67**, 143 (1997).
- Bel98 J. Belleson and E. Grochowski. "The era of giant magnetoresistive heads." 1998. <http://www.storage.ibm.com/storage/hardsoft/diskdrdl/technolo/gmr/gmr.htm> (5 Sept. 1998).
- Ben90 W.R. Bennett, W. Schwarzacher, and W.F. Egelhof, *Phys. Rev. Lett.*, **65**, 3169 (1990).
- Blo94 A. Blondel, J.P. Meier, B. Doudin, and J.-Ph. Ansermet, *Appl. Phys. Lett.* **65**, 3019 (1994).
- Boc95 G. Bochi, H.J. Hug, D.I. Paul, B. Stiefel, A. Moser, I. Parashikov, H.-J. Güntherodt, R.C. O'Handley, *Phys. Rev. Lett.* **75**, 1839 (1995).
- Boo95 I. Booth, A.B. MacIsaac, and J.P. Whitehead, *Phys. Rev. Lett.* **75**, 950 (1995).

- Bow94 M.J. Bowden, in *Introduction to Microlithography*, L. Thompson, C.G. Wilson, and M.J. Bowden, eds., pp. 19-138, American Chemical Society, Washington, DC, 1994.
- Bru96 J.A. Brug, L. Tran, M. Bhattacharyya, J.H. Nickel, T.C. Anthony, and A. Jander, *J. Appl. Phys.* **79**, 4491 (1996).
- Bru79 J.H. Brunning, *J. Vac. Sci. Technol.* **56**, 1925 (1979).
- Buc89 J.D. Buckley, D.N. Galburt, and C.J. Karatzs, *J. Vac. Sci. Technol B* **7**, 1607 (1989).
- Cab97a J.A. Caballero, *Growth and Characterization of Thin Films of Heusler Alloy NiMnSb and its Application to Magneto-resistive Multilayer Structures*, Ph.D. Dissertation, University of Florida (1997).
- Cab98 Caballero, J.A., Park, Y.D., Childress, J.R., Bass, J., Chiang, W.-C., Reilly, A.C., Pratt, W.P., Jr., and Petroff, F., *J. Vac. Sci. Technol. A*, **16**, 1801 (1998).
- Cab97b A. Cabbibo, *Magnetic and Magneto-transport Properties of Granular Co-Cu Multilayer Films*, M.S. Thesis, University of Florida (1997).
- Cam82 I.A. Campbell and A. Fert, in *Ferromagnetic Materials*, vol. 3, E.P. Wohlfarth, ed., pp. 747-804, North-Holland Publishing Company, Amsterdam (1982).
- Cam89 R.E. Camley and J. Barnas, *Phys. Rev. Lett.*, **63**, 664 (1989).
- Cho96 S.Y. Chou, P.R. Krauss, and L. Kong, *J. Appl. Phys.* **79**, 6101 (1996).
- Cul72 B.D. Cullity, *Introduction to Magnetic Materials*, Addison-Wesley, New York (1972).
- Dau92 J.M. Daughton, *Thin Solid Films*, **216**, 162 (1992).
- Dau93 J.M. Daughton and Y.J. Chen, *IEEE Trans. Magn.* **29**, 2705 (1993).
- Dau96 J. Daughton and J. Brown, *Proceedings Sensor Expo Anaheim*, p.431, 273-81 (1996).
- deJ94 W.J.M. de Jonge, P.J.H. Bloemen, and F.J.A. den Broeder, in *Ultrathin Magnetic Structures I*, B. Heinrich and J.A.C. Bland, eds., pp.65-86, Springer-Verlag, New York (1994).

- Die91a B. Dieny, V.S. Speriosu, S.S.P. Parkin, B.A. Gurney, D.R. Wilhoit, and D. Mauri, *Phys. Rev. B* **46**, 1297 (1991).
- Die91b B. Dieny, V.S. Speriosu, B.A. Gurney, S.S.P. Parkin, D.R. Wilhoit, K.P. Roche, S. Metin, D.T. Peterson, and S. Nadimi, *J. Magn. Magn. Mater.* **93**, 101 (1991).
- Die94 B. Dieny, *J. Magn. Magn. Mater.* **136**, 335 (1994).
- Doi93 M. Doi, T. Kanbe, and M. Matsui, *J. Magn. Magn. Mater.* **126**, 443 (1993).
- Don91 M. Donath, D. Scholl, H.C. Siegmann, and E. Kay, *Phys. Rev. B.* **43**, 3164 (1991).
- Dub97 S. Dubois, C. Marchal, J.M. Beuken, L. Piraux, J.L. Duvail, A. Fert, J.M. George, and J.L. Maurice, *Appl. Phys. Lett.* **70**, 396 (1997).
- Enz82 U. Enz, in *Ferromagnetic Materials*, vol. 3, E.P. Wohlfarth, ed., pp. 1-36, North-Holland Publishing Company, Amsterdam (1982).
- Eve98 B.A. Everitt and A.V. Pohm, *J. Vac. Sci. Technol. A*, **16**, 1794 (1998).
- Fal98 C. Falco, in "Materials Deposition Techniques," Lecture Notes at Spintronics Summer School, South Lake Tahoe, CA, Aug. 2-8, 1998.
- Far98 R.F.C. Farrow, *IBM J. Res. Develop.* **42**, 43 (1998).
- Fer93 A. Fert and T. Valet, *J. Magn. Magn. Mater.* **121**, 378 (1993).
- Fer94 A. Fert and P. Bruno, in *Ultrathin Magnetic Structures II*, B. Heinrich and J.A.C. Bland, eds., pp.82-117, Springer-Verlag, New York (1994).
- Fer95 A. Fert, P. Grünberg, A. Barthelemy, F. Petroff, and W. Zinn, *J. Magn. Magn. Mater.* **140-144**, 1 (1995).
- Fis89 G. Fishman and D. Calecki, *Phys. Rev. Lett.*, **62**, 1302 (1989).
- Gan96 S. Gangopadhyay, M.T. Kief, J.A. Barnard, and M.R. Parker, *J. Magn. Magn. Mater.* **161**, 43 (1996).
- Gre92 D. Greig, M.J. Hall, C. Hammond, B.J. Hickey, H.P. Ho, M.A. Howson, M.J. Walker, N. Wisen, and D.G. Wright, *J. Magn. Magn. Mater.* **110**, 239 (1992).
- Har93 G.R. Harp, S.S.P. Parkin, R.F.C. Farrow, R.F. Marks, M.F. Toney, Q.H. Lam, T.A. Rabedeau, and R.J. Savoy, *Phys. Rev. B* **47**, 8721 (1993).

- Har94 G.R. Harp and S.S.P. Parkin, *Appl. Phys. Lett.* **65**, 3063 (1994).
- Has97 M. Hassoun, W. Black, E. Lee, R. Geiger, and A. Hurst, *IEEE Trans. Magn.* **33**, 3307 (1997).
- Hei93 B. Heinrich and J.F. Cochran, *Adv. in Phys.*, **42**, 523 (1993).
- Hey96 T. Heyn. "MR Heads: The Next Step in Capacity and Performance." 1996. <http://www.seagate.com/corp/vpr/literature/papers/tbmrhead.shtml> (4 Sept. 1998).
- Hol96 H. Holloway and D.J. Kubinski, *J. Appl. Phys.* **79**, 7090 (1996).
- Hon95a K. Hong and N. Giordano, *Phys. Rev. B* **51**, 9855 (1995).
- Hon95b K. Hong and N. Giordano, *J. Magn. Magn. Mater.* **151**, 396 (1995).
- Hsi97 R. Hsiao, D. Miller, T. Lin, and N. Robertson, *Thin Solid Films*, **304**, 381 (1997).
- Hub98 A. Hubert and R. Schäfer, *Magnetic Domains: Analysis of Magnetic Microstructures*, Springer, New York (1998).
- Hum93 R. Hummel, *Electronic Properties of Materials*, Springer-Verlag, New York (1993).
- Hyl93 T.L. Hylton, K.R. Coffey, M.A. Parker, and J.K. Howard, *Science*. **261**, 1021 (1993).
- Hyl95 T.L. Hylton, M.A. Parker, K.R. Coffey, J.K. Howard, R. Fontana, and C. Tsang, *Appl. Phys. Lett.* **67**, 1154 (1995).
- Jia97 Y.Q. Jia, S.Y. Chou, and J-G, Zhu, *J. Appl. Phys.* **81**, 5461 (1997).
- Joh91 M. Johnson, *Phys. Rev. Lett.* **67**, 3594 (1991).
- Kit86 C. Kittel, *Introduction to Solid State Physics*, John Wiley & Sons, New York (1986).
- Kon69 J. Kondo, *Solid State Physics*, **23**, 184 (1969).
- Kri63 C.J. Kriessman and S. Middelhoek, *J. Appl. Phys.* **34**, 1055 (1963).
- Kry96 M.H. Kryder, W. Messner, and L.R. Carley, *J. Appl. Phys.* **79**, 4485 (1996).

- Kum96 M. Kume, A. Maeda, T. Tanuma, and K. Kuroki, *J. Appl. Phys.* **79**, 6402 (1996).
- Lee97 J. Lee, *Comparison of High-density Electron Cyclotron Resonance and Inductively Coupled Plasma Sources for Etching of Electronic Materials : New Plasma Etch Regimes for Electronic Materials*, Ph.D. dissertation, University of Florida (1997).
- Lee92 S.W. Lee, W.P. Pratt, J.M. Slaughter, P.A. Schroeder, and J. Bass, *Phys. Rev. B* **46**, 548 (1992).
- Lev82 M.D. Levenson, N.S. Viswanathan, and R.A. Simpson, *IEEE Trans. Electron Devices*, **59**, 1828 (1982).
- Lev90 P.M. Levy, S. Zhang, and A. Fert, *Phys. Rev. Lett.*, **65**, 1642 (1990).
- Mat91 J. Mathon, *Contemp. Phys.* **32**, 143 (1991).
- McG75 T.R. McGuire and R.I. Potter, *IEEE Trans. Magn.* **11**, 1018 (1975).
- Mea65 T. Meaden, *Electrical Resistance of Metals*, Plenum, New York (1965).
- Meu79 B.J. Meusemann, *J. Vac. Sci. Technol.* **16**, 1886 (1979).
- Mor79 J.M. Moran and D.J. Maydan, *J. Vac. Sci. Technol.* **16**, 1620 (1979).
- Mos91 D.H. Mosca, F. Petroff, A. Fert, P.A. Schroeder, W.P. Pratt, and R. Laloe, *J. Magn. Mater.* **94**, L1 (1991).
- Mot64 N.F. Mott, *Adv. Phys.* **13**, 325 (1964).
- Muc94 J.A. Mucha, D.W. Heiss, and E.S. Aydil, in *Introduction to Microlithography*, L. Thompson, C.G. Wilson, and M.J. Bowden, eds., pp. 377-507, American Chemical Society, Washington DC, (1994).
- Noz98 Y. Nozaki, T. Ono, K. Motohashi, H. Miyajima, and T. Kinoshita, *J. Magn. Mater.* **171-181**, 1271 (1998).
- Ohr92 M. Ohring, *The Materials Science of Thin Films*, pp. 101-141, Academic Press, Inc., New York (1992).
- Par97 Y. D. Park, J. A. Caballero, A. Cabbibo, J. R. Childress, H. D. Hudspeth, T. J. Schultz and F. Sharifi, *J. Appl. Phys.*, **81**, 4717 (1997).

- Par91a S.S.P. Parkin, Phys. Rev. Lett. **67**, 3598 (1991).
- Par91b S.S.P. Parkin, R. Bhadra, K.P. Roche, Phys. Rev. Lett. **66**, 2152 (1991).
- Par91c S.S.P. Parkin, Z.G. Li, and D.J. Smith, Appl. Phys. Lett. **58**, 2710 (1991).
- Par92 S.S.P. Parkin, R.F. Marks, R.F.C. Farrow, G.R. Harp, Q.H. Lam, and R.J. Savoy, Phys. Rev. B **46**, 9262 (1992).
- Par92a S.S.P. Parkin, Appl. Phys. Lett. **61**, 1358 (1992).
- Par93 S.S.P. Parkin, Phys. Rev. Lett. **71**, 1641 (1993).
- Par94 S.S.P. Parkin, in *Ultrathin Magnetic Structures II*, B. Heinrich and J.A.C. Bland, eds., pp.148-186, Springer-Verlag, New York (1994).
- Pet91 F. Petroff, A. Barthélémy, A. Fert, P. Etienne, and S. Lequien, J. Magn. Magn. Mater. **93**, 95 (1991).
- Pir94 L. Piraux, J.M. George, J.F. Despres, C. Leroy, R. Ferain, R. Legras, K. Ounadjela, and A. Fert, Appl. Phys. Lett. **65**, 2484 (1994).
- Pir97 L. Piraux, S. Dubois, J.L. Duvail, K. Ounadjela, and A. Fert, J. Magn. Magn. Mater. **175**, 127 (1997).
- Pir97a L. Piraux, S. Dubois, E. Ferain, R. Legras, K. Ounadjela, J.M. George, J.L. Maurice, and A. Fert, J. Magn. Magn. Mater. **165**, 352 (1997).
- Pra91 W.P. Pratt, S.F. Lee, J.M. Slaughter, P.A. Schroeder, and J. Bass, Phys. Rev. Lett. **66**, 3060 (1991).
- Rij97 Th.G.S. Rijks, R.F.O. Reneerkens, R. Coehoorn, J.C.S. Kools, M.F. Gillies, J.N. Chapman, and W.J.M. de Jonge, J. Appl. Phys. **82**, 3442 (1997).
- Ros93 S.M. Rossnagel, in *Multicomponent and Multilayered Thin Films for Advanced Microtechnologies: Techniques, Fundamentals and Devices*, O. Auciello and J. Engemann, eds., pp. 1-20, Kluwer Academic Publishers, Boston, 1993.
- Rud54 M.A. Ruderman and C. Kittel, Phys. Rev., **96**, 99 (1954).
- Rus95 S.E. Russek, R.W. Cross, S.C. Sanders, and J. Oti, IEEE Trans. Magn. **30**, 3939 (1995).

- Sch98 T.J. Schultz, *Electron Beam Lithography Methods for Fabrication of Magnetic Nanostructures*, M.S. Thesis, University of Florida (1998).
- Sch97 W. Schwarzacher, K. Attenborough, A. Michel, G. Nabiyouni, and J.P. Meier, *J. Magn. Magn. Mater.* **165**, 23 (1997).
- Sha89 F. Sharifi, *Thermal Activation and Macroscopic Quantum Phenomena in Super-conducting Devices*, Ph.D. Dissertation, University of Illinois at Urbana-Champaign (1989).
- She94 C. Shearwood, S.J. Blundell, M.J. Baird, J.A.C. Bland, M. Gester, H. Ahmed, and H.P. Hughes, *J. Appl. Phys.* **75**, 5249 (1994).
- She97 J. Shen, *IEEE Trans. Magn.* **33**, 4492 (1997).
- Shi90 T. Shinjo and H. Yamamoto, *J. Phys. Soc. Jpn.* **59**, 3061 (1990).
- Shu88 R.J. Schutz, in *VLSI Technology*, S.M. Sze, ed., pp.184-232, McGraw-Hill, New York (1988).
- Smi58 F.M. Smith, *Bell Sys. Tech. Jour.*, 711 (1958).
- Smi88 N. Smith, *J. Appl. Phys.* **63**, 2932 (1988).
- Stu83 R.V. Sutart, *Vacuum Technology, Thin Films, and Sputtering : an Introduction*, Academic-Press, New York (1983).
- Tho94 L. Thompson, in *Introduction to Microlithography*, L. Thompson, C.G. Wilson, and M.J. Bowden, eds., pp. 377-507, American Chemical Society, Washington DC, (1994).
- Tom92 M.E. Tomlinson, R.J. Pollard, D.G. Lord, and P.J. Grundy, *J. Magn. Magn. Mater.* **111**, 79 (1992).
- Tsa82 C. Tsang and R. Fontana, *IEEE Trans. Magn.* **18**, 1149 (1982).
- Val54 L.B. Valdes, *Proc. I.R.E.*, **42**, 420 (1954).
- Val93 T. Valet and A. Fert, *Phys. Rev. B* **48**, 7099 (1993).
- Van81 T. Van Duzer and C.W. Turner, *Principles of Super-conducting Devices and Circuits*, Elsevier, New York (1981).

- Voe95 B. Voegeli, AL. Blondel, B. Doudin, and J.Ph. Ansermet, *J. Magn. Magn. Mater.* **151**, 388 (1995).
- Wes80 W.D. Westwood, *MRS Bulletin*, 46 (1980).
- Whi95 R. White, *How Computer Works*, Ziff-Davis Press, Emeryville, CA (1995).
- Woh80 E.P. Wohlfarth, in *Ferromagnetic Materials*, vol. 1, E.P. Wohlfarth, ed., pp. 1-70, North-Holland Publishing Company, Amsterdam (1980).
- Yos96 K. Yoshida, *Theory of Magnetism*, Springer, New York (1996).
- Zha92 S. Zhang and P.M. Levy, *Mat. Res. Soc. Symp. Proc.*, **231**, 255 (1992).
- Zij82 H. Zijlstra, in *Ferromagnetic Materials*, vol. 3, E.P. Wohlfarth, ed., pp.37-105, North-Holland Publishing Company, Amsterdam (1982).

BIOGRAPHICAL SKETCH

Yun Daniel Park was born on October 31, 1972, in Seoul, Korea. Late in 1980, Dan followed his father and mother along with his younger brother, Jin, to the United States where his father enrolled at Purdue University as a graduate student in computer science. Due to the nature of his father's work, Dan moved to many places, from West Lafayette, Indiana to Indianapolis, Indiana, to Charlotte, North Carolina where the family settled for five years. At North Carolina, Dan was accepted for admission to the North Carolina School of Science and Mathematics (NCSSM) where he finished his junior and senior years of high school. At NCSSM, Dan was introduced to inspiring teachers in all subjects, so much so that he enrolled in an unheard-of class load of nine courses in one semester. More than anything else, NCSSM taught Dan earlier than others how to live and enjoy time away from home and prepared him for college.

After graduation from NCSSM in '90, Dan enrolled in the College of Engineering at Cornell University in Ithaca, New York. As a freshman, he enrolled in a wide variety of courses including honor course work in physics with an eye to major in materials science and engineering. He soon realized that the materials science major offered too many topics other than his interest in electronic materials. Thus, he majored in electrical engineering with an emphasis on solid-state devices while conducting undergraduate research work in both the Department of Materials Science and Engineering (MSE) and the School of Electrical Engineering. As a freshman and sophomore, Dan worked with

the human performance lab in the Department of Theoretical and Applied Mechanics, where he was in charge of a small machine shop. In his junior year, he worked for Prof. Ast in the Department of MSE working on an optical injection modification for DLTS. Between his junior and senior years, he was a Materials Science Center intern working under Prof Blakely. For his senior year project, he worked with Prof. Dick Shealy in the School of Electrical Engineering.

After graduation from Cornell ('94), Dan enrolled at the University of Florida in the Department of MSE to pursue the Ph.D. degree, originally working for Prof. Childress. Due to Prof. Childress's departure to IBM, he was fortunate to be under the supervision of Prof. Holloway. Along the way, he has found a wonderful person in Clara J. Shin whom he married on June 21, 1997. After graduation, Dan would like nothing more than prove to become a respected and productive scientist to justify the faith of all who have supported him.